Doctoral Thesis

Form Finding of Deployable Elastic Gridshells Based on Nets of Geodesic Curves

submitted in satisfaction of the requirements for the degree of
Doctor of Science in Civil Engineering
of the TU Wien, Faculty of Civil Engineering

Dissertation

Formfindung von Aufspannbaren Elastischen Gitterschalen mit Netzen von Geodätischen Linien

ausgeführt zum Zwecke der Erlangung des akademischen Grades eines
Doktors der technischen Wissenschaften
eingereicht an der Technischen Universität Wien, Fakultät für Bauingenieurwesen

von

Dipl.-Ing. **Stefan Pillwein**, BSc
Matr.Nr.: 00925449

Advisor: Assoc. Prof. Dr. techn. **Przemyslaw Musialski**
Department of Computer Science
New Jersey Institute of Technology (NJIT)
University Heights, Newark, NJ 07102, United States

Advisor: Univ.-Prof. Dipl.-Ing. Dr. techn. **Josef Füssl**
Institute for Mechanics of Materials and Structures
Technische Universität Wien (TU Wien)
Karlsplatz 13/202, 1040 Vienna, Austria

Reviewer: Prof. Dr. **Mark Pauly**
Geometric Computing Laboratory
École polytechnique fédérale de Lausanne (EPFL)
Rte Cantonale, 1015 Lausanne, Switzerland

Reviewer: Prof. Dr. **Olga Sorkine Hornung**
Interactive Geometry Lab
Eidgenössische Technische Hochschule Zürich (ETH Zürich)
Universitätstrasse 6, 8092 Zürich, Switzerland

Wien, im November 2022

I thank

my supervisor Przemyslaw Musialski for putting his trust in a freshly baked civil engineering graduate student and thus giving me the great chance to do this Ph.D.,

my supervisor Josef Füssl for mentioning *this other topic* in our meeting on open diploma theses when I was already almost out of his office (I stuck to it),

Christian Müller, Helmut Pottmann, and Florian Rist for their support and inspiring discussions,

my father Gerhard for always having an open ear for my problems, being a great tower of strength, and always taking his time to spin ideas with me,

my mother Gabriele for her positiveness, unconditional trust in my abilities, and encouraging and motivating words in tough times,

my loving family and dear friends for their support (I am sorry for having made myself scarce sometimes).

And to all my nearest and dearest who were here when I started this journey but aren't here anymore: You have a special place in my heart.

Abstract

This thesis proposes a novel type of planar–to–spatial deployable structures called elastic geodesic grids. It aims at approximating freeform surfaces with spatial grids of bent lamellas, which can be deployed from a planar configuration using a simple kinematic mechanism. Encoded in the layout of the planar grids is the intrinsic shape of the target surface. When deployed, the grids buckle by design, approximating the curved target shape closely as grid elements bend and twist. Such elastic structures are easy–to–fabricate and easy–to–deploy and produce shapes that combine physics and aesthetics. They may serve architectural purposes like free-form envelopes, sun and rain protectors, pavilions, or equally smaller-scale applications like decorative panels, deployable furniture, baskets, lamps, etc.

The thesis proposes solutions based on nets of geodesic curves on target surfaces and introduces a set of conditions and assumptions which can be closely met in practice. Target surfaces with different characteristics allow different solutions: Restricting the target surfaces to patches enclosed by convex geodesic quadrilaterals simplifies the design problem and enables solutions with high practical usability. Clearly, this approach potentially leads to big cut-offs, unacceptable for many design purposes. Conveniently, decomposing surfaces into smaller patches is an effective strategy for tackling the problem with cut-offs and curvature-related issues. But even arbitrary boundaries of patches can be considered. Dealing with non-convex boundaries requires additional procedures, as shortest connections are not necessarily geodesic curves. It is possible to deal with surface patches of this sort, generalizing the notion of elastic geodesic grids. All these approaches are deeply connected to the inner geometry of the target surface. They involve solving optimization problems in abstract spaces, where solutions are found more easily.

The form-finding of such grids is challenging. Fortunately, their shape is deeply linked to geometry. Exploiting insights from differential geometry allows to speed up form-finding by avoiding the necessity of numerical shape optimization and physical simulation at an acceptable loss of accuracy.

The proposed algorithms finally ensure that the 2d grids are perfectly planar, making the resulting gridshells inexpensive, easy–to–fabricate, transport, assemble, and deploy. Additionally, since the structures are pre-strained, they also come with load-bearing capabilities.

This thesis proposes a solution for the design, computation, and physical simulation of elastic geodesic grids. It presents several fabricated small-scale examples and a prototype of some meters in size, all with varying geometric complexity. Moreover, it provides empirical proof of the employed methods and assumptions by comparing the results to laser scans of the fabricated models. The outcome of this research is intended as a form-finding tool for elastic gridshells in architecture and other creative disciplines. It should give the designer an easy-to-handle way to explore such structures, as results can be obtained in a matter of seconds.

Table of Contents

Chapter 1

Introduction

Wherever nature reveals efficient strategies, humans readily copy them. The purposeful use of elasticity is a well-known example and stands at the heart of this thesis. Using elastic strips of material to create stronger, curved shapes by weaving, or creating springs by loading objects with elastic energy, are simple examples that evoke the strong connection of shape, geometry, and elasticity. This thesis considers bending assemblies of elastic strips to approximate free-form target surfaces and builds upon the mentioned long-standing idea.

However, using elasticity as a shape-providing tool is tricky for many reasons. Obviously, elasticity has its limits: once the material's ultimate strength is reached, it fails or plastically deforms. Although a fierce adversary for gridshell-building enthusiasts, failure is not the only difficulty: The elastic answer, i.e., the shape of the manipulated elements, is not known a priori. It depends on material parameters and boundary conditions. Nowadays, designing with elasticity has become much easier, as designers and engineers have suitable, fast simulation techniques to compute the elastic equilibrium shapes.

The research topography of computational design involving elasticity as a shape-providing mechanism is vibrant and fast-evolving, including techniques like curved folding, 4d printing, computational knitting, using programmable elastic meta-materials, utilizing elastic linkages, and many more.

But what is an elastic gridshell after all? It is a grid of flexible, rod-like, connected members, which obtains its spatial, curved shape by loading it with elastic energy. More specifically, its shape emerges due to the bending and twisting of members and shearing of the grid, which is governed by an interplay of boundary conditions and member stiffnesses. Their design is determined by different geometric models and assumptions on how members deform.

The research presented in this thesis contributes to the form-finding of scissor-like deployable elastic mechanisms based on geodesic curves. This topic links up many disciplines: In terms of applications, the connections to design and architecture are evident. Asking for specific structural properties clearly requires knowledge of engineering and numerical simulation. However, studying and employing the rich theory of curves and surfaces of differential geometry ultimately leads to superior solutions in terms of performance, appearance, aesthetics, and shape diversity. Furthermore, computational design and form-finding are impossible without a proper understanding of mathematics and computer science, as optimization and efficient algorithms are crucial prerequisites for this design task. From the viewpoint of architecture, the elegant and natural emergence of curvature obtained by bending flat materials opens up far-reaching possibilities to implement functional and resource-effective free-form designs. Furthermore, the lightweight elastic gridshells promise open spaces without much-hated columns. From an engineering point of view, a structure is a vehicle to transport loads to the ground, and an efficient structure does so by using as little material as possible. Among the most exciting structures are shells, and their discrete counterpart, gridshells. Similar to arcs, their curvature makes them efficient, and computing their structural capabilities is a fair challenge. Finally, from a geometric point of view, exploring the rich theory of geodesic curves on surfaces and their connection to the Gaussian curvature is an attractive, highly relevant research task. The same goes for deployable kinematic mechanisms, as elasticity is strongly connected to geometry, considering the Elastica or minimal surfaces.

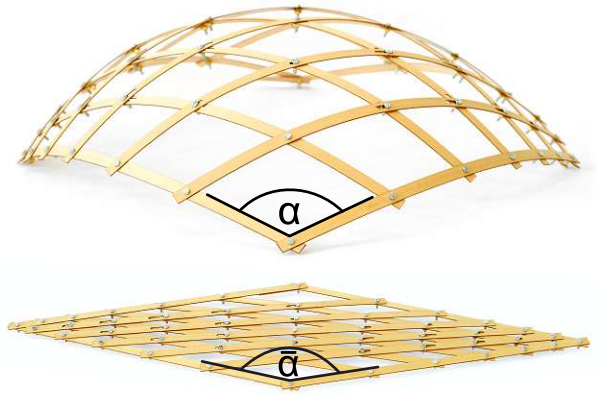

Fig. 1.1: The scissor-like deployment principle of elastic geodesic gridshells. A deployed elastic geodesic gridshell (top) and its planar state (bottom), fabricated from wooden lamellas. The deployment of the whole kinematic system is based on changing the angle $\bar{\alpha}$, such that $\bar{\alpha} \rightarrow \alpha$. Adapted from [Pillwein et al. 2020b].

Creating curvature through elastic energy is commonly denoted as active-bending in the architectural community. It promotes loading objects with potential energy for reversible and cheap creation of curvature and increased

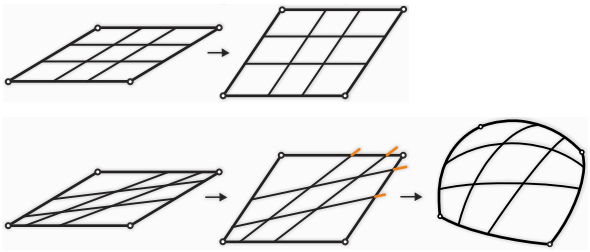

Fig. 1.2: The scissor-like deployment principle. Top: All members of a family are parallel and rigid; the kinematic linkage can move freely in the plane. Bottom: A non-parallel layout produces a deadlock when trying to change the shape since the inner members are too long. Allowing members to deform elastically, they buckle out of the plane. Adapted from [Pillwein et al. 2020b].

structural performance. Considering bendable but non-stretchable flat sheets of material, the space of viable surfaces is limited to singly-curved, developable surfaces, of which there only are three basic types: cylinders, cones, and tangent surfaces of curves. However, by cutting the material into strips and cleverly connecting them to a spatial grid, the space of feasible shapes vastly extends, and approximating non-developable surfaces is feasible.

The method to create curved shapes pursued in this thesis implements this process: Grid-like layouts of flexible strips are arranged carefully in the plane to make them deployable to 3d shapes by changing interior angles. In other words, the target shape is encoded in the planar layout, and a scissor-like mechanism governs the deployment motion. Please note that such a scissor-like deployment is not a novel concept. Related approaches exist, but either build on shaky theoretical foundations, or solve entirely different design problems, which will be discussed thoroughly in Sections 1.1.4 and 1.6.

Intending efficient and aesthetically appealing elastic gridshells, two relevant questions arise: What are efficient shapes for elastic gridshells? Which target surfaces can be approximated well, considering the elastic shape response? While the space of feasible shapes for related structures like planar elastic strips [Hafner et al. 2021] and shells [Block et al. 2007] was already specified, it is unknown for elastic gridshells due to their complexity. Furthermore, reaching high structural efficiency and approximating free-form target surfaces are potentially conflicting objectives. Purely efficiency-driven approaches mainly suggest gridshell shapes such as domes with a convex boundary and positive Gaussian curvature everywhere, which is clearly not attractive from a design perspective. Abandoning the question of efficiency and tending to the space of feasible target surfaces, we again arrive at unexplored research territory. However, current approaches are capable of answering if a given target surface can be approximated well by an elastic grid. Moreover, recent research [Panetta et al. 2019; Pillwein et al. 2020b; Pillwein et al. 2021b] shows that the space of feasible surfaces is rich, even for the subset of scissor-like elastic gridshells.

Asking for a grid layout that approximates a given target surface in its deployed state belongs to the class of inverse design problems. Such problems require finding the cause for a specific effect, i.e., finding the undeployed layout for a target shape. Since there is no standard strategy to solve inverse design problems, they are challenging and require problem-specific insights. Sections 1.2 and 1.6 describe form-finding approaches of elastic gridshells and the ideas and assumptions which allow to solve the inverse design problem for scissor-like deployable elastic geodesic gridshells.

Before going into further detail, a differentiation of terms is needed. Elastic gridshells, or short, elastic grids will serve as an umbrella term for all kinds of flexible grid structures, e.g., grids geometrically based on Chebychev nets, geodesics, asymptotic curves, etc.Elastic geodesic grids [Pillwein et al. 2020b] make use of geodesics and bendable lamellas, with the notable features of being deployable by a scissor-like mechanism and being exactly planar in the undeployed state. Although there are strong ties to architecture and engineering, this thesis addresses a broader audience, including various design disciplines and objects of all scales.

Thesis Overview The present thesis is organized in five chapters: an introduction, three chapters presenting the publications that shape this thesis, and a chapter of concluding remarks.

Chapter 1 serves as an introduction to elastic gridshell structures. To obtain an intuition of the thesis's scope, Section 1.1 introduces the idea of deployable elastic geodesic grids and their implementation. Elastic gridshells are attractive from an engineering and architectural point of view: Section 1.2 covers their historical development, their mechanics, and their structural behavior. Efficient gridshell structures have strong ties to geometry: Section 1.3 discusses their connection to the geometry of curves and surfaces. It examines different frames for surface curves and rods, introduces geodesics and tangential strips, and describes transformable grids with elastic members on target surfaces. Section 1.4 briefly discusses some considerations for the simulation of elastic rod structures.

Section 1.5 outlines the publications of this thesis and states the contributions to the scientific community. Section 1.6 summarizes the related work.

Chapters 2, 3, and 4 present the papers which were published within the scope of this thesis:

- On Elastic Geodesic Grids and Their Planar-to-Spatial Deployment
- Design and Fabrication of Multi-Patch Elastic Geodesic Grid Structures
- Generalized Deployable Elastic Geodesic Grids

Finally, Chapter 5 concludes this thesis, providing discussion and future work.

1.1 Elastic Geodesic Grids

The mission statement of such structures is to approximate a wide range of free-form surfaces by finding specific deployable grid layouts as depicted in Figure 1.1. After the designer provides a target surface, a computational pipeline finds special layouts of geodesic grids and their planarized counterparts. When implementing the planar grids with flexible lamella-like elements, they can be elastically deployed to approximate the initial target surface. This section provides an overview and reveals their properties and the theory and assumptions for their form-finding.

1.1.1 Physical Implementation

Elastic geodesic grids are assembled from two families of straight, thin, non-parallel lamellas, which are easy to bend and twist, but very hard to stretch or contract. Intersections within a family of lamellas are prohibited to ensure deployability, i.e., the combinatorics of the planar grids allow quadrilaterals only. Lamellas are connected by screws, which can slide in elongated holes of different lengths in the interior of the grid, called *notches*. The deployment motion causes the lamellas to buckle by bending and twisting, which creates a 3d curved shape. Finally, dedicated boundary joints are fixed to a supporting structure which secures the desired, final shape of the grid.

1.1.2 Deployment Mechanism

Systematically utilizing buckling and scissor-like deployment mechanisms [Pillwein et al. 2020b; Panetta et al. 2019; Soriano et al. 2019] to approximate target surfaces is a fast and simple method to create curved shapes.

Elastic geodesic grids have a single degree of freedom, i.e., α in Figure 1.1, which controls the changes in angles between members and forces them to deform elastically. Figure 1.2 depicts the scissor-like deployment principle for such grids: Due to non-parallel members, trying to transform the boundary results in length incompatibilities, which are compensated by buckling. In this depiction, all inner members are too long to stay planar, which results in a positively curved shape. However, such layouts are capable of producing negatively curved shapes too, if inner members are too short. Thus, the deployment mechanism is determined by the respective lengths of members and strongly linked to target surfaces and target curves with specific arc-lengths.

1.1.3 Connection to Geodesics

The geometric basis of the proposed structures are geodesics. Such curves do not turn sideways on a surface. As a consequence, developable tangential strips with geodesic centerlines become straight when unfolded in the plane. Please refer to Sections 1.3.3 and 1.3.4 for a more rigorous discussion about geodesics and developable tangential strips on surfaces.

These remarkable properties connect their arc-length and their straightness on the surface and in the plane. Exploiting this connection is most useful for computational design algorithms and the critical component in the approaches presented in this thesis: Just knowing the geodesic distance (i.e., the shortest distance) between two points on a surface allows to infer the existence of a connecting shortest geodesic, where the shape and length of its planar twin is clear. In other words, during form-finding, one may avoid to bother tracing geodesic paths or use approximations. This is beneficial, since distance computation is faster and simpler than tracing shortest geodesics (cf. Section 1.6).

However, which features connect the physical grids (as in Figure 1.2) to geodesic grids on target surfaces and thus provide good shape agreement? One can identify several traits of the physical implementation, which connect it to the underlying geodesic grid. The fundamental assumptions for shape agreement are the following:

- The centerlines of the grid members should agree well with the geodesics. Exploiting the developable tangential strip property of a geodesic suggests strip-like grid members which bend effortlessly, but always remain straight in the planarized state. A close physically feasible counterpart is a lamella, which bends effortlessly out of the plane, but is very stiff to in-plane bending. Thus the agreement of geodesic and centerline is rephrased to agreement of tangential strip and lamella, which show closely related traits (cf. Section 1.3.4).
- The geometric strips are tangential strips, i.e., the principle normals of their geodesic centerlines are aligned with the surface normals. To reverse-engineer this property, lamellas are constrained to lie flat on top of each other, connected by screws in the direction of the respective surface normals.
- Arbitrary geodesic grids cannot be flattened without lengthening or shortening of grid members, which will be discussed more thoroughly in Section 1.1.4. Introducing stretchable materials would corrupt the deployment mechanism and all efforts to obtain a curved target shape due to their low stiffness. Thus, sliding connections at the intersections of grid members take care of this problem and ensure high geometric shape agreement.
- The deployed grid is flexible to undergo elastic deformations, which keep angles between grid members unchanged, much like isometric deformations of surfaces. To constrain the grid to the desired target shape, it is mounted to supports with individually inclined contact areas.

Fig. 1.3: Comparison of an elastic geodesic grid without notches (left) and with notches (right), where the target surface is a patch of a sphere. While the grid with notches shows even curvature, the grid without notches exhibits inappropriate accumulations of curvature.

1.1.4 Length-preserving Mappings of Geodesic Grids

A problem in classic differential geometry refers to geodesic nets on a surface which can be mapped onto geodesic nets on a family of related surfaces, including the inital one. The mapping further shall only allow changing the angles between the geodesics, but keep their arc-lengths fixed. Such geodesic nets and their carrying surfaces were already studied and classified [Voss 1907; Lagally 1910]: A continuous geodesic net can be mapped as described above, if and only if it is rhombic. A rhombic geodesic net requires a parametrization of the surface with geodesics as parameter curves and $E = G$ in the first fundamental form $ds^2 = Edu^2 + 2Fdudv + Gdv^2$. The carrying surfaces of such rhombic geodesic nets were identified as Liouville surfaces. Among others, all rotational surfaces and surfaces of constant Gaussian curvature belong to this type.

Requiring geodesic grids which can be mapped to the plane necessitates a corresponding rhombic net in the plane. Rhombic geodesic nets in the plane consist either of the tangents of a conic section or of two families of lines, where the lines of each family are either parallel or have a common point of intersection [Perron 1924]. Hence, only a subset of Liouville surfaces is feasible.

Based on the different types of planar rhombic nets, Liouville surfaces, that permit the above-mentioned mapping are are the one-sheeted hyperboloid, if the conic section is an ellipse or a hyperbola, or the hyperbolic paraboloid, if the conic section is a parabola. The trivial case of rhombic nets based on parallel lines permits mappings to surfaces isometric to the plane. Please note that the conic sections can degenerate into points or lines. However, they can still be assigned to one of the above cases.

Apart from these examples the space of other feasible surfaces is unclear, and one must accept that geodesic nets on general free-form surfaces which can be planarized in an arc-length preserving manner do not exist. Ignoring this fact compromises the quality of the approximation of elastic geodesic grids, as clearly visible in Figure 1.3. To allow for changes of partial lengths, the concept of notches was introduced [Pillwein et al. 2020b]. Their lengths are determined geometrically by the amount of sliding a connection has to undergo between the planar and the deployed state.

1.2 Elastic Gridshells

This section highlights the relevance of elastic gridshells in the engineering community, where most of it applies to other communities. It further discusses the structural behavior, the idea of scissor-like deployment mechanisms, and form-finding.

Classical civil engineering and architectural structures are assembled from stiff elements, which show deformations so small that one can view them as rigid in a good first approximation. The notion of computing the actual *equilibrium shape* is usually unnecessary: if some design rules are followed, it will agree very well with preceding drawings and plans. In other words, the structure you draw in your CAD software is the structure you get. Yet, elastic structures obtain their shape through elastic deformation and abandon these known grounds in engineering. Their equilibrium shape is a response to external constraints like the supports or loads. In addition to that, closeness to a specific target shape is desired.

Form-finding creates structural shapes that are in static equilibrium. It is required whenever the interaction of geometry, forces, and the desired equilibrium shape is too complicated to be solved by the designer's intuition alone. Form-finding simplifies the design problem as much as possible and provides a quick, approximate initial solution, which fulfills specific constraints and is often obtained using optimization procedures [Woodbury et al. 2006; Adriaenssens et al. 2014b]. This technique is used not only for elastic gridshells but also for masonry shell structures, net structures, membranes, and other elastic structures.

There are two strategies for designing elastic gridshell structures: forward design and inverse design, where *cause* and *effect* have different roles. To determine their meaning, one can resort to Figure 1.2: the cause is the layout of the undeployed grid, the number, kind, and placement of constraints, etc., and the effect is the observable gridshell shape. In forward design, the cause is changed until the effect matches some target shape or a designer's

needs. It is only required to compute the effect induced by the cause, e.g., by simulation. Forward design of gridshells may involve iterative changes in layout and constraints, and subsequent simulation steps until the result is satisfactory. The inverse design does the opposite: it finds the cause for a predefined effect, which is very desirable in the case of a given target surface, but by far much harder to solve.

1.2.1 Practical Relevance

Elastic gridshells offer many advantages for free-form design. They provide a rich space of doubly-curved shapes from small-scale objects like tents, strainers, or weaves to large-span, lightweight structures due to their beneficial structural behavior, which will be discussed in Section 1.2.3. They are resource-efficient since they are assembled from a number of (often straight) elements, which can be cut from plates or prefabricated by other means. They can be assembled on-site without expert knowledge and rapidly deployed manually or by means like mobile cranes for larger structures [Chilton et al. 2016]. Of great practical relevance is their cost: the amount of material needed is low, deployment happens fast, and therefore their cost per square meter of covered area undercuts conventional techniques like casting, milling, or welding by far [Du Peloux et al. 2016].

Elastic geodesic grids benefit from the advantage that they can be assembled from thin strips or lamellas, which are perfectly straight and stay tangential to the surface, which provides an aesthetic appearance and easy fabrication. Furthermore, the lamellas allow out-of-plane bending only (cf. Figure 1.4). This feature makes such structures easier to deploy, which is interesting for all structural scales: The resistance to bending of a rectangular cross-section increases with the third power w.r.t. its height, while the influence w.r.t. its width is linear. In other words, the force needed to deploy them is always relatively small compared to general elastic gridshells with circular or square cross-sections. Furthermore, lamellas' width can be chosen independently of the curvature of the lamellas.

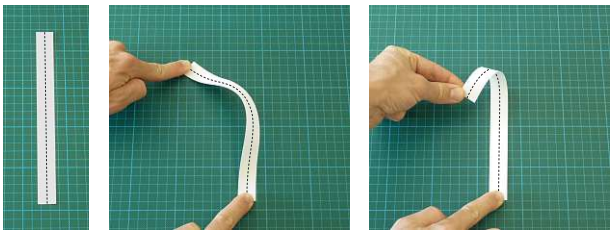

Fig. 1.4: A paper strip and its response to bending. In-plane bending (middle) is impossible without tearing and causes the strip to buckle. Out-of-plane bending (right) is effortless and easily controllable. Lamellas behave similarly, allowing low-effort out-of-plane bending.

Finding practical and cheap strategies to deploy elastic gridshells is essential for easy use and cost-efficiency. Structures assembled in 3d in a weaving-like manner do not enjoy the advantage of planar assembly, require challenging manual labor, and are costly. Clever deployment mechanisms increase the usability of such structures: Scissor-like deployable elastic geodesic grids offer easy and fast deployment of curved structures, especially of small to medium scales, because manual deployment is easy to perform. One can imagine decomposing large free-form surfaces into smaller patches, and deploying and assembling them sequentially, as proposed by one publication [Pillwein et al. 2020a] of this thesis. Undeployed structures are also relatively compact, making them easy to store or transport.

Due to their lightweight design, all elastic gridshells are limited in their external load capacity, and experience undesired buckling easily, which is characteristic of slender structures under compression. The background of the engineering community with elastic gridshells is still somewhat limited due to the small number of realized projects. Furthermore, there are many open questions regarding long-term behavior: Material parameters of common materials like timber or fiber-reinforced plastics vary considerably due to humidity, temperature, and operation time, resulting in variations of shape and stiffness. Furthermore, although form-finding has become increasingly simple, detailed structural evaluation (as required for civil structures) and optimal sizing of cross-sections are anything but straightforward.

1.2.2 Historic Retrospect

This section provides a historical overview of notable elastic gridshell projects, and then turns to recent trends in research. For a taxonomy of elastic gridshells and their historical evolution, please refer to [Chilton et al. 2016; Dickson et al. 2014; Peloux 2017].

Historically, large-scale elastic gridshells spanning several tens of meters were pioneered by the Russian engineer and architect Vladimir Shukhov at the end of the 19th century. He developed delicate hyperbolic gridshells, as well as tensile structures like the Rotunda [Shukhov 1896] at the Panrussian Exposition (cf. Figure 1.5). This flexible structure already reveals some common traits with elastic gridshells. Famous architects like Antoni Gaudí, Frei Otto, and Heinz Isler further pursued the idea of using gravity and elasticity as a shape-providing mechanism. Consequently, among other spectacular structures, Frei Otto designed elastic gridshells, most notably the roof of the Multihalle at the Mannheim Bundesgartenschau [Happold et al. 1975]. Due to the limited capabilities of computational models, by that time, stable elastic structures were designed using empiric methods [Gengnagel et al. 2013]. Among them were hanging chain models to find efficient shapes for arches, shells, and gridshells. Hook's law of inversion [Adriaenssens et al. 2014b] states

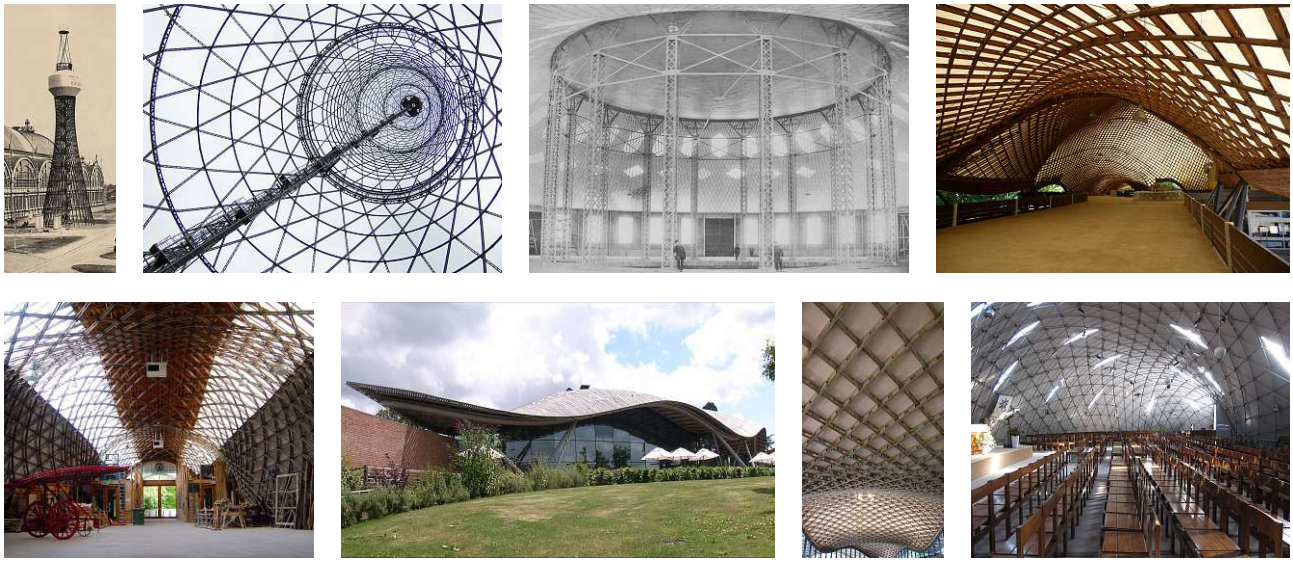

Fig. 1.5: Historical and recent examples of gridshell structures. From left (top) to right (bottom): a) A hyperbolic steel gridshell displayed at the Panrussian Exposition 1896 b) A similar gridshell of 160 meters in height, serving as a broadcasting tower in Moscow, built between 1919–1922 c) The Rotunda-pavilion, an early steel tensile structure, also presented at the Panrussian Exposition 1896 d) The Multihalle, a large scale elastic gridshell, built in 1974-1975 e) The Weald and Downland elastic gridshell, built in 2002, f & g) The Savill building elastic gridshell, built in 2002 e) The Ephemeral Cathedral, an elastic glass fiber gridshell built, in 2013.

that an arch, which exhibits compression only, can be designed by inverting the shape of a catenary, which exhibits tension only. If buckling is neglected, compression-only or tension-only structures guarantee the highest possible material efficiency due to the uniform utilization of the material. Empiric form-finding also included designing membrane structures by studying soap films and copying their shapes.

More recent large-scale elastic gridshell examples are the Downland gridshell [Harris et al. 2003], the Savill Garden gridshell [Harris et al. 2008], and the Ephemeral Cathedral [Du Peloux et al. 2016] (cf. Figure 1.5). These examples demonstrate that elastic gridshells can produce large spans with little material input (from large to small): Multihalle 60m, Savill Garden 24m, Downland Museum 16m, Ephemeral Cathedral 15m [Bouleau et al. 2019].

The active-bending paradigm [Lienhard 2014] and improved simulation techniques sparked a wave of interest in large-scale elastic structures in the research community, resulting in many new concepts and research pavilions [Soriano et al. 2015; Tornabell et al. 2014; Fleischmann et al. 2011; Nicholas et al. 2013; Harding et al. 2015; Douthe et al. 2010]. Furthermore, the engineering community addressed the issue of deploying gridshells with novel techniques like inflatable air cushions [Quinn et al. 2014; Liuti et al. 2017; Quinn et al. 2018] and developed free-form elastic gridshell design methods [Douthe et al. 2010; Hernández et al. 2013; Adriaenssens et al. 2014a; Pone et al. 2013; Tayeb et al. 2013]. Finally, new ideas of deployable elastic gridshells with a scissor-like deployment mechanism were pioneered in the field of architecture [Soriano 2017; Soriano et al. 2019] and further developed and formalized in the fields of geometry and computer science [Panetta et al. 2019; Pillwein et al. 2020b; Pillwein et al. 2021b]. Due to the connection of elasticity to geometry and simulation, there is much interest in elastic grid structures in other scientific communities (cf. Section 1.6).

1.2.3 Structural Behavior

The mechanics of elastic gridshells are complex due to the interaction of elastically loaded members. Their geometrical resemblance to curved shells suggests that gridshells show similar structural behavior, which is partly the case and will be discussed below. In general, two structural mechanisms determine the load transport and the deflections in elastic gridshells: shell-action and pre-stressing due to elastic deformation.

Shells obtain their highest structural efficiency when designed to exhibit compression only. This type of load-bearing mechanism is called shell-action.

Such ideal shells are very rigid and have a high sensitivity to variations in their shape. If unanticipated loads (loads that induce bending) appear, shells deform very little until they suddenly collapse [Adriaenssens et al. 2014b]. The membrane theory of shells requires the following sufficient criteria to be fulfilled to avoid bending in a shell [T. Mitchell 2014; Sanchez-Palencia et al. 2010]:

- The boundary and the shape of the shell need to be designed in accordance. Purely elliptic shells with closed boundaries guarantee to avoid bending, while hyperbolic or parabolic shells do not.

- The boundary conditions (the supports) are continuous and designed only to transport axial forces (no clamped boundary).
- Loads are distributed smoothly (no point loads or discontinuities).

Although these rules seem to limit the design space to dome-like or blob-like shapes, the development of Thrust Network Analysis [Block et al. 2007] revealed an incredibly rich design space for compression-only shells and masonry vaults. The same applies to compression-only rigid gridshells [Kilian et al. 2017b; Millar et al. 2021]. However, the theoretical limits w.r.t. the thickness of shells can never be implemented in practice: Due to their high sensitivity towards bending, shells need to be designed conservatively to account for unanticipated loads and guarantee structural safety.

It seems contradictory to connect the structural behavior of elastic gridshells to shell-action, because bending is omnipresent in gridshells, and there is no resulting closed surface. However, due to their double curvature, a relevant portion of loads is transported via compressive forces in the grid members. Finding an elastic gridshell in a state close to shell-action is a chicken-and-egg situation: An elastic gridshell will approximate a target surface only to a certain degree, so even if the target surface allows pure shell-action, the gridshell will generally not be optimal because its shape is different. Hence, expensive joint shape optimization of the target surface and the grid would be required to reach material-minimizing states close to shell-action.

Elastic gridshells also benefit from the pre-stressing effect of bending and twisting members into place: The energy to produce the curvature and torsion is stored and causes an increase in the total stiffness of the structure, i.e., it answers to loads with smaller deflections.

As stated earlier, shells are rigid and deform very little until they collapse, i.e., they are form-passive [Adriaenssens et al. 2014b]. On the other hand, cables, membranes, or elastic gridshells are form-active: they are flexible to react to loads with considerable deformation, and hence avoid failure more easily. The collapse of elastic gridshells is furthermore announced by large deflections and does not happen suddenly. A known cause of failure are long-term material effects like creep, which increases the material's flexibility over time.

Undesired behavior emerges due to their slenderness: Elastic gridshells may react to loads with buckling, which must be considered thoroughly for their implementation, e.g., by studying buckling modes [Malek et al. 2014; Lefevre et al. 2015; Huang et al. 2022]. A common approach to increase their stiffness significantly and hence increase the resistance to buckling is introducing multiple structural layers and connecting them rigidly.

Furthermore, although there is a rich history of evaluating elastic gridshells with small-scale models, their structural behavior does not scale linearly with their size [Adriaenssens et al. 2014b; Pillwein et al. 2020a].

To discuss the in-plane and out-of-plane stiffness of gridshells, the idea of a virtual surface S through the deployed gridshell is convenient. The in-plane stiffness, i.e., the resistance against deformations in the tangent planes of S, is determined by the inextensibility of the grid members and the shearing resistance. The latter is produced by diagonal cables or rods. The out-of-plane stiffness is, loosely speaking, determined by the structural height of the gridshell: it increases with the dimension orthogonal to S. Strictly speaking, it is determined by the combined modulus of resistance of the single or multiple gridshell layers orthogonal to S.

After reviewing the structural behavior, one can conclude that elastic gridshells are suitable for specific applications which do not involve high external loads or require high structural stiffness. Furthermore, they are not especially material-efficient due to the large amount of bending in their members. However, they enable the design of free-form shapes very rapidly and cheaply, and their double curvature allows lightness and wide spans.

1.3 Geometry of Elastic Gridshells

The concept of a target surface connects elastic gridshells to the differential geometry of curves and surfaces. During form-finding, rods are idealized by curves on the target surface. Ensuring a close approximation of a specific target surface may not always be feasible, e.g., if the target surface has high-frequency curvature features, inner bumps or dents (positive extrema of the Gaussian curvature K), or non-smooth features. Whether a surface can be approximated well enough depends very much on the alignment of the grid and the curvature of individual members.

In a single member, oscillations in curvature usually correspond to high potential energy. If not properly restrained, the member will adopt a shape corresponding to a lower energy state, which may be far from the desired target surface. Remedying this with a high number of restraining supports reduces the practicality, and considering insights from shell theory, appropriate support locations are along the boundary. There are interesting approaches [Hafner et al. 2021] to realize single elements with oscillations in their curvature without introducing additional restraining supports. However, these approaches depend on planar centerlines and varying cross-sections along the rod, which is an excellent strategy, but hard to implement for nets of surface curves from a geometrical and fabricational point of view.

This section elaborates on the geometry of surface curves, curve frames, their connection to material frames of rods, and tangential strips along surface curves. It provides insights into some of the building blocks of shape correspondence with a target surface and their geometric background. Please note that geometric concepts will

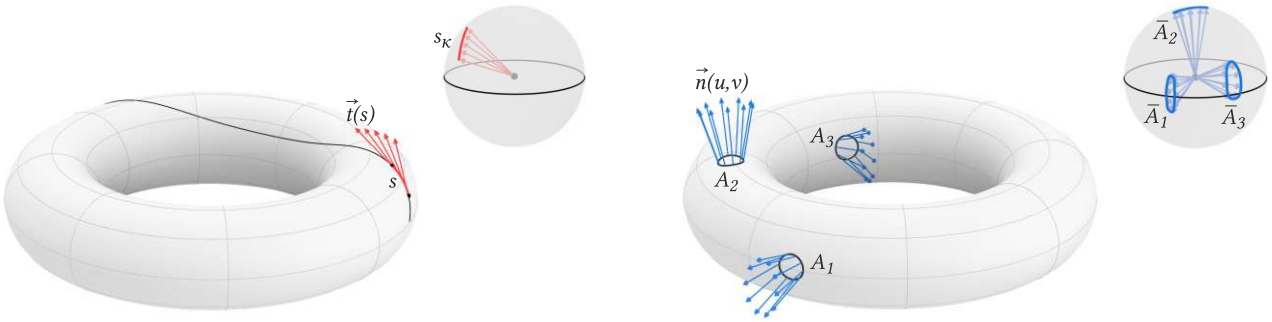

Fig. 1.6: Left: The spherical image of the tangents $\vec{t}(s)$ of a small arc around a point p on a curve $\gamma(s)$. The curvature κ at p can be computed as the limit of s_κ/s. Right: Small patches A_1, A_2, A_3 on a surface S(u,v) and the spherical images of their normals $\vec{n}(u,v)$. The magnitude of the Gaussian curvature K at p_1, p_2, p_3 can be computed as the limit of $\bar{A}/A$. Please note that $\bar{A}_2$ is curve-like, which indicates that p_2 is a parabolic surface point.

be discussed w.r.t. the smooth theory of differentiable curves and surfaces, but without strict mathematical rigor. A transfer to the discrete theory, which is employed for computational reasons to perform distance computations on the surface and simulations, is out of scope.

1.3.1 Curvature of Curves and Surfaces

The curvature κ of an arc-length parameterized curve $\gamma(s)$ in $\mathbb{R}^3$ measures the local directional change of the tangent vector $\vec{t}(s) = \gamma'(s)$ at a point $p = \gamma(s)$ w.r.t. arc-length s. The torsion τ measures the local directional change of the osculating plane, i.e., the local directional change of the binormal vector $\vec{b}(s)$, which is the unit vector of $\vec{t}(s) \times \gamma''(s)$ and therefore orthogonal to the osculating plane $[p, \vec{t}, \gamma'']$. To measure the magnitudes of κ and τ, one can resort to the spherical images of $\vec{t}(s)$ and $\vec{b}(s)$, and compare their respective arc-length s_κ and s_τ w.r.t. the arc-length s of the curve:

$$\kappa = \frac{ds_\kappa}{ds} = |\vec{t}'(s)| = |\gamma''(s)|\,,$$
$$|\tau| = \frac{ds_\tau}{ds} = |\vec{b}'(s)|\,.$$

The curvature κ of a spatial curve is not signed, i.e., $\kappa \geq 0$. A sign is attached to τ, w.r.t. the direction of the rotation of $\vec{b}(s)$ about $\vec{t}(s)$.

With a concept similar to curves, the local deviation of a surface $S(u,v)$ from its tangent plane at a point $p = S(u,v)$ can be measured. The Gaussian mapping $S(u,v) \to \vec{n}(u,v)$, with $\vec{n}$ being the surface's unit normal vector (i.e., the unit vector of $\partial S/\partial u \times \partial S/\partial v$), defines the spherical image of the surface on the unit sphere. Corresponding small regions with areas A and $\bar{A}$ on the surface around $p = S(u,v)$ and on the unit sphere around $\vec{n}(u,v)$ can be compared. The magnitude of the Gaussian curvature K at p is the limit of the ratio $\bar{A}/A$, if the areas shrink to zero. A sign is attached to K due to orientation: The Gaussian mapping induces a parameterization of the spherical image and therefore an orientation of its unit normal vector. If it agrees with $\vec{n}(u,v)$, K is positive, and otherwise negative.

A different approach to Gaussian curvature utilizes the normal curvatures κ_n at a surface point p. They measure the curvature of planar surface curves through p w.r.t. arbitrary tangent directions $\vec{t}$, where the curves' planes are orthogonal to the tangent plane at p. The normal curvature κ_n corresponding to $(p, \vec{t})$ is signed: It is positive if the surface normal $\vec{n}$ and the curve's principal normal $\vec{N}$ have the same orientation. As the orientation of $\vec{n}$ depends on the parametrization of the surface, so does the sign of κ_n. Generally, there are two extremal normal curvatures κ_1 and κ_2, with orthogonal directions $\vec{v}_1$ and $\vec{v}_2$, denoted as principal curvatures and principal directions, respectively. The connection between κ_1, κ_2, and κ_n is given by Euler's formula:

$$\kappa_n = \kappa_1 \cos^2\varphi + \kappa_2 \sin^2\varphi\,, \tag{1.1}$$

where φ is the angle between $\vec{v}_1$ and $\vec{t}$. The Gaussian curvature $K = \kappa_1\kappa_2$ is the product of the principal curvatures. The famous theorema egregium [Gauss 1828] states, that the Gaussian curvature belongs to the inner geometry of the surface. Hence, K is invariant under isometries, whereas the principal curvatures κ_1 and κ_2 are not.

Surface points with $K > 0$ are denoted as elliptic (S is locally egg-shaped), with $K < 0$ as hyperbolic (S is locally saddle-shaped), and with $K = 0$ as parabolic. At an elliptic point, the signs of κ_1 and κ_2 are the same, and therefore $\kappa_n = 0$ is not possible. If $\kappa_1 = \kappa_2$, all κ_n are equal, and the point is denoted as umbilical. At a hyperbolic point, the two directions corresponding to $\kappa_n = 0$ are determined by Equation 1.1 and are denoted as asymptotic directions. Only if $\kappa_1 = -\kappa_2$, they are orthogonal.

1.3.2 Surface Curves, Frames and Rods

The alignment of rods in an elastic gridshell w.r.t. the target surface is of significant importance. It is governed by curve frames and material frames of the centerlines of rods.

There are three specific unit vectors connected to each point p of an arc-length parametrized curve $\gamma(s)$: the tangent vector $\vec{t} = \gamma'(s)$, the principal normal vector $\vec{N}$ (aligned with the curvature vector $\gamma''(s)$), and the binormal vector $\vec{b} = \vec{t} \times \vec{N}$. This orthonormal basis is called the Frenet frame. The derivatives of the basis vectors with regard to arc-length are defined by the following linear combinations:

$$\begin{bmatrix} \vec{t} \\ \vec{N} \\ \vec{b} \end{bmatrix}' = \begin{bmatrix} 0 & \kappa & 0 \\ -\kappa & 0 & \tau \\ 0 & -\tau & 0 \end{bmatrix} \begin{bmatrix} \vec{t} \\ \vec{N} \\ \vec{b} \end{bmatrix} .$$

Thus, the shape of the curve is fully determined by the coefficients κ and τ.

If the curve lies on a surface, a further frame can be connected with the curve: The Darboux frame is spanned by the tangent vector $\vec{t}$, the surface normal vector $\vec{n}$, and a surface tangent vector $\vec{f}$, defined by $\vec{f} = \vec{n} \times \vec{t}$. The Frenet frame and the Darboux frame share the same basis vector $\vec{t}$, thus the former can be transformed into the latter by rotation about $\vec{t}$ by the angle $\beta = \beta(s) = \angle(\vec{b}, \vec{n})$, which can also be measured as angle between the osculating plane $[p, \vec{t}, \vec{N}]$ of the surface curve and the tangent plane $[p, \vec{t}, \vec{f}]$ of the surface (cf. Figure 1.7). As a consequence, the derivatives of the basis vectors with regard to arc-length are given by the following linear combinations:

$$\begin{bmatrix} \vec{t} \\ \vec{f} \\ \vec{n} \end{bmatrix}' = \begin{bmatrix} 0 & \kappa_g & \kappa_n \\ -\kappa_g & 0 & \tau_g \\ -\kappa_n & -\tau_g & 0 \end{bmatrix} \begin{bmatrix} \vec{t} \\ \vec{f} \\ \vec{n} \end{bmatrix} ,$$

$$\text{with } \kappa_g = \kappa \cos(\beta),\ \kappa_n = -\kappa \sin(\beta),\ \tau_g = \tau + \beta' .$$

The movement of the Darboux frame can be understood as succession of infinitesimal rotations about an axis through $p = \gamma(s)$, followed by an infinitesimal shift to a neighboring point $\gamma(s + ds)$. The skew-symmetric matrix defines these infinitesimal rotations.

To get an insight into the meaning of κ_g, κ_n and τ_g, the angular velocity vector $\vec{\Omega}$ can be employed. It defines the infinitesimal rotation at $p = \gamma(s)$ by its axis and angular velocity (magnitude of coefficients). In the Darboux frame, the local coordinates are $\vec{\Omega} = [\tau_g, -\kappa_n, \kappa_g]$. In the global coordinate system, $\vec{\Omega}$ is therefore given by the linear combination

$$\vec{\Omega} = \tau_g \vec{t} - \kappa_n \vec{f} + \kappa_g \vec{n} ,$$

where τ_g, $-\kappa_n$, and κ_g express the angular velocities of the rotations about the basis vectors $\vec{t}$, $\vec{f}$, and $\vec{n}$ separately. However, since rotations are non-commutative, the rotation about $\vec{\Omega}$ must not be interpreted as a sequence of rotations.

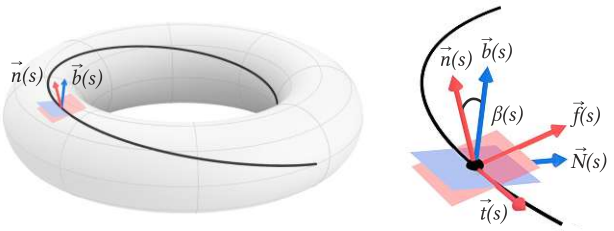

Fig. 1.7: Frames of a surface curve (Frenet in blue and Darboux in red) and the angle β. The blue plane depicts the osculating plane $[p, \vec{t}, \vec{N}]$ of the surface curve, the red plane depicts the tangent plane $[p, \vec{t}, \vec{f}]$ on S. Rotating the Frenet frame about the tangent $\vec{t}(s)$ with angle $\beta(s)$ aligns it with the Darboux frame.

The coefficients of the skew-symmetric matrix are denoted as geodesic torsion τ_g (rotation about $\vec{t}$), normal curvature κ_n (rotation about $\vec{f}$), which was already discussed in Section 1.3.1, and geodesic curvature κ_g (rotation about $\vec{n}$). The geodesic curvature κ_g measures, how much the curve locally turns sideways on the surface (i.e., how much it deviates from being as straight as possible). While κ_g is invariant under isometries (i.e., it belongs to the inner geometry of the surface), the normal curvature κ_n is not. The relation between the curvatures κ, κ_n, and κ_g of surface curves results from comparing $\vec{t}'$ in the Frenet and Darboux frames:

$$\left\| \vec{t}' \right\| = \kappa = \sqrt{\kappa_g^2 + \kappa_n^2} .$$

It is possible, that either τ_g, κ_n, or κ_g vanishes along a surface curve. These special curves are interesting for many reasons:

- Geodesic curves ($\kappa_g = 0$): They are as straight as possible on the surface and thus correspond to the straight lines in the plane. Their principal normals $\vec{N}$ coincide with the surface normals $\vec{n}$. They are always locally length-minimizing, while this may not be the case globally.
- Asymptotic curves ($\kappa_n = 0$): They exist only on hyperbolic patches (i.e., patches with $K < 0$), where two of them pass through each point. Their principal normals $\vec{N}$ lie in the tangent planes.
- Curvature lines ($\tau_g = 0$): Generally, two of them pass through each point p, regardless of the sign of the Gaussian curvature, and intersect orthogonally. Their respective normal curvatures κ_1 and κ_2 are extremal under all normal curvatures at p.

As for the implementation of gridshells, asymptotic and geodesic curves share a common property: Both allow implementations with thin straight lamellas, which in the case of asymptotic curves are placed orthogonally to the surface [Schling et al. 2018; Schikore et al. 2021], and for geodesic curves tangentially [Pillwein et al. 2020b].

To describe a deformed rod, an orthonormal material frame analogous to the frames mentioned before can be used. It is spanned by the tangent vector $\vec{t}$ of the rod's centerline, and two material vectors $\vec{m}_1$ and $\vec{m}_2$ for the orientation of the rod's cross-section. The derivatives of the basis vectors can be written in perfect analogy to the Darboux frame:

$$\begin{bmatrix} \vec{t} \\ \vec{m}_1 \\ \vec{m}_2 \end{bmatrix}' = \begin{bmatrix} 0 & \omega_1 & \omega_2 \\ -\omega_1 & 0 & m \\ -\omega_2 & -m & 0 \end{bmatrix} \begin{bmatrix} \vec{t} \\ \vec{m}_1 \\ \vec{m}_2 \end{bmatrix} .$$

Again, the coefficients ω_1 and ω_2 decompose the curvature κ of the centerline, whereas the coefficient m corresponds to the geodesic torsion:

$$\omega_1 = \vec{t}' \, \vec{m}_1 \ , \ \ \omega_2 = \vec{t}' \, \vec{m}_2 \ , \ \ m = \vec{m}_1' \, \vec{m}_2 = -\vec{m}_2' \, \vec{m}_1 \, .$$

To simulate rods, discrete geometry is employed: The centerlines are polylines, and the material frames operate on its edges. However, the underlying geometric relations stay the same.

The alignment of the Frenet frame and a material frame along the rod's centerline can be coupled by stiffness parameters of the cross-section [Bergou et al. 2008]. Proper choice of these parameters opens up a large space of shapes [Panetta et al. 2019; Hafner et al. 2021]. This connection can be understood by examining the bending energy of an initially straight rod with a smooth centerline:

$$E_{bend} = \frac{1}{2} \int \left[\omega_1, \omega_2\right] \mathbf{B}(s) \left[\omega_1, \omega_2\right]^T ds \, ,$$

where the stiffness matrix $\mathbf{B}(s) = E\mathbf{I}(s)$ is the product of the elastic modulus E of the material and the moment of intertia tensor $\mathbf{I}(s)$, which accounts for the shape of the cross-section, and ω_1 and ω_2 are the projections of the curvature κ of the centerline onto the material directions. To virtually prohibit curvature in a material direction $\vec{m}_1$ or $\vec{m}_2$, lamella-like rectangular cross-sections are convenient, since their moment of inertia for one of these directions is very big.

The discussion of surface curves and material frames reveals the strong connection between geometric properties and shapes of cross-sections. Closely approximating a target surface using an elastic grid is achievable if the frames of the surface curves and the rod's material frames agree.

1.3.3 Geodesics

Due to their straightness ($\kappa_g = 0$), geodesics are valuable tools, e.g., to define patterns on surfaces [Pottmann et al. 2010], straight tangential strips [Wallner et al. 2010], the layout for triaxial weaves [Vekhter et al. 2019], or gridshells with geodesic members [Harding et al. 2015; Adiels et al. 2018].

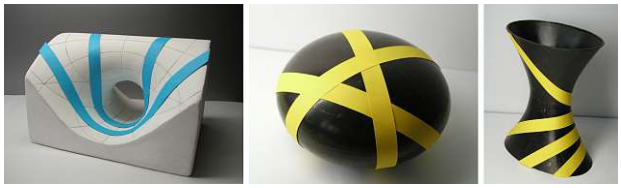

Fig. 1.8: Examples of paper strips "glued" to the surfaces. The centerlines of the strips follow geodesic curves on each surface. A sufficiently small strip can follow any geodesic with non-vanishing curvature. Adapted from [Pottmann et al. 2015].

Finding geodesics on surfaces is a long-standing and still active research topic with a rich theory in differential geometry. Start-and-direction geodesics continue straight from a given initial point and an initial direction. Start-and-end geodesics connect two given points with $\kappa_g = 0$. A shortest geodesic is globally shortest among all start-and-end geodesics between two points. Please note that the shortest possible curve between two points which does not contact the surface boundary is always a shortest geodesic. The former type (start-and-direction) is unique for every combination of initial point and direction, while the latter one (start-and-end) generally is not.

Shortest geodesics between two points receive special attention since their trajectory is more manageable than the trajectory of start-and-direction geodesics. As for a given start point, finding the precise direction that yields a start-and-direction geodesic through a desired endpoint is hard. The problem of finding shortest geodesics is closely related to distance fields, which can be computed using a variety of methods. Please refer to Section 1.6 for an overview.

The uniqueness of shortest geodesics strongly depends on the Gaussian curvature K of the surface. Intuitively arguing, a shortest geodesic will likely lead around any high-curvature bump between the start and end point, simply because all paths over the bump are not shortest. A further connecting geodesic might lead over the bump, and a third one might avoid the bump on the other side. The shortest geodesic and the third one may even have equal length. Thus, there can be two shortest geodesics between the start and end point, which are denoted as cut points in this case. Please refer to Section 3.4.1 for a more detailed discussion and depiction of this phenomenon. The occurrence of cut points depends on the magnitude, variation, and sign of K, and the location of the start and end points. It is very difficult to check if surfaces are fully coverable with families of shortest geodesics connecting points on the surface's boundary, and so far, only rough estimates are used [Pillwein et al. 2020b]. Nevertheless, shortest geodesics are convenient for the form-finding of elastic structures, especially when the Gaussian curvature is negative or low enough.

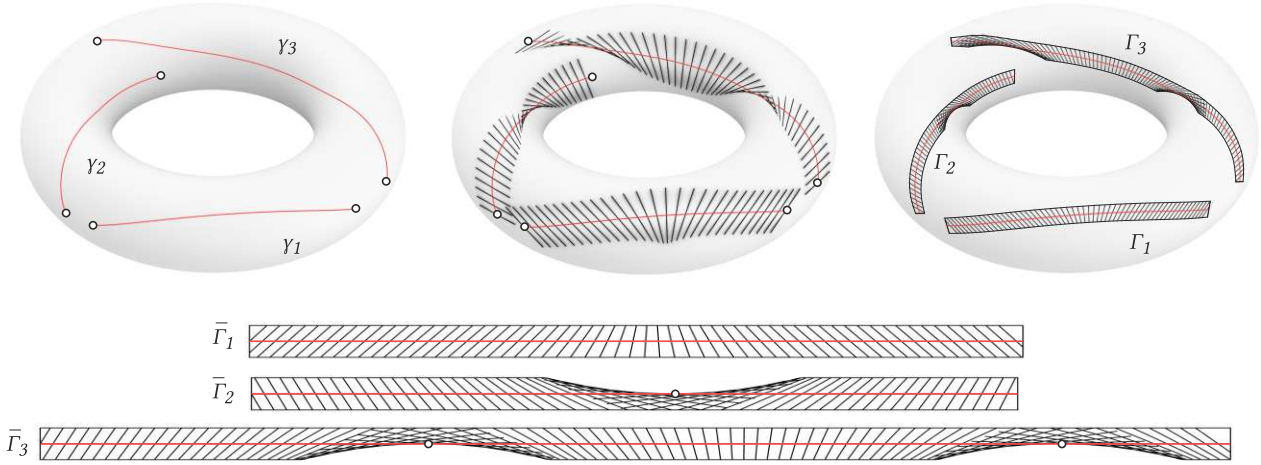

Fig. 1.9: Truly developable strips $\Gamma_1, \Gamma_2, \Gamma_3$ and their generators on a surface along geodesics. The strips Γ_2 and Γ_3 fold over on themselves along a crease curve. The marked points correspond to the location of $\kappa_n = 0$, where the generator aligns with the tangent.

1.3.4 Tangential Strips

Along every surface curve $\gamma(s)$ a corresponding developable tangential strip can be defined. Such a strip is enveloped by the surface's tangent planes along γ, and its generators $\vec{g}(s)$ are conjugate to the curve's tangents $\vec{t}(s)$ [Wallner et al. 2010]. When unfolding such a strip to the plane, its centerline does not need to become straight, as its curvature is the surface curve's geodesic curvature κ_g (i.e., the intrinsic part of the curve's curvature κ). Inversely, the planar strip can be wrapped onto the surface, with the generators $\vec{g}(s)$ as bending axes. Their directions are the limits of the intersection lines of the tangent planes at neighboring points $\gamma(s)$ and $\gamma(s+ds)$ (cf. Figure 1.10). To derive $\vec{g}(s)$ mathematically, one can utilize that the intersection line has the direction of the cross product of the respective surface normals $\vec{n}(s)$ and $\vec{n}(s+ds)$:

$$\vec{n}(s) \times \vec{n}(s+ds) = \vec{n}(s) \times (\vec{n}(s) + d\vec{n}) = \vec{n}(s) \times d\vec{n} \quad \Big|\tfrac{1}{ds}$$
$$\vec{n}(s) \times \frac{d\vec{n}}{ds} \overset{ds\to 0}{=} \vec{n}(s) \times \vec{n}'(s)\,,$$

and subsequently derive $\vec{g}(s)$, using the derivative equations of the Darboux frame:

$$\vec{g}(s) = \vec{n}(s) \times \vec{n}'(s) = \vec{n}(s) \times (-\kappa_n \vec{t} - \tau_g \vec{f}) = -\kappa_n \vec{f} + \tau_g \vec{t}\,.$$

Please note that $\vec{g}(s)$ is the orthogonal projection of the angular velocity vector $\vec{\Omega}$ of the Darboux frame onto the tangent plane at $p = \gamma(s)$.

Wrapping the tangential strip onto the surface requires only bending along the generators $\vec{g}$, which are precisely the strip's bending axes. Through this process, the centerline automatically obtains curvature and torsion.

Aspiring straight strips, geodesics are the perfect choice due to $\kappa_g = 0$. In fact, any straight strip with a sufficiently small width (with edges parallel to the centerline) can be wrapped onto a surface along its centerline, which automatically will always be a geodesic. Please note that for geodesics the equations $\tau = \tau_g$ and $\kappa = |\kappa_n|$ hold. If the geodesic is a planar curve, the generators $\vec{g}$ are orthogonal to it. If it exhibits torsion (general case), the construction of the strip may become problematic: The higher the ratio of torsion τ_g to curvature κ_n, the more inclined the generators become (cf. Figure 1.9).

Extending the generators of a strip provides interesting insights. On this extended developable surface, they envelop a ridge curve. The distance of this curve to the geodesic centerline determines the maximum feasible width of the tangential strip. Introducing strips with higher widths results in tangential strips which fold back on themselves along the ridge curve. In the worst case, the geodesic has an inflection point ($\kappa = \kappa_n = 0$), where the generator $\vec{g}(s)$ is aligned with the tangent $\vec{t}(s)$. As the centerline of the strip is now tangential to the ridge curve, the maximal width of the strip is zero. Hence, developable strips may need a variable width, which may become zero.

In practice, this geometric problem can be bypassed by compromising on strict developability and using materials that allow a small amount of in-plane stretching, which enables twisting additionally to bending (unlike paper). For such cases, the binormal model [Wallner et al. 2010] is suitable. It proposes using a non-developable strip defined by the surface tangents orthogonal to the geodesic (i.e., the binormals of the geodesic), omitting the computation

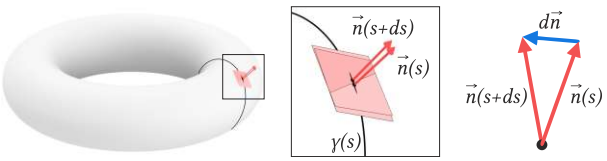

Fig. 1.10: Geometric construction of the generators $\vec{g}$. Intersecting adjacent tangent planes at $\gamma(s)$ and $\gamma(s+ds)$ yields a line which converges to the generator $\vec{g}(s)$.

of conjugate surface tangents. This model requires a certain amount of stretching of the strip's edges, which is directly linked to the torsion τ of the geodesic centerline. The length of the stretched edges can be computed using Frenet's formulas:

$$l + \Delta l = \int_0^l \sqrt{1 + \left(\frac{w}{2}\,\tau(s)\right)^2}\, ds\,,$$

where l is the length of the centerline and w is the strip's width. The binormal model is also closely related to the simulation of discrete elastic rods [Bergou et al. 2008; Bergou et al. 2010], where length changes by twisting are not penalized.

In this thesis, the binormal model performed well since the materials used to build elastic geodesic grids (wood or glass fiber reinforced plastics) allow for a tiny amount of in-plane stretching.

1.3.5 Transformable Grids

Elastic gridshells build upon the transformation of an initially planar grid to a spatial, curved shape. The main instrument to perform such a transformation is changing inner angles of the grid. Although such a collective strategy exists, there are different classes of transformable grids with different underlying geometric assumptions. This section discusses discrete Chebychev nets, Chebychev-related elastic nets, and scissor-like deployable geodesic grids.

The main constraint for deployable grids is prohibiting the stretching or contracting of the centerlines of members. This is reminiscent of Chebychev nets. In the smooth world, a Chebychev net is sampled from parameter lines of a surface parametrization with $E = G = 1$. A discrete Chebychev net is a quadrilateral grid of finite resolution with polylines as member curves δ and edges e of uniform length. The edges can rotate freely around their vertices, but the lengths of the edges are preserved. There is great freedom to find discrete Chebychev nets on surfaces, e.g., by using two guiding curves [Koenderink et al. 1998], or vector fields [Sageman-Furnas et al. 2019]. However, finding such nets on arbitrary surfaces inevitably results in singularities, and finding nets with only a few of them is an active field of research. Singularity-free discrete Chebychev nets can always be transformed into the plane by appropriately changing the interior quad angles [Koenderink et al. 1998].

Imagining a similar net of some fixed resolution, but with elastic and therefore smooth grid lines, the net has quite different kinematics. Again, arc-lengths of the members between their joints do not change. But, due to the elasticity of the members, changes in inner angles of the grid propagate through the whole grid (cf. Figure 1.11), whereas in discrete Chebychev nets, such changes remain local. Although the shape of Chebychev-related elastic nets is not determined by a single degree of freedom, i.e., a single angle in the grid, but local changes of angles add to the overall shape. This behavior can be understood by considering members elasticae, which adapt their shape by minimizing the following functional:

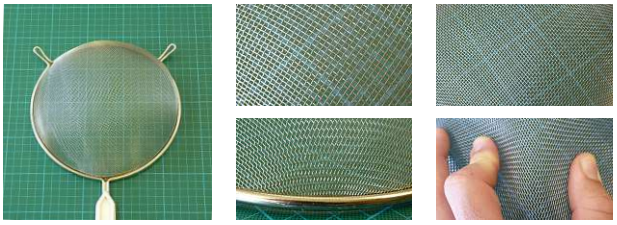

Fig. 1.11: A household strainer as an example for a Chebychev-related elastic net. When unconstrained, the metal mesh is completely flat. By changing interior angles, doubly curved shapes are viable.

$$E_\delta = \frac{1}{2}\int \alpha\kappa(s)^2 ds\,,$$

where α is a parameter similar to the stiffness matrix $\mathbf{B}$ of a rod, κ is the member's curvature, and s its arc-length.

A related approach [Panetta et al. 2019] builds on the idea of creating curved grids through local changes of angles by loading its joints with different amounts of torque. Please note that the grid layouts used in this approach are, however, geometrically not related to Chebyshev nets.

After deploying Chebychev-related elastic nets, the axes of rotation through their joints are generally not perpendicular to the target surface. The principal normals $\vec{N}$ of grid members are generally not aligned with the respective surface normals $\vec{n}$, which is only the case if members are geodesics.

Scissor-like deployable geodesic grids are also quadrilateral grids of flexible members which preserve the lengths of member curves δ. However, as their spacing is not uniform, they are not Chebychev-related elastic nets. Their lamella-like members reduce the kinematic mechanism to a single degree of freedom. In other words, changing one angle controls their shape globally, and no local changes of interior angles are feasible without breaking the grid. This behavior is due to the significant resistance of the lamellas in one of the material directions, which effectively prohibits in-plane bending. Similar to the former type of grids, isometric bending of a deployed grid is feasible, leading to a family of shapes for each grid. Please note that for elastic geodesic grids (as described in Section 1.1) elongated holes are necessary if the deployed grid should agree closely with a given target surface.

1.4 Simulation and Validation

Well-established mathematical models, like the Discrete Elastic Rods (DER) model, are well suited to simulate the shape of assemblies of elastic objects. Rod simulation

techniques need to be fast, especially for form-finding, where different layouts must be evaluated repeatedly. Simplifications of the elements' geometry and the physical principles that govern elastic deformation guarantee the speed and robustness of simulation techniques at an acceptable loss of accuracy. Such techniques represent volumetric elements by polylines as their centerlines, and material frames assigned to the edges of the polylines, representing the orientation of the cross-sections. There are numerous approaches to determine the equilibrium of such structures, which function by either minimizing geometric energies like the Discrete Elastic Rods model [Bergou et al. 2008; Bergou et al. 2010], or minimizing out-of-balance forces [D'Amico et al. 2015; Lefevre et al. 2017; Sakai et al. 2020]. In the former case, physical constraints like joints require the formulation of additional energy terms, resulting in a mix of geometric energies, which are only loosely related to the elastic energy of the structure. Unfortunately, external forces like loading cannot be applied directly in simulation techniques that depend on geometric energies. However, these techniques are computationally very robust and efficient. Despite apparent advantages, 1d rod simulation techniques do have some shortcomings: Geometrically non-linear effects like helix strain or buckling of local regions of the cross-section cannot be analyzed. Furthermore, the weakening of cross-sections by holes cannot be handled, which is a significant source of failure for built gridshells.

One can even go further and ask if the simulation can be partly circumvented using geometric considerations only. Although the interaction of the elastic members is complex, some geometric designs can easily be discarded by analyzing the curvature and torsion of the curves on the target surface. Holding, for example, a thin metal lamella at its ends and bending it, it is pretty hard to produce more than one inflection point if the strip is not constrained further (e.g., by a helping hand). Heuristics based on such geometric insights clearly do not provide the same comprehensive rigor in information as simulating the equilibrium shape. However, if heuristic rules for good shape correspondence can be identified, such approaches bear the potential for significant speed-ups [Pillwein et al. 2021b].

It shall be noted that implementing elastic gridshells on a large scale requires in-depth Finite Element Analysis (FEA), featuring geometric and material non-linearity and proper volumetric representations of the elements.

1.5 Thesis Objectives and Contributions

This thesis features three publications (**P1**,**P2**,**P3**), all related to the form-finding of elastic geodesic grids. The proposed approaches aim at approximating free-form surfaces with spatial grids of bent lamellas, which can be deployed from a planar configuration using a simple scissor-like kinematic mechanism.

1.5.1 Outline of Publications

On Elastic Geodesic Grids and Their Planar-to-Spatial Deployment (P1) proposes the approximation of free-form surfaces using scissor-like deployable elastic grids. The design algorithm is based on geodesic curves and produces specific planar layouts for different target surfaces, encoding the shape of the surface into the planar layout. The design pipeline is semi-automatic, where the user defines a target surface bordered by a convex geodesic quadrilateral to be approximated, obtains a sparse base layout, and can successively choose to densify it. The paper further investigates theoretical constraints on transforming geodesic grids to the plane without stretching, and overcomes them by introducing particular sliding connections called notches. The method is intended as a form-finding tool for elastic gridshells in architecture and other creative disciplines, and should give the designer an easy-to-handle tool to explore such structures.

Authors: Stefan Pillwein, Kurt Leimer, Michael Birsak and Przemyslaw Musialski; *Published in:* ACM Transactions on Graphics, Vol. 39, No. 4, July 2020.

Design and Fabrication of Multi-Patch Elastic Geodesic Grid Structures (P2) proposes improvements in the space of admissible design surfaces, like surfaces with high local Gaussian curvature or non-geodesic boundaries, which a single elastic geodesic grid cannot cover. The paper demonstrates, how decomposing such surfaces into smaller patches is an effective strategy to tackle these problems. Finally, it presents a showcase model of some meters in size, and discusses practical aspects like fabrication, size, and easy deployment.

Authors: Stefan Pillwein, Johanna Kübert, Florian Rist and Przemyslaw Musialski; *Published in:* Computers & Graphics, Vol. 98, August 2021.

Generalized Deployable Elastic Geodesic Grids (P3) revisits the concept of elastic geodesic grids from a new perspective: The combinatorics of the grids are not restricted to quads, and boundaries of design surfaces may even be non-convex. This generalization requires strategies to prohibit invalid grid members, i.e., shortest curves which touch the boundary and are therefore no geodesics, and update the grid combinatorics accordingly. It further introduces a well-defined elastic grid energy functional that allows identifying networks of curves that minimize the bending energy and, simultaneously, nestle to the provided target surface well. To get results fast, it omits simulating the equilibrium shape, relying instead on a geometrically motivated heuristic.

Authors: Stefan Pillwein and Przemyslaw Musialski; *Published in:* ACM Transactions on Graphics, Vol. 40, No. 6, December 2021.

1.5.2 Contributions

The contributions of this thesis are the following:

- We identify a specific case of the inverse design problem of spatial elastic grids, which can be formulated using geometric considerations only. This formulation allows us to find a perfectly planar grid that can be deformed in an elasto-kinematic manner to a desired spatial grid, which approximates a given target surface closely. (**P1**)
- We derive a mathematical method for form-finding of such geodesic grids, based on the differential-geometric properties of geodesic curves. In particular, we introduce *distance maps* and *cladding functions*, which allow for an efficient and fast calculation of suitable configurations without expensive numerical shape optimization. (**P1**)
- We introduce rules for decomposing large and challenging input surfaces, which can have holes and non-convex boundaries, into many individual patches. We apply this strategy to three examples of free-form architecture, and show, that between the patches continuity of members is feasible. (**P2**)
- We introduce a second, independent mathematical method to find elastic geodesic grids, based on a well-defined energy functional, which allows us to identify so-called *least-effort* and *most-effort* geodesics on the surface, which ensure capturing the surface characteristics well and provide aesthetic grid layouts. (**P3**)
- More sophisticated target surfaces may exhibit boundaries that are non-convex. Possibly, there are even multiple non-convex regions. This implies that the planar configuration becomes more intricate, hosting sub-families of members, and poses the challenge of varying-connectivity grids. We propose an efficient algorithm, based on distance computations only, that updates the combinatorics of the grids. (**P3**)
- A crucial requirement of deployable structures is the perfect planarity of the undeployed state. This requirement is important for the ease of fabrication, transportation, and assembly, and should not be underestimated, as dealing with bent elements is considerably more difficult and expensive than with planar ones. We introduce a generic planarization algorithm, independent of grid combinatorics, that also considers fabrication constraints. (**P3**)
- Finally, we introduce physical simulation and a simple fabrication method for wooden elastic geodesic gridshells, and perform empirical measurements that prove our approach's validity. (**P1**,**P2**,**P3**)

1.6 Related Work

For the reader's convenience, this section presents a consolidated and revised version of the related work from the author's publications [Pillwein et al. 2020b; Pillwein et al. 2020a; Pillwein et al. 2021b].

Developable Surfaces. Due to their vanishing Gaussian curvature, developable surfaces are isometric to the plane, which is convenient from a theoretical and practical point of view.

Nets of geodesics are intrinsically unaffected by isometries, i.e., they remain geodesics, and their lengths and intersection angles stay unchanged. These properties provide valuable constraints to model developable surfaces and their isometric deformation based mathematically on orthogonal nets of geodesics [Rabinovich et al. 2018a; Rabinovich et al. 2018b; H. Wang et al. 2019].

Computationally exploring curved folding is a closely related area with a lot of research interest. Introducing curved creases on developable surfaces involves strategies to connect patches along the creases and ensure their developability individually by introducing multiple discrete orthogonal geodesic nets [Rabinovich et al. 2019], or by identifying and utilizing the ruling directions of the planarized patches [Kilian et al. 2008; Tang et al. 2016; Verhoeven et al. 2022]. Curve-pleated structures [Jiang et al. 2019] permit approximating curved surfaces by introducing fold patterns for curved creases based on pseudogeodesics.

The geometry of paper crumpling was also explored [Schreck et al. 2016], where sharp features emerge when the sheet is crumpled by computationally linking a finite element simulation step and a remeshing step, which ensures developability. Another recent approach to model developable surfaces is via isometric mappings between surfaces as correspondences between checkerboard patterns [Jiang et al. 2020b], allowing for cutting, gluing, or folding along curved creases.

Approximating free-form surfaces with assemblies of developable surfaces, which can be bent and combined, is a related research question. There is a wide variety of approaches involving geodesics to define tangential patches and combining them [Ion et al. 2020], thinning of Gauss images of surface patches [Binninger et al. 2021], variational approaches that modify meshes toward developable patches [Stein et al. 2018], or making heightfields piecewise developable by minimizing the rank of their Hessian [Sellán et al. 2020].

Approximating free-form surfaces with developable strips [Wallner et al. 2010; Pottmann et al. 2010; Eigensatz et al. 2010; Tang et al. 2016; Mitani et al. 2004] or panels [Gavriil et al. 2019; Y. Liu et al. 2011; Pellis et al. 2020] is a typical application, which is economically highly relevant in the field of architectural geometry and product design [Pottmann et al. 2015; D. Chen et al. 2013].

Deployable Surfaces and Structures. A simple way to create spatial shapes from flat sheets is by appropriately folding paper [Mitani et al. 2004; Massarwi et al. 2007], which is inherently related to the Japanese art of Origami [Dudte et al. 2016]. This technique also allows for the approximation of free-form surfaces, as every polyhedral surface can be folded from a sufficiently large square of paper [Demaine et al. 2017]. The art of Kirigami involves folds and cuts and enables corrugated surface representations isometric to the plane [Jiang et al. 2020a].

Auxetic materials feature a negative Poisson's ratio, enabling them to expand orthogonally to a given stretching direction. This is due to their elaborate internal geometric structure, which features openings and rotational joints. Such materials can nestle to doubly-curved surfaces [Konaković et al. 2016; Konaković-Luković et al. 2018], while being produced from planar sheets of material. Auxetics may even take multiple stable states, as recent advancements in bi-stable structures show [T. Chen et al. 2021].

Elastically Deployable Surfaces and Structures. A compelling way to deploy surfaces is to utilize the energy stored in planar configurations in order to approximate shapes, for instance, using prestressed latex membranes in order to actuate precomputed planar geometric structures into free-form shapes [Guseinov et al. 2017], or to predefine flexible micro-structures which deform to desired shapes if appropriate boundary conditions are applied [Malomo et al. 2018; Laccone et al. 2019]. Another approach is to combine elastic rods and membranes, leading to Kirchhoff-Plateau surfaces that allow easy planar fabrication and deployment [Pérez et al. 2017]. Related approaches explore programmable materials [Tozoni et al. 2020], or rod networks [Pérez et al. 2015] that deform to controllable states when deformed. Shape morphing mesostructures [Guseinov et al. 2020] even evolve to doubly-curved surfaces over time.

Surface-based inflatable structures [Panetta et al. 2021] utilize expanding tunnels, fabricated by fusing two layers of thin material to approximate surfaces. Layouts are found by including the bending energy stored in the tunnels.

Introducing elements with variable stiffness enables a wide range of target equilibrium shapes. This space was recently characterized for elements that are only constrained at their boundaries, using a method to determine physically viable shapes by the idea of visual inspection [Hafner et al. 2021].

Weaving approaches are closely related to elastic gridshells, which also employ thin elastic strips. Form-finding techniques vary from geodesic weaves [Vekhter et al. 2019] to weaves with curved strips [Ren et al. 2021]. A similar approach to weaving is the division of shapes into principal strips, which bend automatically if combined [Takezawa et al. 2016].

Wire Structures. Wires are convenient to abstract spatial shapes, either by plastic deformation and assembly [Miguel et al. 2016; Yang et al. 2021; Lira et al. 2018] or by combining them with elastic springs of variable stiffnesses to create kinetic wire characters [Xu et al. 2018].

Wire meshes are closely related to Chebyshev nets and are well suited to approximate doubly-curved surfaces [Garg et al. 2014; Sageman-Furnas et al. 2019; H.-Y. Liu et al. 2020]. Permanently deforming such wire meshes to approximate the target shapes requires plastic deformation.

Wire mesh approaches, which build on pure elastic material behavior, are closely related to elastic gridshells and have been explored and simulated [Baek et al. 2018; Baek et al. 2019]. Due to their elasticity and lightness, such wire meshes were even used for heavy-duty applications such as for the tires of the the Lunar Roving Vehicles [Asnani et al. 2009], and as candidates for probe-tires on other planets.

Rigid Free-form Surfaces. Many methods which aim directly at the computational design of physically sound and stable architectural structures have been proposed, e.g., the design of self-supporting masonry surfaces [Block et al. 2007; Vouga et al. 2012; Panozzo et al. 2013]. Also, the process of the erection of such objects has been computationally explored [Deuss et al. 2014]. Moreover, methods for fast interactive form-finding of physically stable structures [Tang et al. 2014], for physically plausible tensegrity structure design [Pietroni et al. 2017], or the minimization of material usage under stability constraints [Kilian et al. 2017b] have been proposed.

Elastic Gridshells. Structures that gain strength and stiffness through their curvature have been used in architecture and design for millennia [Lienhard et al. 2013]. This form of structure erection has been summarized in the architecture and construction literature as the active-bending paradigm [Lienhard et al. 2013; Lienhard et al. 2018]. Modern and easy-to-use computational methods increased the scientific community's interest in systematically utilizing elastic bending to realize curved shapes. Architectural works aim to approximate free-form surfaces with gridshells to combine lightweight structural design with aesthetics [Soriano 2017; Soriano et al. 2019], and are often based on particular kinds of surface curves, such as asymptotic curves [Schling et al. 2018; Schikore et al. 2021; Schling et al. 2022]. The engineering community is less focused on producing stunning designs but on systematizing form-finding and simulating elastic gridshells which are based on Chebychev nets [Douthe et al. 2010; Quinn et al. 2014; Hernández et al. 2013; Pone et al. 2013; Tayeb et al. 2013]. A central constraint for all these approaches is that structural members do not stretch or contract, which is useful in their form-finding, but has far more profound importance: In fact, the zeroth-order shape

of an elastic gridshell is determined by rod inextensibility, not the elastic bending of members [Baek et al. 2018].

Scissor-like Deployable Gridshells. Simple deployment makes grid structures easy to fabricate and use. Thus, a lot of research activity went into finding deployment mechanisms. Several different deployment strategies exist: erecting a scaffolding and bending the grid down, lifting the grid by cranes, lifting the grid by inflatable air cushions [Quinn et al. 2014; Liuti et al. 2017; Quinn et al. 2018], or employing scissor-like mechanisms encoded in the grid [Panetta et al. 2019; Soriano et al. 2019; Pillwein et al. 2020b; Haskell et al. 2021; Schikore et al. 2021]. Scissor-like deployable elastic grids produce curved shapes by systematically harvesting buckling: The members in the flat layouts cannot be transformed in the plane without changing lengths, but due to their flexibility the grids may buckle and create spatial, curved shapes. This idea was explored for assemblies based on geodesics and other curves.

To create an X-Shell [Panetta et al. 2019], a planar grid layout is designed using curved or straight members, and actuated via physical simulation. The approach does not require a target surface, the space of feasible shapes can simply be explored iteratively: In multiple layout iterations, the designer finds a satisfactory shape by adapting the planar layouts and evaluating the deployed shapes. Target surfaces can, however, be approximated by using shape optimization (presuming a good planar initialization). The practical feasibility of these structures was investigated with the construction of a pavilion [Isvoranu et al. 2019].

The G-Shells approach [Soriano et al. 2019] proposes to planarize a specific geodesic grid using physical simulation and an evolutionary multi-objective solver. Unfortunately, length-preserving mappings of geodesic nets on a surface onto geodesic nets in the plane are generally not possible [Lagally 1910]. Ignoring this finding induces a geometric error, producing deviations of the computed grid w.r.t. the target geodesic grid and the target surface. Please refer to Figure 1.3 for a depiction. Two well-known examples of surfaces are feasible using this method: the hyperbolic paraboloid and the one-sheeted hyperboloid. Apart from these examples, the space of realizable shapes for this method is still unclear.

In contrast to the former approaches, elastic geodesic grids [Pillwein et al. 2020b; Pillwein et al. 2021a; Pillwein et al. 2021b] use the concept of notches, which prevents the geometric error in the grid layout and allows for a very close approximation of a target surface. However, it also makes deployment more complicated, as sliding of members is necessary. The method takes a design surface as input, and produces a deployable and perfectly planar grid layout.

Shortest Geodesics and Distance Fields. Geodesics are defined as surface curves with vanishing geodesic curvature ($\kappa_g = 0$). If the shortest connection between two surface points does not touch the surface's boundary, it is always a geodesic, denoted as shortest geodesic between the two points. Due to their inherent connection to distances on the surface, shortest geodesics are closely related to distance fields, which will be reviewed in the following. The methods for computing shortest geodesics can be classified into three categories: computational geometry methods, PDE methods, or graph-based methods. Please refer to [Crane et al. 2020] for a comprehensive study of current approaches.

Computational geometry methods build on measuring distances on flattened triangle strips based on the MMP or the CH algorithms [J. S. Mitchell et al. 1987; J. Chen et al. 1990]. This basic approach has seen many improvements in efficiency, either by optimizing the propagation of the algorithm through the mesh [Xin et al. 2009; Qin et al. 2016; Han et al. 2017; Surazhsky et al. 2005], parallelization [Ying et al. 2019; Ying et al. 2014], or creative geometric simplification of the original algorithms at some loss of accuracy [Trettner et al. 2021]. These approaches internally build a data structure, using so-called windows, which are segments on edges, and store data, such as the distance to the source. Using this data, the shortest path (i.e., the shortest geodesic) can be traced back from any point on the mesh to the source.

A distance field is a function u on a surface and can be defined as a PDE w.r.t. the length of its gradients: it needs to obey the Eikonal Equation $||\nabla u(x)|| = 1$. PDE methods intend to solve the Eikonal Equation on triangle meshes. While the isolines of such a function are curved, the FMM method [Sethian 1999] assumes linear isolines in each triangle, yielding approximations of geodesic distances, which become more accurate the farther the considered triangles are away from the source. The method was also improved w.r.t. the handling of acute triangles [Xin et al. 2007]. Another PDE approach substitutes solving the Eikonal equation with solving the heat equation and a Poisson equation [Crane et al. 2013], which both can be solved by linear systems of equations on triangle meshes. However, the quality of the solution depends on a time integration variable and the anisotropy of the mesh.

Graph-based methods [Ying et al. 2013; Adikusuma et al. 2020; X. Wang et al. 2017] build an undirected graph on the mesh, such that shortest paths on the mesh become shortest paths in the graph. Graph shortest paths can subsequently be found fast, using Dijkstra's algorithm [Dijkstra et al. 1959].

Besides the before-mentioned, window-based approaches, geodesics can also be traced using curve-shortening approaches [Sharp et al. 2020; Xin et al. 2007], which can, however, only ensure to deliver locally shortest geodesics.

Chapter 2

On Elastic Geodesic Grids and Their Planar-to-Spatial Deployment

Authors: Stefan Pillwein, Kurt Leimer, Michael Birsak and Przemyslaw Musialski

Published in: ACM Transactions on Graphics, Vol. 39, No. 4, July 2020

2.1 Introduction

Design and construction of structures composed of curved elastic elements has a long history in the field of architecture. Alongside their aesthetical aspects imposed by nature, they have a lot of functional advantages: they are compact, lightweight and easy to build; nonetheless practicable, durable, and of high structural performance.

They have been utilized for a long time dating back to ancient vernacular architecture for formal as well as for performance reasons, however, the possibilities of their form-finding in the past were limited [Lienhard et al. 2013].

Fortunately, the currently available computational capabilities and advances in computer science open up avenues for direct modeling of complex shapes composed of elastically bending members. This goes beyond traditional architectural design and allows to aim at many general purpose products composed of such elements. The range of potential objects encompasses gridshells, formwork, paneling, various types of furniture, sun and rain protectors, pavilions and similar small-scale buildings, home decoration and accessories, like vases, bowls, or lamps, etc., and finally, also elements of future's functional digital fabrics that can be utilized in engineering as well as in fashion.

This vision leads directly to the objective of this paper: a designer provides a target surface and a computational method finds a planar grid of flat lamellas, that—when deployed—approximates the surface well. Figure 2.1 shows a planar and a deployed grid of wooden strips, where a surface with the curved lamellas being tangential to it can be imagined. The joints between the lamellas allow for rotation and partially also for sliding. As the lamellas connecting opposite edges of the planar boundary quadrilateral are not parallel to each other, the grid is rigid in the plane. Given the flexibility of wooden lamellas with regard to bending and twisting, the grid is not rigid

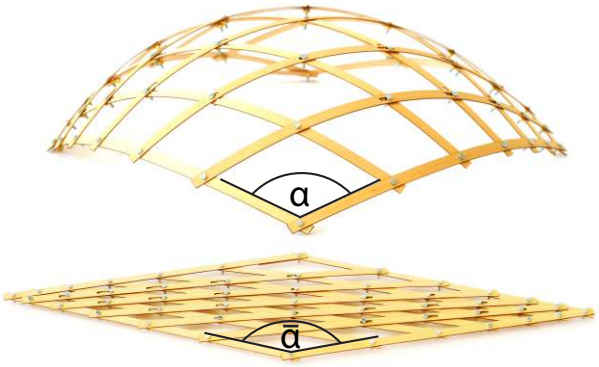

Fig. 2.1: A deployed elastic geodesic gridshell (top) and its planar lattice in the rest state (bottom) fabricated of wooden lamellas. The deployment of the whole kinematic system is based on changing angle $\bar{\alpha}$, such that $\bar{\alpha} \rightarrow \alpha$.

in space. By adjusting only one degree of freedom, for example the angle $\bar{\alpha} \rightarrow \alpha$ at one corner, the planar kinematic configuration *elastically bends* continuously into a spatial gridshell which approximates the desired surface. The deployment process is governed by the rules of physics, seeing the lamellas as thin elastic minimal energy beams, allowed to bend as well as to rotate and slide at their intersections.

Our goal is to find a suitable planar setup of the lamellas that can be deformed into a spatial grid, fitting the target surface as closely as possible. To achieve this goal, we propose a solution based on networks of geodesic curves on the target surface. We introduce a set of conditions and assumptions which can be met closely in practice and restrict the grids to geodesics. However, at the same time, it allows us to develop a purely geometric solution which builds on top of theoretical background from differential geometry.

An advantage of our approach is to omit numerical shape optimization and to provide a solution which allows for easy exploration of designs of geodesic curve networks. To produce large scale gridshells, further considerations will be needed, however, our main goal is geometric modeling and form-finding. Our work provides insights into that domain, also due to the fact that it uses intrinsic surface geometry only. In summary, the contributions of this paper are the following:

- We identify a specific case of the inverse design problem of spatial elastic grids which can be formulated using geometric considerations only. This formulation allows us to find a grid which is perfectly planar and can be isometrically deformed in an elasto-kinematic manner to a desired spatial grid.
- We derive a mathematical method for form-finding of such geodesic grids based on differential-geometric properties of geodesic curves. In particular, we introduce *distance maps* and *cladding functions* which allow for efficient finding of suitable configurations without expensive numerical shape optimization.
- Finally, we introduce physical simulation and a simple fabrication method for wooden small-scale elastic geodesic gridshells and perform empirical measurements which prove the validity of our approach.

In the following section we review related work and in Section 2.3 we provide a set of preliminary considerations necessary for our formulation. In Section 2.4 we provide the details of our geometric derivation, and in Section 2.5 we propose an adapted physical simulation. In Section 2.6 we present and evaluate our results. Finally, we discuss and conclude the work in Sections 2.7 and 2.8.

2.2 Related Work

Developable Surfaces This topic has a long tradition in computer graphics and architectural geometry [Pottmann et al. 2015]. A lot of attention has been paid to the approximation of free-form surfaces with developable strips [Wallner et al. 2010; Pottmann et al. 2010], which can be fabricated from 2d flat material-sheets by cutting. By bending and combining them, complex free-form surfaces can be erected. Also paneling of surfaces with planar tiles [Eigensatz et al. 2010] or with general planar polygons [D. Chen et al. 2013] have been proposed. Another way is the division of shapes into principal strips which bend automatically if combined [Takezawa et al. 2016]. On the theoretical side, a novel representation of developable surfaces using quadrilateral meshes with appropriate angle constraints [Rabinovich et al. 2018a] or a definition of developability for triangle meshes [Stein et al. 2018] have been proposed recently. Also discrete geodesic parallel coordinates for modeling of developable surfaces were proposed [H. Wang et al. 2019]. All these works aim at the design of developable surfaces, which, due to their isometric properties, can be fabricated from planar sheets. However, they do not incorporate a planar-to-spatial elastic deployment.

Deployable Surfaces One more way to easily construct spatial shapes from flat sheets is by appropriately folding paper [Mitani et al. 2004; Massarwi et al. 2007], which is inherently related to the Japanese art of Origami [Dudte et al. 2016]. Another set of works deals with curved folding and their efficient actuation from flat sheets to spatial objects [Kilian et al. 2008; Kilian et al. 2017a]. Our work is related to these approaches in terms of being deployable from a planar initial state, however, the main difference is that our grids are elastic and approximate doubly-curved surfaces.

In fact, a lot of attention has been paid to the design of doubly-curved surfaces which can be deployed from planar configurations due to the ease of fabrication. One way of achieving this goal is by using auxetic materials [Konaković et al. 2016] which can nestle to doubly-curved spatial objects, or in combination with appropriate actuation techniques, can be used to construct complex spatial objects [Konaković-Luković et al. 2018]. The main difference to our approach is that these structures do not use elastic bending to reach the actual spatial shape.

Elastically Deployable Surfaces An interesting way to deploy surfaces is to utilize the energy stored in planar configurations in order to approximate shapes, for instance using prestressed latex membranes in order to actuate precomputed planar geometric structures into free-form shapes [Guseinov et al. 2017], or to predefine flexible micro-structures which deform to desired shapes if set under tension [Malomo et al. 2018]. A combination of flexible rods and prestressed membranes lead to Kirchhoff-Plateau surfaces that allow easy planar fabrication and deployment [Pérez et al. 2017]. These methods achieve their planar-to-spatial configuration from elastic tension in the network, either due to prestressing in the planar state or by setting appropriate boundary conditions. The latter approach is more closely related to ours, however, instead of structure optimization, we build on top of the differential geometric properties of geodesic curves on the target surfaces. Thus, our method is based on the assumption that the elastic elements can bend and twist, but not stretch and must therefore maintain the same length in the planar as well as in the spatial configuration.

Wire Surfaces Our work also contributes to surface approximations using grids. This is not a novel approach, and previous works have tackled this topic. For example, approximations of surfaces with meshes based on Chebyshev nets [Garg et al. 2014], as well as with wires that are deformed in planar configurations and assembled together [Miguel et al. 2016] to abstract a spatial shape, have been proposed. In contrast to us, these works do not focus on elastic-planar-to-spatial deployment nor on elasticity of the networks.

Physical Surfaces. A number of methods which aim directly at computational design of physically valid and stable architectural structures have been proposed. For example, design of self-supporting masonry surfaces [Vouga et al. 2012] or the design of unreinforced masonry surfaces

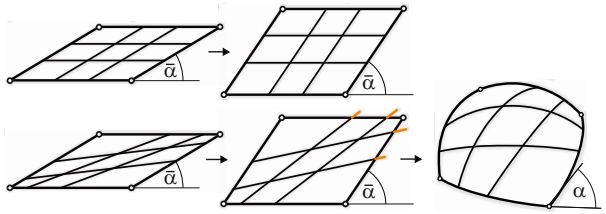

Fig. 2.2: The principle behind our planar to spatial deployment system. Top row: all members of a family are parallel and rigid, the kinematic linkage can move freely in the plane. Bottom row: non parallel layout produces a deadlock when trying to change the shape, inner members are too long. Allowing members to elastically deform, they buckle out of plane.

[Panozzo et al. 2013]. Also the process of erection of such objects has been computationally explored [Deuss et al. 2014]. Moreover, methods for fast interactive form-finding of physically stable structures [Tang et al. 2014], for the minimization of material usage under stability constraints [Kilian et al. 2017b], or physically plausible tensegrity structure design [Pietroni et al. 2017] have been proposed. Our method is related in terms of the goal of achieving structurally stable shapes. In turn, these methods do not utilize elastic bending for deployment or stability.

Classical Geometric Surfaces. In classic differential geometry, geodesic nets on surfaces which can be mapped onto a geodesic net on a different surface (including a plane) have been analyzed by Voss [Voss 1907] and Lagally [Lagally 1910]. Regarding to their analysis, arc-length preserving mappings of continuous geodesic nets onto each other require rhombic geodesic nets, i.e., need a parametrization of the surface with the net curves as parameter curves and $E = G$ in the fundamental form. The resulting Liouville surfaces are very limited in shapes, and therefore not useful for our free-form design purpose.

Gridshells and Active-Bending The idea of gridshells — structures that gain their strength and stiffness through their curvature—were introduced by Shukhov for the Rotunda of the Panrussian Exposition [Shukhov 1896] and further pursued by famous architects, e.g., by Frei Otto for the construction of the roof of the Multihalle at the Mannheim Bundesgartenschau [Happold et al. 1975].

The introduction of the *active bending* paradigm [Lienhard et al. 2013] together with enhanced and easy-to-use computational methods increased the interest of the scientific community in systematically utilizing elastic bending to realize curved shapes. Until recent advances in computer science they could only be form-found empirically [Gengnagel et al. 2013].

Existing design approaches are often based on particular kinds of surface curves, e.g., curvature lines [Schling et al. 2018]. Emerging concepts for the erection of elastic gridshells facilitate the construction process or even eliminate the need for scaffolding [Quinn et al. 2014].

Architectural works which aim at the approximation of gridshells and combine lightweight structural design with aesthetics [Soriano 2017] also inspired our work. Soriano et al. [Soriano et al. 2019] also proposed mechanisms for the deployment of geodesic gridshells using an evolutionary solver to form-find the grids. However, the design process is rather complex and time consuming, using numerical gradient-free optimization methods. In contrast, our approach is based on geometric considerations and omits expensive computations. Besides gridshells, kinetic structures, bending plate structures, and textile hybrids form a new class of structures explored in the active bending research community [Lienhard et al. 2018].

Recently [Panetta et al. 2019] introduced an interactive approach for finding deployable grid structures. Their method requires the user to create an initial grid design by iterating between layout editing and grid simulation steps. Once an overall satisfying shape is found, the layout is then optimized to reduce the internal elastic energy of the flat assembly state and the deployed target state.

In contrast, our design approach only requires the user to provide a target surface patch. Based on its geometry, our algorithm produces a grid layout to approximate the target surface patch when deployed. Furthermore, our approach guarantees that the planar configuration is in a zero-energy state.

Fabrication and Elastic Simulation The computer graphics community started to deal with fabrication and computational design [Bermano et al. 2017], for this reason many novel methods aim at fast but physically valid simulations. Our simulation is based on the method of discrete elastic rods [Bergou et al. 2008; Bergou et al. 2010], which have been adapted and utilized for works on sparse rod networks [Pérez et al. 2015; Malomo et al. 2018; Vekhter et al. 2019]. Recently this method has been also used for the simulation of hemispherical elastic gridshells [Baek et al. 2019].

2.3 Preliminary Considerations

2.3.1 Elasto-Kinematic Deployment

The main idea behind our planar-to-spatial deployment is based on a very simple kinematic mechanism, as depicted in Figure 2.2. It is a special case of a planar quadrilateral four-bar linkage with rigid members, rotating joints and one degree of freedom.

If we change the angle at one corner and all links of a family are parallel, the system can move freely in the plane (Figure 2.2, top row). If we introduce stiff inner links which are not parallel, the system is deadlocked. By introducing bending and twisting flexibility to the members, they buckle out of plane in order to preserve their length and form a spatial grid (Figure 2.2, bottom row). To construct such a mechanism, the lengths of the members

must match on the surface as well as in the planar configuration. Mathematically, this behavior can be modeled by geodesic curves on a surface.

A geodesic locally minimizes the arc length between two distinct points and maintains its length under isometric deformations of the surface. Moreover, its principal normal falls into the surface normal, i.e., it allows normal curvature, but prohibits geodesic curvature. As a consequence, a carefully chosen network of such curves can be used to build the elasto-kinematic deployment mechanism and to abstract the surface' characteristics.

Additionally, gridshells of the nets should be easy to manufacture, transport, assemble, and deploy. To meet these properties in practice, we use thin straight lamellas with a cross section ratio of about 1 : 10, creating a distinct weak axis for easy bending and a strong axis that prohibits bending. These lamellas can be wrapped on a surface and interpreted as tangential strips with a geodesic centerline. Also their connections, which are essential for the kinematic deployment, imitate the intersections of geodesics well: the lamellas can rotate with the axis of rotation being always parallel to both of the principal normals of the centerlines, and their connections can slide along the tangents of the centerlines.

Besides apparent advantages of easy production, geodesics offer a lot of theory and give us a great set of tools to analyze surface patches and find suitable solutions.

2.3.2 Grid Representation

The input to our computational system is a surface patch $\mathcal{P}$ which is a convex bounding shape defined on a designer created target surface by four corners. They are connected by geodesic curves on the surface which constitute the boundaries of the surface patch $\mathcal{P}$ as depicted in Figure 2.3. The output of our system is a planar quadrilateral, denoted as planar patch $\bar{\mathcal{P}}$, filled with interconnected straight lines. Its corners are the counterparts of the spatial corners.

The patches consist of two families of grid members: g, h-members are geodesics on the surface patch, and $\bar{g}, \bar{h}$-members are their corresponding straight lines in the planar patch with matching lengths (cf. Figure 2.3). The grid members are parameterized along the boundaries with parameter-pairs (u_1, u_2) and (v_1, v_2) respectively.

2.3.3 Surface Patch Characteristics

Using geodesics to model the grid members also poses restrictions on the representability of the target surfaces. There are two ways to compute geodesics: defining a start point and a direction vector, which has a unique solution, or defining a start and an end point, which delivers the shortest path between these two points, but does not necessarily have a unique solution [Polthier et al. 1998].

To maintain the length of a curve between the boundaries, we need to compute geodesics between two points

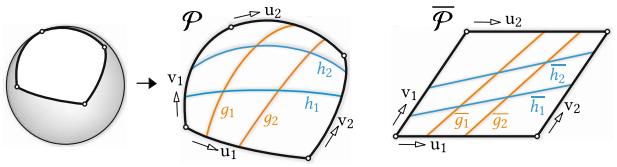

Fig. 2.3: Overview of our approach and the notation. Left: the user selects four corners on a desired target surface. Center: the surface patch $\mathcal{P}$ with members of the g and h family. Each family is parameterized with pairs (u_1, u_2) and (v_1, v_2) respectively. Right: a corresponding planar patch $\bar{\mathcal{P}}$ with corresponding members of the $\bar{g}$ and $\bar{h}$ family (cf. Section 2.3.2).

on opposite boundaries, so for our application we use the second case, which we will denote as shortest geodesics from now on.

A feature of shortest geodesics—namely the possibility of non unique solutions—can have disadvantageous effects for the approximation. It may happen that two points on a surface patch can be connected by more than one shortest geodesic. The existence of such points is linked to the Gaussian curvature K of the surface. They result in areas of the patch $\mathcal{P}$ that cannot be covered with shortest geodesics connecting the boundaries. For the quality of the approximation, it needs to be ensured that every point on patch $\mathcal{P}$ can be reached by a shortest geodesic of the g and h-curves family. If this is not the case, surface features cannot be captured with shortest geodesics and cannot be encoded in the planar grid.

Figure 2.4 illustrates the problem: when drawing shortest geodesics from point p to all points on the opposite boundary, the central area of high positive K remains uncovered and produces a gap in the coverage. Taking a look at the distance field (Figure 2.4, left), we can identify singularities as it approaches the opposite boundary. These singularities form the *cut locus* $\mathcal{L}(p)$ on $\mathcal{P}$ and each point $\in \mathcal{L}(p)$ can be reached from p by two distinct geodesics of the same length.

The geodesic distance d between p and its nearest point on $\mathcal{L}(p)$ is called the *injectivity radius* $ir(p)$ [do Carmo 1992] given as

$$ir(p) = \inf d(p, \mathcal{L}(p)) .$$

Using a corollary of the Rauch comparison theorem [do Carmo 1992] we obtain the following inequality:

$$ir(p) \geq \frac{\pi}{\sqrt{K_{\max}}} . \tag{2.1}$$

It gives us a lower bound for the injectivity radius $ir(p)$ for each surface point p. Evaluating it at local peaks of Gaussian curvature $K_{\max}$ serves as a quick check for the uniqueness of shortest geodesics.

If the lengths of all members are smaller than the right hand side of Expression (2.1), the patch can be used as it is.

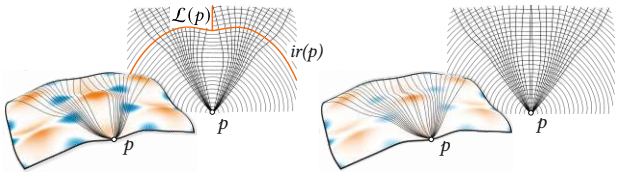

Fig. 2.4: Shortest geodesics between point p and points on the opposite boundary (top) and distance fields emanating from p (bottom). Left: the peak area cannot be covered by shortest geodesics, cut locus $\mathcal{L}(p)$ and injectivity radius $ir(p)$ are indicated. Right: Uncovered area sufficiently reduced by smoothing (cf. Section 2.3.3).

If this is not the case, the surface patch cannot be covered completely (unless the peak is on the boundary).

Although Expression (2.1) indicates the existence of these areas, the size of the gaps remains unclear. Small gaps may not pose big problems for the quality of the approximation, while big gaps do. They indicate that there is a considerable difference in length between the shortest geodesic next to the peak and the (start-direction) geodesic over the peak, thus the quality of the approximation of the surface by the planar grid will be worse. In order to handle surface patches that cannot be covered with shortest geodesics completely, we propose an iterative smoothing procedure.

To check for uncoverable areas around a Gaussian curvature peak $p_{\max}$, we first compute two distance fields: one from the peak $p_{\max}$ and one from the boundary point p_1, where we choose p_1 to be the closest point to $p_{\max}$ on the boundary.

They provide us with distances $d(p_1, q)$ to the points q of the opposite boundary as well as $d(p_1, p_{\max})$ and $d(p_{\max}, q)$. We compute the minimum of $d(p_1, p_{\max}) + d(p_{\max}, q) - d(p_1, q)$, which is reached at a point q_1. If the minimum is close to zero, the peak $p_{\max}$ is not problematic and there is no gap. If not, the factor:

$$\eta = \frac{d(p_1, p_{\max}) + d(p_{\max}, q_1)}{d(p_1, q_1)}$$

is used to measure the size of the gap. In order to remove the unreachable gaps, we perform Laplacian smoothing of $\mathcal{P}$ with cotangent weights iteratively [Desbrun et al. 1999], until η falls below a certain threshold $\eta_{\max}$. In practice we choose $\eta_{\max} = 1.0015$ (cf. Figure 2.4, right) which we have determined empirically.

2.4 Elastic Geodesic Grids

2.4.1 Grid Criteria

Our goal is to find a grid of geodesics on $\mathcal{P}$, which can be "planarized" to $\bar{\mathcal{P}}$ with a certain angle $\bar{\alpha}$. The grid curves are allowed to reduce their curvature and torsion but should keep their total lengths as well as the lengths between points of intersection. At each configuration, the grid curves should be geodesics on a hypothetical surface.

Inversely, the planar grid is deployed to a spatial grid as the planar angle approaches the spatial angle, i.e., $\bar{\alpha} \to \alpha$ such that the planar corners approach their spatial counterparts, and the planar straight lines bend to geodesic curves tangential to the target surface.

In order the meet these requirements, both the planar and the spatial grids need to obey the following geometric demands:

(i) *Length correspondence*: All straight lines $\bar{g}, \bar{h}$ have the same lengths as their corresponding geodesics g, h.

(ii) *Boundary correspondence*: On boundaries, the (u_1, u_2) and (v_1, v_2) coordinates of connections are identical for the 2d and the 3d grid.

(iii) *Bijectivity of correspondence*: Each point on one boundary has one and only one corresponding point on the opposite boundary, defining a grid member uniquely.

(iv) *Convexity of boundary*: the corresponding patches $\mathcal{P}$ and $\bar{\mathcal{P}}$ need to be convex.

Criterion (iv) is necessary, since otherwise the kinematic mechanism can run into a deadlock. It is fulfilled if each of the four inner angles of $\mathcal{P}$ is less than π, which can be argued with the triangle inequality of the surface metric and the convexity of sufficiently small areas [do Carmo 1992].

In the following, we introduce mathematical tools which allow to identify geodesic grids which fulfill all posed criteria. We explain the process only for one family of members. Note however that the shape of the planar patch is chosen with respect to both families, satisfying interconnecting constraints, thus they are not found independently.

2.4.2 Distance Maps

As a tool to match the distances on the surface patch $\mathcal{P}$ and the planar patch $\bar{\mathcal{P}}$, we introduce distance maps $\mathcal{D}_u$ and $\mathcal{D}_v$. To create them, distance fields are spread from all points $p(u_1)$ on one boundary to all points $q(u_2)$ on the opposite boundary, measuring the geodesic distances $d(p(u_1), q(u_2))$ between them (cf Figure 2.5, left). Transforming the distances into the (u_1, u_2, d)-3d space creates a representation of the geodesic lengths of the surface patch, which is illustrated in Figure 2.5. While the distance maps of the surface patch $\mathcal{D}_u(u_1, u_2)$ and $\mathcal{D}_v(v_1, v_2)$ have a predefined angle α induced by the choice of the surface patch and depend only on the coordinates u_1, u_2 and v_1, v_2 respectively, the distance maps of the planar patch $\bar{\mathcal{D}}_u(u_1, u_2, \bar{\alpha})$ and $\bar{\mathcal{D}}_v(v_1, v_2, \bar{\alpha})$ also depend on the angle $\bar{\alpha}$. The choice of that angle changes the shape of the planar grid and hence also the shapes of the distance maps $\bar{\mathcal{D}}_u$ and $\bar{\mathcal{D}}_v$. In our implementation, distance maps

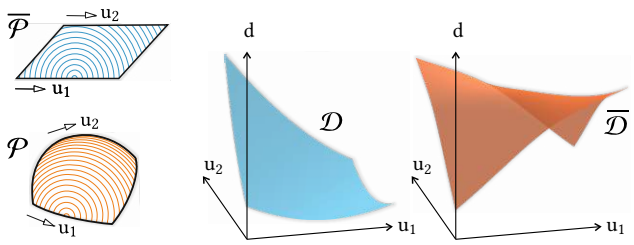

Fig. 2.5: Distance fields on a planar patch $\bar{\mathcal{P}}$ and a surface patch $\mathcal{P}$, computed from a single point shown on the left. By sampling all point-pairs along corresponding (u_1, u_2)-domains, we create distance maps $\mathcal{D}_u(u_1, u_2)$ and $\bar{\mathcal{D}}_u(u_1, u_2, \bar{\alpha})$. Note that the planar distance map $\bar{\mathcal{D}}$ also depends on the shape of $\bar{\mathcal{P}}$ and thus the angle $\bar{\alpha}$ (cf. Section 2.4.2).

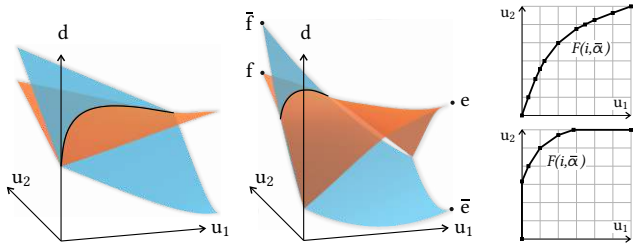

Fig. 2.6: Intersection of distance map $\bar{\mathcal{D}}_u(u_1, u_2, \bar{\alpha})$ for planar patch in blue and distance map $\mathcal{D}_u(u_1, u_2)$ for surface patch in orange. Left: proper intersection, fulfilling the constraints (cf. Sec. 2.4.3). Center: partial intersection, providing an invalid cladding function $\mathcal{F}_u$. Right: piecewise linear functions F_u of both cases evaluated on a discrete grid (cf. Section 2.4.3).

are represented as quad meshes; their resolution is chosen according to the resolution of the input surface mesh. In practice, it is around 100×100 vertices.

2.4.3 Cladding Functions

In this section we derive the cladding functions which determine the distribution of the corresponding members in $\bar{\mathcal{P}}$ and $\mathcal{P}$. This is done via finding a suitable angle $\bar{\alpha}$, such that the grid criteria defined in Section 2.4.1 are fulfilled.

The cladding function $\mathcal{F}_u$ is built by first projecting the intersection of the distance maps $\mathcal{D}_u$ and $\bar{\mathcal{D}}_u$ to the u_1, u_2-plane (respectively, $\mathcal{F}_v$ is built using a projection to the v_1, v_2-plane). Points on this function represent geodesics which connect opposite boundaries and have the same length on both the planar and the spatial patch. Please recall that the shape of the distance map $\bar{\mathcal{D}}_u(u_1, u_2, \bar{\alpha})$ also depends on the choice of the angle $\bar{\alpha}$, hence the shape of the cladding function does as well.

Grid criteria (i) and (ii) are fulfilled by the nature of these functions. Our goal is now to determine the parameter $\bar{\alpha}$ such that also grid criteria (iii) and (iv) are fulfilled. This implies that the cladding function $\mathcal{F}_u$ must be continuous and bijective over the entire domain, which means its first order partial derivative $\dot{\mathcal{F}}_u$ w.r.t. u_1 should nowhere reach 0 nor ∞ (cf. Figure 2.6, right).

Additionally, bounds can be set on $\dot{\mathcal{F}}_u$ in order to avoid too steep or too flat tangents, which would result in a strong concentration of members on a boundary and an uneven coverage of the patches $\bar{\mathcal{P}}$ and $\mathcal{P}$ as shown in Figure 2.7. Moreover, if criteria (iii) and (iv) are not fulfilled, triangular member connections may appear in the planar grid, destroying the kinematic deployment mechanism.

With this picture in mind, we denote the cladding functions as

$$u_2 = \mathcal{F}_u(u_1, \bar{\alpha}) \quad \text{and} \quad v_2 = \mathcal{F}_v(v_1, \bar{\alpha})$$

with $u_1, u_2 \in [0, 1]$ (v_1, v_2 respectively). Refer to Figure 2.7 for a depiction. Please note that for the cladding functions to exist, the length of the diagonals e, f of the surface patch $\mathcal{P}$ and $\bar{e}, \bar{f}$ (cf. Figure 2.6) of the planar patch $\bar{\mathcal{P}}$ must fulfill the following inequality:

$$(e - \bar{e}) \cdot (f - \bar{f}) < 0\,. \tag{2.2}$$

In other words, this inequality is a necessary condition for a proper intersection of the distance maps. Figure 2.6 depicts how the diagonals e, f of the surface patch and $\bar{e}, \bar{f}$ of the planar patch appear in the distance maps.

To find a feasible domain for the angle $\bar{\alpha}$ under the condition of bijective cladding functions $\mathcal{F}_u(u_1, \bar{\alpha})$ and $\mathcal{F}_v(v_1, \bar{\alpha})$, we formulate it as an optimization problem using Expression (2.2) as a constraint.

Note that at $(0, 0)$ and $(1, 1)$ distance maps always intersect, so $\mathcal{F}_u$ is always defined there. However, the function might be not defined or not continuous over the entire domain of $u_1 \in [0, 1]$, as depicted in Figure 2.6, center. To deal with this case, we introduce a piecewise linear parametric representation $F_u(i, \bar{\alpha}) = (u_1(i), u_2(i), \bar{\alpha})$ given over the entire domain and range of $\mathcal{F}_u$ (cf. Figure 2.6).

Using the slopes of the segments $\dot{F}_u$ and $\dot{F}_v$ simultaneously as constraints, we cast the following optimization problem to determine a feasible domain for the angle:

$$\begin{aligned} \min \quad & \bar{\alpha} \\ \text{s.t.} \quad & (e - \bar{e}) \cdot (f - \bar{f}) < 0 \\ & k_{\min} < \dot{F}_u(i, \bar{\alpha}) < k_{\max}, \quad 1 \ldots n \\ & k_{\min} < \dot{F}_v(i, \bar{\alpha}) < k_{\max}, \quad 1 \ldots n, \end{aligned} \tag{2.3}$$

with n being the number of segments and with $k_{\min}$ and $k_{\max}$ being slope bounds which we have determined empirically as $k_{\min} = 0.1$ and $k_{\max} = 10$. We evaluate $\dot{F}_u$, $\dot{F}_v$ using finite differencing

$$\dot{F}_u(i, \bar{\alpha}) = \frac{\Delta u_2(i)}{\Delta u_1(i)}$$

at all segments, as shown in Figure 2.6, right. To tackle the case where $\dot{F}_u = \infty$, we set its value to $c\Delta u_2$ with $c \gg k_{\max}$; cases with $\dot{F}_u = 0$ do not cause any numerical problems. In our implementation, each cladding function is computed by intersecting the distance map meshes and

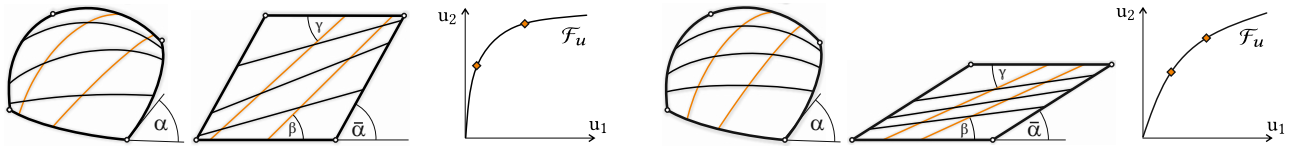

Fig. 2.7: The influence of $\bar{\alpha}$ on the cladding with grid members: its choice affects the distribution and coverage of the members g and h on the surface patch $\mathcal{P}$. Right: the shape of the cladding function $\mathcal{F}_u$ with indicated members (cf. Section 2.4.3). Please note also the angles β and γ, which are used to determine minimum distances between lamellas with a certain width (cf. Section 2.4.4).

their resolution induces the resolution of piecewise linear function F.

We solve Problem (2.3) using sequential quadratic programming with numerical gradients w.r.t. $\bar{\alpha}$. First we determine the minimum feasible $\bar{\alpha}_{\min}$ with the lower bound for $\bar{\alpha}$ from the convexity restrictions of grid criterion (iv). Then we find a maximum feasible $\bar{\alpha}_{\max}$ using the same concept. Values of $\bar{\alpha}$ between these bounds ensure the cladding functions $\mathcal{F}_u$ and $\mathcal{F}_v$ to be bijective.

Note, that setting bounds for $\bar{\alpha}$ also makes it possible to introduce designer constraints on the shape of the planar patch $\bar{\mathcal{P}}$. In practice, we choose $\bar{\alpha}_{\min}$ for our examples, which results in a compact planar patch design.

2.4.4 Grid Members

After checking the validity of the surface patch (with smoothing, if needed) and fixing $\bar{\alpha}$, we choose the number and positions of the grid members. Patches with many curvature features (cf. Figure 2.4) obviously need a minimum number of well placed members to capture all surface features well. For this specific example, all the bumps of the surface have to be encoded in the planar grid.

Our approach for fitting grid members is a geometrically motivated heuristic. It reuses the information from the intersections of the respective distance maps $\mathcal{D}_u$ and $\bar{\mathcal{D}}_u$ in the (u_1, u_2, d) space (cf. Section 2.4.3). Along their intersection curve, we can construct an associated function $C_u(s)$ of geodesic lengths d of the members. Its maxima and minima correspond to longest or shortest geodesics $(g_i, \bar{g}_i)$ on the surface patch $\mathcal{P}$ and provide good candidates for physical members of the elastic grid.

Hence, members are first placed at the extrema of $C_u(s)$ and next at the extrema of the curvature of $C_u(s)$. The first pass ensures to cover major features (large peaks) since these members correspond to locally longest and shortest geodesics. The second pass ensures to capture finer features (smaller bumps), since the corresponding members are also locally the longest or the shortest members, however on a smaller scale. Figure 2.8 depicts these steps.

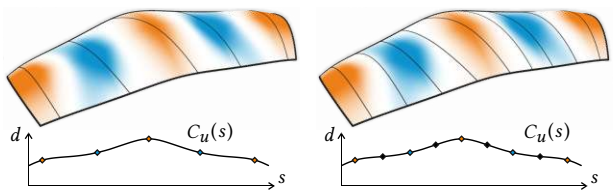

Fig. 2.8: One iteration of the member placement procedure. Left: members placed based on geometric features. Right: additional members placed in the gaps and distributed without affecting the initial members. Bottom row depicts the C-function with indicated members (cf. Section 2.4.4).

In order to avoid the members to be placed too close to each other or to overlap, we compute the offsets

$$d^{(+)}\left(\beta(u_1), \gamma(u_1), w_m\right) \quad \text{and} \quad d^{(-)}\left(\beta(u_1), \gamma(u_1), w_m\right)$$

which give the minimum distance between a member and its preceding and subsequent neighbors. The angles $\beta(u_1)$ and $\gamma(u_1)$ are the enclosed angles between a member and the boundaries, and w_m is the member width (cf. Figure 2.7). If members are too dense, we prioritize them using the absolute value of curvature of $C_u(s)$. The assumption behind this choice is inspired by the observation that the more curved C_u locally is, the more distinct surface features the corresponding geodesic captures.

If members are too sparse, we add new members in the gaps, which fulfill the restrictions imposed by $d^{(+)}$ and $d^{(-)}$. After adding them, we minimize the sum of the squared distances to existing members in order to achieve a more equal distribution.

Note that the same procedure is applied to $\mathcal{D}_v$ and $\bar{\mathcal{D}}_v$ to obtain the function C_v and the members of the $(h, \bar{h})$ family.

2.4.5 Notches

Deploying the planar grid with rotational-only connections delivers an approximation of the surface patch $\mathcal{P}$, but the centerlines of the physical lamellas cannot become geodesics on $\mathcal{P}$. The reason is that they are held back by their fixed intersections with inner members of the other family. This restriction is a consequence of the grid criteria (i) and (ii). Note that as shown by Lagally [Lagally 1910], an arbitrary geodesic grid cannot be planarized in general.

To address this issue, we introduce *sliding notches* at the connections of inner members. These notches provide two translational degrees of freedom at each connection, enabling the respective members g_i and h_j to slide by the notch lengths ℓ_{g_i}, ℓ_{h_j} (cf. Figure 2.9). We can identify unique optimal sliding directions and notch lengths from comparing the difference of the locations of the connec-

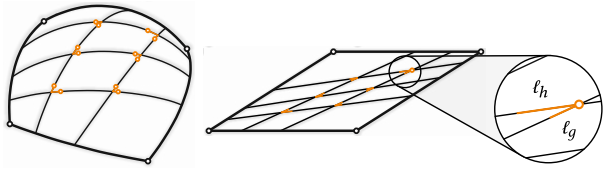

Fig. 2.9: Left: deployment without notches, where orange dots indicate optimal connections in the spatial state. Right: Notches ℓ_g, ℓ_h computed for one particular connection q (cf. Section 2.4.5).

tions w.r.t. the arc length between the geodesic members g, h and their planar counterparts $\bar{g}, \bar{h}$.

In other words, traversing an inner member pair $(g_i(s), \bar{g}_i(\bar{s})) \in (g, \bar{g})$ along its arc length parameters s and $\bar{s}$, the notch length ℓ_{g_i} at a particular connection is given by

$$\ell_{g_i} = s - \bar{s}\,.$$

The notch length ℓ_{h_i} along the $(h_i(s), \bar{h}_i(\bar{s}))$ member pair is given in an analogous way (cf. Figure 2.9).

The corresponding sliding directions are given by the sign of this equation. If each connection slides to the end of both its notches, the centerlines of the lamellas move towards the geodesics on $\mathcal{P}$. Due to the extra degrees of freedom, notches enable the structure to take a lower energy state by reducing the torsion and curvature of the members. The notches are physically realized by simply elongating the holes of the corresponding lamellas.

2.4.6 Anchors

When changing the angle $\bar{\alpha} \to \alpha$, an elastic grid buckles out of plane into a curved configuration. While the surface patch $\mathcal{P}$ has a fixed shape, the grid can deform to multiple spatial configurations, since an elastic grid for a specific surface patch is also suitable for all isometric surface patches. This is given by the fact that our grids are constructed using the intrinsic metric on $\mathcal{P}$, which is invariant to isometries. Isometries of a surface can be imagined by bending the surface without stretching it.

To force the grid into the desired configuration, we introduce additional anchors which pin connections of members to fixed points on the target surface. We systematically introduce them on selected connections of inner members with boundary curves, such that they push the elastic grid into a configuration in agreement with the shape of $\mathcal{P}$.

For practical reasons, we only allow anchors on the boundaries. In particular, we identify points of locally extreme curvature on the boundary geodesics and filter for small extrema. The connections of members closest to these points serve as anchor locations (cf. Fig. 2.10).

Fig. 2.10: The influence of anchors and notches on the example *Archway*. Left: Anchors at the corners are not sufficient to push the grid into the right configuration. Center: Deployed state without notches, local buckling and irregularities in smoothness can be observed. Right: Notches relax the structure to a more natural, lower energy shape (cf. Sections 2.4.5 and 2.4.6).

2.5 Physical Simulation

To simulate the physical behavior of the deployed grid, we use a simulation based on discrete elastic rods [Bergou et al. 2010] and build upon the solution of [Vekhter et al. 2019]. We refer the reader to those papers for the details. Note, that the associated material frames of the rods do not need to be isotropic, which allows us also to model the exact cross sections of lamellas with a ratio of 1 : 10.

A central aspect of the kinematics of elastic geodesic grids is the ability of grid members to slide at connections, denoted in the following as q. In general, they do not coincide with the vertices of the discretized grid members. To handle them, we introduce barycentric coordinates β_q to describe the location of a connection on a rod-edge. We also take the physical thickness t of the lamellas into account, which is modeled by an offset between the members g and h at each connection. Hence, a connection q consists of two points q_g and q_h with an offset t. Apart from sliding, members are allowed to rotate around connections about an axis that is parallel to the cross product of the edges q_g and q_h lie on.

Simulation Our aim is to find the equilibrium state of the given elastic grid, which corresponds to an optimization problem of minimizing the energy functional

$$E = E_r + E_q + E_a + E_n + E_p,$$

where E_r is the internal energy of the rods, E_q is the energy of the connection constraints, E_a is the energy of the anchor constraints, E_n is the energy of the notch-limit constraints, and E_p is an additional notch penalty term that also serves to account for friction. We perform the simulation by minimizing the entire energy E for the rod centerline points x using a Gauss-Newton method in a similar fashion as proposed by Vekhter *et al.* [Vekhter et al. 2019]. In Section 2.6.2 we perform an empirical evaluation of the accuracy of the simulation by comparing it to laser-scans of the makes.

For the sake of readability, we will define the constraint energy terms only for a single constraint each. E_r is the sum of stretching, bending and twisting energies of each

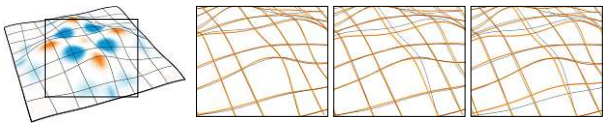

Fig. 2.11: The effect of the weighting parameter μ in E_p (from left to right): surface shaded with K and geodesics; $\mu = 0.01$, rods slide onto geodesics; $\mu = 0.1$, sliding in high K areas reduced (our setting); $\mu = 1$, sliding is heavily reduced. Refer to Section 2.7.3 for a further discussion on μ.

individual rod. As a full explanation of the DER formulation is out of scope for this paper, we refer the reader to the work of [Bergou et al. 2010] for a detailed description of these terms.

The connection constraint energy E_q is given by

$$E_q = \lambda_{q,1} \left\| q_g - q_h + t m_g \right\|^2 + \lambda_{q,1} \left\| q_h - q_g - t m_h \right\|^2 + \lambda_{q,2} \left\| \angle \left(m_g, m_h \right) \right\|^2,$$

with m_g and m_h denoting the material vectors of g and h at q respectively. The term tm accounts for the thickness of the rods, while $\lambda_{q,1}$ and $\lambda_{q,2}$ are the constraint weights for the position and direction terms.

The anchor constraint energy E_a ensures that both the position q and material vector m of the given connection do not deviate from the position q_a and material vector m_a of the corresponding anchor. It is given by

$$E_a = \lambda_{a,1} \left\| q - q_a \right\|^2 + \lambda_{a,2} \left\| \angle \left(m, m_a \right) \right\|^2,$$

with $\lambda_{a,1}$ and $\lambda_{a,2}$ as weights. This constraint applies to the grid corners and anchors.

The notch-limit constraint energy E_n ensures that the connection point remains within the bounds of the notch. They are specified by the notch length l and the sliding direction (cf. Section 2.4.5):

$$E_n = \delta^{(-)} \left(\frac{1}{10} \log \left(\beta_q - \beta^{(-)} \right) \right)^2 + \delta^{(+)} \left(\frac{1}{10} \log \left(\beta^{(+)} - \beta_q \right) \right)^2$$

with $\beta^{(-)}$ and $\beta^{(+)}$ denoting the barycentric coordinates of the notch bounds on their corresponding edges. The term is only active when the connection lies on the same rod-edge as one of the notch bounds, so $\delta^{(-)} = 1$ or $\delta^{(+)} = 1$ when the connection lies on one of these edges, and 0 otherwise.

The additional notch penalty term E_p controls the movement of a connection q between two adjacent edges. If q switches edges, it needs to be reprojected to the neighboring edge at the next iteration of the simulation. Within an iteration, E_p prevents q from moving too far beyond the end of the current edge:

$$E_p = \left(\mu \log \left(\epsilon + \beta_q \right) \right)^2 + \left(\mu \log \left(\epsilon + 1 - \beta_q \right) \right)^2,$$

with ϵ denoting how far q is allowed to move past the end of the edge and μ acting as a weighting parameter (we choose $\epsilon = 0.0001$, $\mu = 0.1$).

Since E_p is not 0 even inside the edge, it penalizes very small sliding movements that would otherwise accumulate over many iterations. In other words, E_p creates a pseudo-frictional effect, which is controlled by μ. In a physical grid, friction creates a force acting against the sliding movement of a connection. If the driving force of the movement and the frictional force counterbalance, the movement stops. This situation has an analogy in our grids. A connection stops moving inside a notch if

$$\frac{\partial E_q}{\partial \beta_q} + \frac{\partial E_p}{\partial \beta_q} = 0$$

is fulfilled. Figure 2.11 depicts the effects of different values for μ.

2.6 Results and Evaluation

2.6.1 Qualitative Results and Fabrication

Using our method, we have approximated a number of surfaces which are depicted in Figures 2.12 and 2.14. We used input surfaces with positive and negative Gaussian curvature regions, as well as purely elliptic and hyperbolic surfaces.

The fabricated models we present in Figure 2.14 are made of lime wood lamellas and placed on 3d-printed supports after assembly. To position the notches precisely, lamellas are laser-cut from thin lime wood plates. Members are connected by simply using screws and nuts. The support structures fix the shape of the boundary members to anchors as described in Section 2.4.6 and also provide correct orientation for the lamellas by inclined contact areas.

2.6.2 Evaluation

Quantitative Results In Table 2.1 we summarize quantitative results of our method for seven models (Figure 2.12 and 2.14). The presented values RMS_1 and RMS_2 denote the root mean square distance between grid vertices and the mesh representing $\mathcal{P}$ without and with notches respectively. As can be seen, notches allow for closer proximity between the rods and $\mathcal{P}$. Please note that the model width, depth and height listed in Table 2.1 are dimensionless and that we scale the model by a global factor for fabrication.

The computation time for the geometric grid generation (c.f. Section 2.4) mainly depends on the mesh resolution of $\mathcal{P}$, which also determines the number of distance fields that are computed. Smoothing additionally requires the computation of several distance fields in every iteration. Simulation time of the deployed state of the grid with and without notches mainly depends on the number of grid vertices.

Fig. 2.12: Computed and simulated results without make, renderings of the simulation and the planar grid. The orange lines follow our simulation with notches. The dark lines follow the shortest geodesics on $\mathcal{P}$.

Evaluation of Simulation To evaluate the agreement of the simulated results with the fabricated wooden makes, we used a state-of-the-art laser-scanning device (Metris MCA 36M7) to capture the deployed gridshell. To enable precise agreement of the cartesian anchor coordinates q_a and the point cloud, we registered them using the ICP algorithm.

The material properties of the wood were not determined by testing, but estimated using reference values for deciduous woods. Figure 2.13 shows the results of the comparison. Note that the root mean square error between the point cloud and the simulated model is 0.06 cm, which is only about half the thickness of a lamella.

2.6.3 Implementation

Our grid design algorithm is implemented in MATLAB, utilizing its sequential quadratic programming solver for solving the optimization Problem (2.3) using numerical gradients w.r.t. α. We furthermore implemented the DER-simulation in C++, building upon the framework of [Vekhter et al. 2019]. To compute the distance fields on the surface patch $\mathcal{P}$ we use the VTP algorithm by [Qin et al. 2016]. For the computation of the geodesic paths we use the algorithm for exact geodesics between two points by [Surazhsky et al. 2005].

2.7 Discussion

2.7.1 Geodesic Grids vs General Grids

In order to design general grids, the paths of the surface curves need to be flexible. In our method, we focus on geodesic curves due to their properties, in particular allowing only the normal curvature on surfaces (cf. Section 2.3). The directions of the curves on the surface can only be controlled by changing the angle $\bar{\alpha}$ because of the restrictions induced by the cladding functions. Creating an elastic geodesic grid that approximates an arbitrary curve network is therefore not possible.

As a consequence of our design choice, cross sections of fabricated members need to be rectangular with a high width to thickness ratio. While this ensures easy fabrication, at the same time it poses a limitation on the design space. As shown by Panetta et al. [Panetta et al. 2019], the shape-space of similar grid structures can be controlled by changing the profile of cross sections. However, when using more complicated cross sections, parts of them may buckle during deployment. This causes nonlinearities in stiffness parameters requiring to account for buckled cross sections. We avoid this necessary nontrivial update of the stiffness parameters, as the choice of our cross section minimizes these geometric second order effects.

Note that in our models, the size of the cross sections is uniform. Allowing different dimensions for every rod or even every segment would allow for an even better approximation of the surface patch.

2.7.2 Representable Shapes

Elastic geodesic grids can only approximate surfaces, that are "claddable" by unique shortest geodesics. If this is not the case, our smoothing algorithm ensures cladding, but surface details could be lost. Also the number and the density of members influences the representable shapes. If the shape is of very high frequency geometric details, it might not be representable by a too sparse network of physical members. In turn, in order to ensure fabricability, only a limited number of members is possible. This relationship is an interesting issue for future work.

To approximate the extrinsic shape of $\mathcal{P}$, we introduce anchors on the boundaries of an elastic grid. They act as constraints on the shape of the grid and are supposed to reduce the number of possible configurations to a single one. However, in some cases our definition of anchors is not sufficient. Imagine a high-frequency surface: fixed boundaries may not suffice to uniquely determine the direction of inner bumps. Although we did not encounter this problem in our examples, there certainly exist surface patches that require additional anchors inside the grid to pin down its shape uniquely.

Besides this geometric view on multiple deployed configurations, they can also be looked at from an equilibrium point of view. If deployed and anchored correctly, a structure in equilibrium will maintain its shape. Further conclusions about the nature of the equilibrium would require a sensitivity analysis which could give interesting insights to the properties of elastic grids like the proneness to pop into a different configuration in a loading scenario.

Notches allow the grid to relax into a lower energy state and increase the accuracy of the approximation. If a

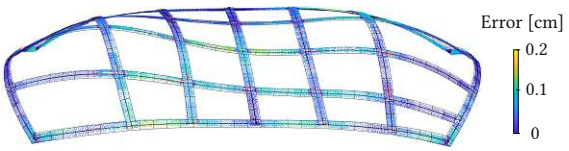

Fig. 2.13: Comparison of the simulation result (Section 2.5) to a laser scan of the example *Double Vault*. The figure shows the point cloud with simulation results overlayed. The notches are indicated in red. The lamellas have cross section of 0.1 : 1.0 cm. The color indicates the L^2 distances of the points to the lamellas. The total RMS error of the comparison is 0.06 cm.

grid without notches is deployed, it cannot approximate the surface patch $\mathcal{P}$, because distances between connections do not agree with the metric of $\mathcal{P}$. The effects can be observed in local buckling of members and general deviations from $\mathcal{P}$ (cf. Figure 2.10).

Finally, the current definition of distance maps is not compatible with holes in the surface, so the surface patch needs to maintain a single boundary.

2.7.3 Simulation

In our simulation, the energy term E_p is not physical, nonetheless, it acts as a source of pseudo-friction. We incorporated it to speed up the convergence of sliding movements and to make the simulation more realistic. As E_p causes connections to not fully utilize the notches, it interferes with the quality of the approximation (cf. Figure 2.10).

However, in our simulated models we registered that successively increasing μ first penalizes notches that belong to members with geodesics in areas of high K. Here geodesics are sensitive to imprecisions (e.g., from discretization of $\mathcal{P}$ or our numeric algorithm) and can exhibit deviations from the desired optimal path. This results in notches that are overly long.

The effects of E_p penalize sliding in high K regions first, which helps to trim such locally overly long notches (c.f. Figure 2.12, Waves Bump and Figure 2.14, Archway). Using the suggested settings, there is no significant negative effect of E_p on the quality of approximation as Table 2.1 and the Figures 2.12 and 2.14 show. It would be interesting to investigate a notch-penalty term that goes beyond imitating friction, but controlling the quality of the approximation via systematically reducing notch-lengths. A further investigation into similar concepts of handling notches is an attractive topic for future work.

The used simulation is based on the DER formulation and therefore uses the concept of linear material elasticity. It does not account for non-linear elastic effects like plasticity or the failure of members. Since we prescribe deformations in the deployment scenario, the resulting stresses have to be kept within an acceptable range. These arising stresses are higly influenced by crosssectional sizing.

2.7.4 Deployment

The deployment of an elastic grid is achieved by changing the angle $\bar{\alpha}$ and applying additional bending to guide it to the desired extrinsic shape. While our treatment of the deployment process is limited to the start and end configurations, without investigating intermediate states, we expect the process to be feasible if the end configuration is physically sound. All our experiments performed in accordance with this expectation, although a proof remains future work.

While deploying our physical models, we encountered that the static friction of wood can hinder connections from sliding freely. It thereby prevents the system from moving into a configuration of lower elastic energy. This can be countered by introducing some extra energy into the system that helps to overcome friction. Also finding fabrication methods that minimize friction between members are interesting problems to explore in the future.

Our approach is intended as a form-finding tool for 2d-3d elastically deployable gridshell structures. Although we only validated our approach with small scale models, [Panetta et al. 2019] examined the deployment of structures that use a similar deployment mechanism, but are bigger in size. Investigating how our approach can be adapted to the challenges of large scale architecture is an interesting engineering problem and a potential topic for future work.

Tab. 2.1: Quantitative results of our method. We measure the root mean square error (RMS) between the member centerlines and the target mesh: RMS_1 refers to grids without notches and RMS_2 to grids with notches. Timings are in seconds, t_{grid} refers to the computation times of generating the geometric elastic grid, t_{sm} to smoothing, t_1 refers to the simulation without notches and t_2 to the simulation with notches. $|M_V|$ expresses the number of mesh vertices and $|G_V|$ the number of grid vertices. Captions refer to examples Torus Wide, Waves Bump (Fig. 2.12), and Sphere, Double Vault, Waves, Archway, and Triple Vault (Fig. 2.14) respectively. Measured on an Intel Xeon E5-2687W v4.

	T.W.	W.B.	Sph.	D.V.	W.	A.w.	T.V.
width	100.0	100.0	100.0	100.0	100.0	100.0	100.0
depth	61.9	100.0	100.0	51.7	65.5	58.0	42.8
height	27.2	12.7	29.9	14.6	15.1	20.7	16.3
$\lvert M_V\rvert$	2122	3385	1083	571	1929	975	1322
$\lvert G_V\rvert$	767	388	414	300	328	625	494
t_{sm}	–	31.63	–	–	10.22	4.14	–
t_{grid}	5.33	5.62	1.29	0.68	2.10	1.50	1.67
RMS_1	1.17	1.47	1.09	0.69	0.59	0.63	0.69
RMS_2	0.27	0.78	0.58	0.31	0.43	0.42	0.46
t_1	1.92	12.60	6.05	2.25	3.03	37.74	3.50
t_2	6.48	57.22	4.25	4.05	9.56	85.43	5.80

2.8 Conclusions

We presented a novel approach for computational design of elastic gridshell structures that approximate smooth free-form surfaces by placing grid elements close to geodesic curves on the surface. Our method is inspired by architecture and design, and aims at simple fabrication, assembly, and most importantly at easy planar–to–spatial deployment. Moreover, it should provide an easy to handle tool for designers to create physically sound and aesthetically pleasing spatial grid structures based on the *active bending* paradigm.

Our solution is based on theoretical considerations and combines geometrical background with physical simulation. We have proposed a concept for the computation and simulation of such elastic grids. Additionally, we compared the results of the simulation to real fabricated grids and show that they match very well. Finally, we presented a set of examples with varying Gaussian curvature and fabricated a subset of them as wooden small-scale gridshells as a proof of our concept.

2.9 Acknowledgments

This research was mainly funded by the Vienna Science and Tech nology Fund (WWTF ICT15-082) and partially also by the Austrian Science Fund (FWF P27972-N31). The authors thank Florian Rist, Christian Müller, and Helmut Pottmann for inspiring discussions, as well as Etienne Vouga and Josh Vekhter for sharing code.

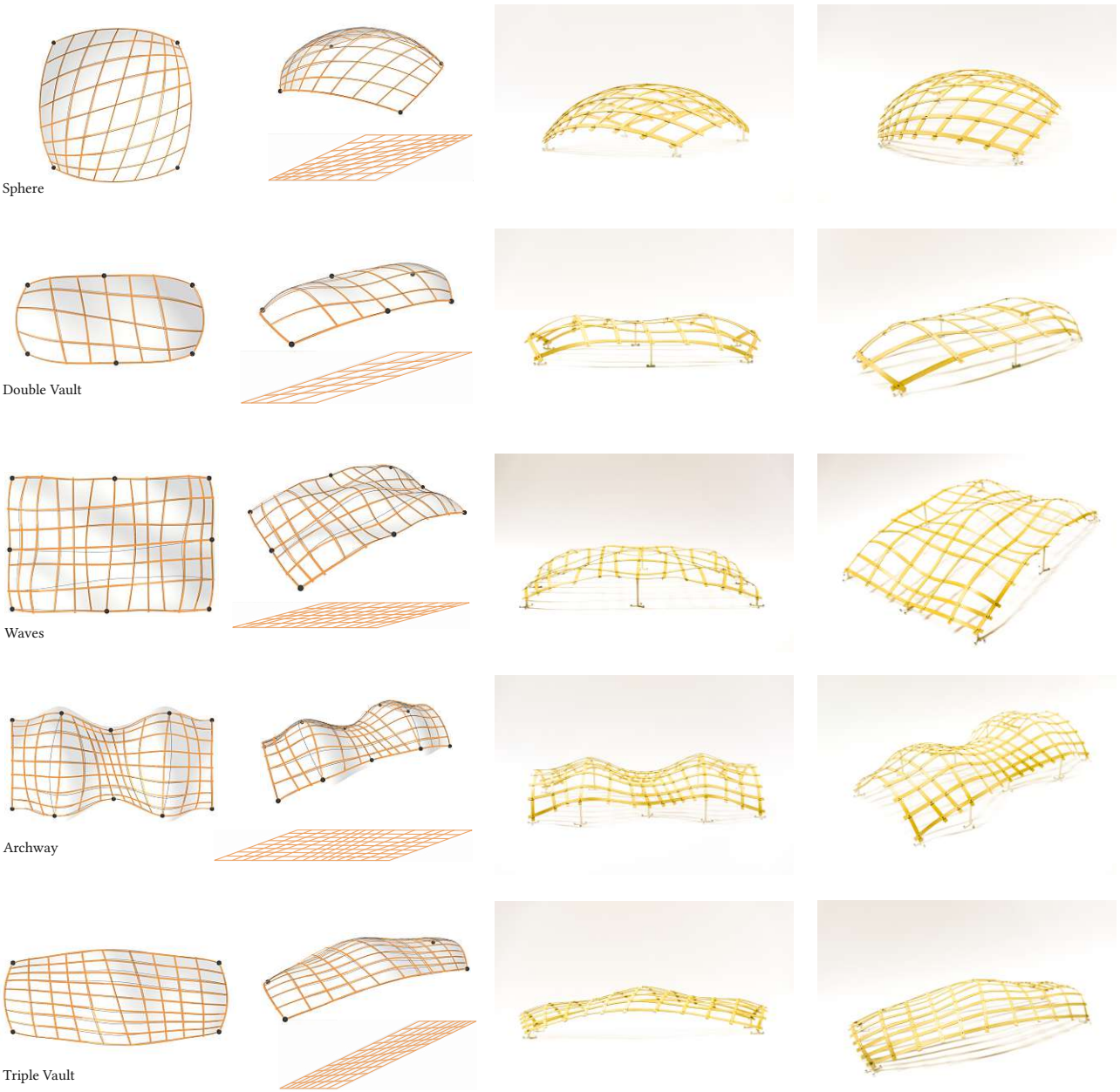

Fig. 2.14: Computed, simulated, and fabricated results of our method. Left: computed planar grids and renderings of the simulation. The orange strips follow our simulation with notches, the dark lines follow the shortest geodesics on $\mathcal{P}$. Right: photographs of our makes. Best seen in the electronic version in closeup.

Chapter 3

Design and Fabrication of Multi-Patch Elastic Geodesic Grid Structures

Authors: Stefan Pillwein, Johanna Kübert, Florian Rist and Przemyslaw Musialski

Published in: Computers & Graphics, Vol. 98, August 2021

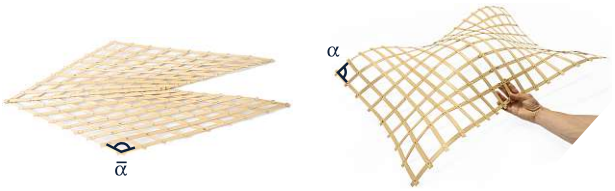

Fig. 3.1: An elastic geodesic grid in the planar and the deployed configuration, the deployment is based on $\bar{\alpha} \rightarrow \alpha$.

3.1 Introduction

In design and architecture, curved structures are aesthetically pleasing and functional, however, they are not always easy to produce. The curved shape of the structure in Figure 3.1 was generated by deploying a planar grid of initially straight but elastic elements fabricated as wooden lamellae. Such grids, referred to as Elastic Geodesic Grids (EGG) by Pillwein *et al.* [Pillwein et al. 2020b], can be deployed from a planar state to a spatial state that approximates a given design surface. The form-finding approach of EGG encodes the shape of the surface into the grid and produces planar grids with nonparallel members. This is the key factor for their deployment: The grids are rigid in the plane, but may easily buckle out of the plane and expand to their spatial configuration. This transformation can be performed simply by expanding the compact planar setup similar to a scissor-like mechanism.

This deployment approach makes the creation of doubly-curved shapes quick and material efficient, and the lightness and easy assembly make the grids applicable for mobile purposes. In addition, their fabrication does not need complicated techniques or advanced materials. We present a showcase model, which was built using simple resources, like plywood, screws, washers, and nuts. If advanced tools are not available, it could even be built using a tape measure, a drill, and a saw. Lightweight grid structures are particularly suitable for applications where large spans and low weight are required, which makes them potential candidates for architectural purposes.

A variety of shapes can be approximated with the EGG approach: they can approximate elliptic and hyperbolic surfaces (i.e., they may have positive as well as negative Gaussian curvature K), and multiple changes in curvature are also possible. Although the range of feasible surfaces is wide, the approach has a drawback for designers: the part of the surface that can be used for an elastic grid needs to be framed by a geodesic quadrilateral, which means the rest of the surface will be cut off.

Another set of problems comes with high Gaussian curvature K: First, if the peaks are too high, the strips on the surface (cf. Figure 3.1, right) will become very long, and at some point, it becomes impossible to fit them into the planar configuration. Second, high-K areas may cause geodesics to be non-unique, which makes the surface unrepresentable using the EGG approach. Previously these issues were solved by smoothing the surface [Pillwein et al. 2020b] until these problems vanish. This, however, is not desirable as it alters the target surface and its characteristics.

These problems can also be dealt with by decomposing the input surface into multiple patches. This approach omits the smoothing procedure and ensures better coverage of the design surface. Along the common boundary of two adjacent patches, the smoothness of the geodesic curves is broken, but the position and thus C^0-continuity is preserved. The boundaries of patches still need to be geodesic curves, but the placement and size of the patches can be chosen following the geometric features of the target shape. This splitting approach fits well with the idea of elastic geodesic grids, and a byproduct is a parameterization of the patch with geodesic curves.

Computing parameterizations for all patches before defining the members of the grid, allows an aesthetically pleasing and even distribution of members over the entire group of patches on the entire design surface. Figure 3.2 shows how such a parameterization can be used to propagate members across multiple patches.

In this paper, we extend the recently presented work of Pillwein *et al.* [Pillwein et al. 2020b; Pillwein et al. 2020a], in particular, our goal is to analyze how elastic geodesic grid models can be designed on challenging input surfaces that require multiple patches. We provide the following contributions:

- The geometric background of efficiently decomposing large and challenging input surfaces is discussed in detail. Such surfaces can have holes and non-convex boundaries. Practical rules for this process are presented and applied to three examples of free-form architecture.
- The propagation of grid members across patches and their even distribution is introduced.
- A showcase model and its fabrication are presented. Practical aspects like material, size, and strength are discussed.

In Section 3.2 we give an overview of the related work, in Section 3.3 we review the EGG approach, in Section 3.4 we examine how surfaces can be split effectively, and in Section 3.5 we discuss fabrication and design challenges. A showcase model, the fabrication process, and three design studies are presented in Section 3.6. Eventually, in Section 3.7 we feature a discussion of advantages and limitations.

3.2 Related Work

Active-Bending Paradigm In the computer science, architecture, and engineering communities, the *active bending* paradigm [Lienhard et al. 2013] and easy-to-use computational methods have sparked a new wave of interest in elastic structures that are deformed to create curved shapes. Until recent advances in computing elastic structures fast and physically accurate, they could only be form-found empirically [Gengnagel et al. 2013].

Gridshells and Deployment-Approaches A lot of research is currently being carried out on gridshell-structures that can be deployed. They can be classified based on their deployment mechanism: inscribed in a grid that is deployed [Panetta et al. 2019; Isvoranu et al. 2019; Soriano et al. 2019; Pillwein et al. 2020b] or by other external mechanisms like inflatable air cushions [Quinn et al. 2018]. We are interested in the first case. The design approaches of inscribing the deployment mechanism into the grid, however, differ a lot:

To create an X-Shell [Panetta et al. 2019], a planar grid layout is designed and actuated with a physical simulator. The grid curves of the planar layout do not have to be straight. In multiple layout iterations, the designer finds a satisfactory shape by changing the planar design. This approach does not depend on a target surface. Target surfaces, however, can be approximated if a good planar initialization is provided by the designer. In this case, a grid that approximates the target surface closely can be found using shape optimization. The bending and twisting behavior of the rods can be controlled by using different shapes of cross-sections. This has a direct effect on the shape of the deployed X-Shell, as the paper shows. The practical feasibility of these structures was investigated

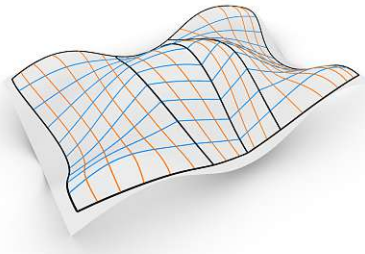

Fig. 3.2: A surface is split into multiple patches, boundaries are indicated in black, grid members in orange and blue. Blue members share start and endpoints.

hands-on with the construction of a pavilion of GFRP-rods, measuring 3.2 × 3.2 × 3.6 meters [Isvoranu et al. 2019].

The G-Shells approach [Soriano et al. 2019] proposes to planarize a specific geodesic grid using physical simulation inside an evolutionary multi-objective solver. This way, a geometric error is introduced, so the flat grid cannot be deployed to match the geodesic grid perfectly, but it can come close, creating beautiful shapes. G-Shells look similar to elastic geodesic grids, as they are also built from thin lamellae.

The EGG approach [Pillwein et al. 2020b] takes a design surface as input and results in a planar grid layout that can be deployed to approximate this surface. The layout is found geometrically and simultaneously on the design surface and in the plane. This makes the computation of grid layouts efficient, as neither design iterations nor physical simulations are needed for finding layouts. Despite the similarity of using geodesics as grid curves, in contrast to the G-Shells approach, EGG uses the concept of notches. This prevents introducing a geometric error in the grid layout, but also makes the deployment process more complicated, as sliding of members is necessary. However, this method does not feature arbitrary curve networks, as it is limited to geodesics as grid curves. This poses a restriction on the space of solutions of deployable grids using an inscribed deployment mechanism. Besides this limitation, design surfaces with high Gaussian curvature might need to be smoothed before a suitable grid layout is feasible. Some practical aspects of the EGG, like reducing friction in the joints or insights on scaling, were already investigated [Pillwein et al. 2020a]. The paper initially considers splitting design surfaces into multiple patches and provides first insights into it. However, in contrast to this paper, it does not explore splitting on an applied level. Also, the distribution and propagation of members across patches are not discussed.

Asymptotic curve networks were also explored as a basis for free-form structures [Schling et al. 2018]. Aside from their aesthetic qualities, these structures can be assembled from initially flat parts. They naturally transform to a curved state by their internal forces. This process induces a high twist of the members, which leads to a nonlinear geometric effect called helix-strain. It is typically negligible in conventional structures but needs to be taken

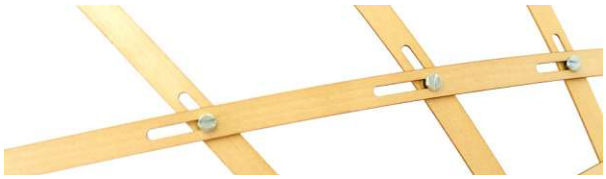

Fig. 3.3: Notches at the connection of grid members. They enable partial sliding, which is necessary for the close approximation of the design surface. They can be implemented by elongating holes.

into account for bendable lamella structures. Recently this effect was investigated for such structures specifically [Schikore et al. 2019]. However, asymptotic curve networks can only be found on surfaces with negative Gaussian curvature.

Other Deployable Surfaces Besides the domain of architecture, there has also been extensive research in the computer graphics literature on various methods for deployable structures. One more way to easily construct spatial shapes from flat sheets is by appropriately folding paper [Mitani et al. 2004; Massarwi et al. 2007], which is inherently related to the Japanese art of Origami [Dudte et al. 2016]. Other works deal with curved folds and efficient actuation of spatial objects from flat sheets [Kilian et al. 2008; Kilian et al. 2017a]. Elastic geodesic grids are related to these approaches in terms of being deployable from a planar initial state, however, the main difference is that they are elastic and approximate doubly-curved surfaces.

In fact, a lot of attention has been paid to the design of doubly-curved surfaces which can be deployed from planar configurations due to the ease of fabrication. One way of achieving this goal is by using auxetic materials [Konaković et al. 2016] which can nestle to doubly-curved spatial objects, or in combination with appropriate actuation techniques, can be used to construct complex spatial objects [Konaković-Luković et al. 2018]. The main difference to the EGG method [Pillwein et al. 2020b] is that these structures do not use elastic bending to reach the spatial shape.

Another recent approach [Malomo et al. 2018] is based on mesostructures that allow local changes in material behavior and can be connected to match target shapes. This approach has been tested on a larger scale by constructing a pavilion [Laccone et al. 2019]. In contrast to EGG, mesostructures are assembled from flat, flexible panels and do not rely on a scissor-like deployment mechanism.

Also, the idea of storing energy in a planar configuration to approximate spatial shapes has been explored. This can be done, for instance, by using prestressed latex membranes to actuate planar structures into free-form shapes [Guseinov et al. 2017], or to predefine flexible micro-structures which deform to desired shapes if they are combined and interact [Malomo et al. 2018]. A combination of flexible rods and prestressed membranes leads to Kirchhoff-Plateau surfaces that allow easy planar fabrication and deployment [Pérez et al. 2017]. The EGG approach is based on the assumption that the elastic elements can bend and twist, but not stretch, and must therefore maintain the same length in the planar as well as in the spatial configuration.

3.3 Elastic Geodesic Grids (EGG)

Using geodesics as grid curves is mainly motivated by practical reasons: A thin, straight strip of a material with sufficient elasticity can be wrapped on a surface and interpreted as a tangential strip. As a consequence, the centerline of the wrapped strip is a geodesic curve. Therefore, the planar grid can be fabricated from straight lamellae, and the deployment mechanism can be encoded in the planar layout.

Using geodesics as grid curves is also motivated by geometry and physics. Pillwein *et al.* [Pillwein et al. 2020b] show, if the mechanics of the grid strongly correlate with the geometric properties of geodesics, the shape of the deployed grid will match the shape of the initial geodesic grid closely. In the following, we briefly recall the concept of the EGG.

3.3.1 Geometric Background

Geodesics are curves on a surface whose geodesic curvature vanishes, i.e., their curvature is only their normal curvature on the surface. Their torsion is the geodesic torsion on the surface. These properties are very beneficial for the elements of physical grids of elastic elements: Bending should be easy around one axis but almost impossible around the other axis. Twisting should be easy, and stretching should be almost impossible. This behavior is inherent to thin lamellae made from a material that stretches very little. The principal normals of geodesic curves coincide with the surface normals, which is also the case where two geodesics cross each other.

The goal of an EGG is to approximate a design surface in the deployed state, hence, the shape of this surface needs to be encoded in the grid layout. Therefore, a layout is computed by finding a planar grid and a geodesic grid simultaneously, which must meet the following main conditions:

i. Total lengths of corresponding grid curves on the surface and in the plane are equal.

ii. Partial lengths between connections on boundary members are equal.

These conditions are based on the following idea: If (i) and (ii) are maintained and the planar grid is deployed, it is forced to take the shape of an isometry of the design surface. To match the extrinsic shape of the deployed grid to the design surface, it just needs to be bent.

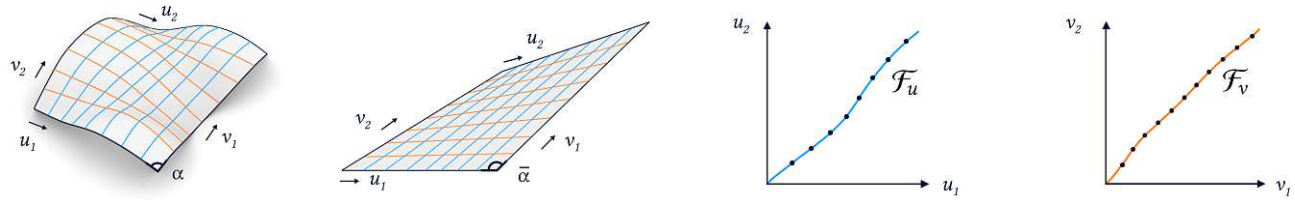

Fig. 3.4: Left: A surface patch and a planar patch carrying two families of grid curves. Right: Cladding functions $\mathcal{F}_u$ and $\mathcal{F}_v$ describe all possible choices of grid members, actual grid members appear as dots in the plot.

However, by complying with (i) and (ii), lengths between connections of inner grid curves will not match for arbitrary surfaces. It is known in differential geometry [Lagally 1910] that in general, a spatial geodesic grid cannot be planarized by only changing the angles between grid curves. The geometric error, caused by having non-matching lengths between curve-intersections, would impair the quality of the approximation. To avoid this problem, the concept of sliding notches at intersections of the curves of the grid was introduced [Pillwein et al. 2020b]. They allow for a certain amount of sliding and can be implemented physically by elongated holes.

The EGG approach intertwines geometry and physics to receive curved grids that approximate design surfaces. The shape of these grids is partly driven by geometric constraints and also by the stiffness of the lamellae w.r.t. bending, twisting, and stretching.

3.3.2 Computation of EGG Layouts

The computational aspects of designing a single elastic geodesic grid will be briefly summarized in this section; please refer to Pillwein *et al.* [Pillwein et al. 2020b] for a detailed description.

The design of an EGG begins by defining the patch on the surface that will be approximated by the grid. To frame this patch, a geodesic quadrilateral is formed by picking four geodesics as boundaries. The type of geodesics used to represent boundaries and grid members are shortest geodesics, i.e., the shortest paths between points on the surface.

A planar grid and the grid on the surface (cf. Figure 3.4) are computed simultaneously. Hence, the next step is to initialize the planar patch. It is defined by a quadrilateral in the plane with straight edges and the same side lengths as its counterpart on the surface. The planar quad has one degree of freedom, as one angle can be chosen freely to fix its shape.

Let us recall from Section 3.3.1, that a grid layout needs to comply with conditions (i) and (ii). Condition (ii) requires, that the parametrization of boundary members for the planar and the spatial configuration is the same. All corresponding boundary members are therefore parametrized with the same constant speed. Figure 3.4 shows the coordinates u_1 and u_2, which belong to the blue family of members. By choosing start and end coordinates (u_1, u_2), a blue geodesic on the surface and in the plane is defined. Feasible choices also need to obey condition (i), which demands equal lengths of the geodesics on the surface and in the plane.

Finding a single grid curve maintaining (i) and (ii) is quite simple: If we look at the setup in Figure 3.4, starting with an arbitrary $\overline{\alpha}$ and a combination of (u_1, u_2) coordinates, $\overline{\alpha}$, u_1 and u_2 can be varied until the lengths of the geodesics on the surface and in the plane match.

However, to find a global solution and cover both patches with valid grid curves, Pillwein *et al.* [Pillwein et al. 2020b] follow a different, more systematic approach: First, all candidates of geodesics between two opposite boundaries are described by so-called distance maps, which are functions that assign the geodesic distances to every combination of coordinates on opposite boundaries. Second, feasible geodesics are found by intersecting the distance maps. This process yields so-called cladding functions that are used to parametrize the corresponding surface and planar patches with geodesics (cf. Figure 3.4).

For the blue curve-family, two distance maps, one for the planar and one for the spatial configuration, need to be computed. The distance map for the surface patch $\mathcal{D}(u_1, u_2)$ is a function of the boundary coordinates u_1 and u_2, while the planar distance map $\overline{\mathcal{D}}(u_1, u_2, \overline{\alpha})$ is additionally also a function of the angle $\overline{\alpha}$.

If two distance maps $\mathcal{D}$ and $\overline{\mathcal{D}}$ for some specific $\overline{\alpha}$ are intersected, common points describe feasible corresponding geodesics on the surface and in the plane. There is one degree of freedom to find good-quality grids: the angle $\overline{\alpha}$. Good choices of this angle deliver compact planar layouts and allow a smooth deployment of the grid. However, poor choices result in extra crossings of grid members or introduce triangles to the grid. This would destroy the kinematic mechanism, making deployment impossible. In an optimization procedure a feasible angle $\overline{\alpha}$ is computed.

Valid cladding functions $\mathcal{F}_u$ (blue curve-family) and $\mathcal{F}_v$ (orange curve-family) are bijective, establish a relationship between the boundary coordinates, and can be seen as geodesic parametrizations. In other words, cladding functions enable an easy generation of a grid layout, govern the direction of geodesics and the overall appearance of the grid. The layout can then be defined by just picking points on the cladding functions, or by using more elaborate approaches. Please refer to Pillwein *et al.* [Pillwein et al. 2020b] for more details.

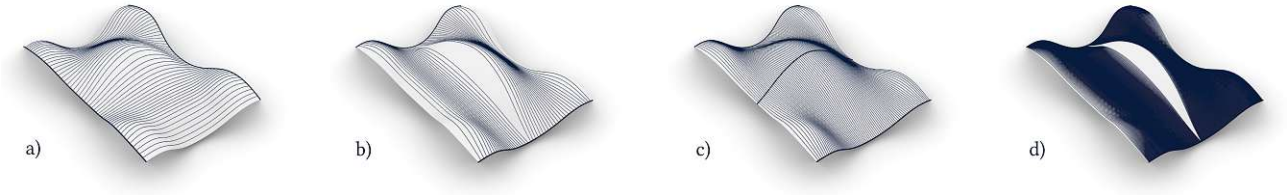

Fig. 3.5: Shortest geodesics on a design surface. a) The first family of shortest geodesics covers the surface nicely and does not require splitting. b) The second family of shortest geodesics does not cover the surface completely. c) Splitting the surface into two patches enables an even coverage of the design surface. d) The problem of uncoverable regions on the surface does not depend on the number of shortest geodesics.

3.4 Splitting the Design Surface

The objective of decomposing the design surface into multiple patches is twofold: First, if the boundary of the design surface is non-geodesic or even non-convex, using multiple patches allows for better coverage of the design surface, as a single patch may lead to big cut-offs (cf. Section 3.3.2). Second, if the design surface has high-K regions and thus hosts non-unique shortest geodesics, it is not representable by a single EGG. A potential solution to this problem is to smooth the surface, however, we want to omit changes of the surface characteristics. The occurrence of such geodesics is strongly connected to the size of the area on the surface that should be covered by an EGG. This suggests that using multiple smaller patches is another suitable strategy to dispose of non-unique shortest geodesics. We will discuss this problem in detail and present a link between the Gaussian curvature of the surface and the uniqueness of shortest geodesics.

After reviewing some aspects of differential geometry in Section 3.4.1, we will discuss suitable shapes for surface patches and cladding functions in Section 3.4.2. In Section 3.4.3 we present an empiric method for decomposing the surface and in Section 3.4.4 we show, how to achieve C^0-connections of members at adjacent boundaries.

3.4.1 Uniqueness of Shortest Geodesics

Regions of high Gaussian curvature K are prone to host non-unique shortest geodesics, as Figure 3.5 illustrates. It shows that the central region cannot be covered by shortest geodesics between the boundaries that are further apart. Moreover, one combination of points even yields two valid shortest geodesics. The existence of such regions and non-unique shortest geodesics is inherently connected. A check for uniqueness is known in differential geometry [do Carmo 1992]:

$$ir(p) \geq \frac{\pi}{\sqrt{K_{\max}}}. \tag{3.1}$$

The left side of the inequality is the injectivity radius $ir(p)$ for geodesics for each surface point p, and $K_{\max}$ is the maximum of the Gaussian curvature of the respective patch. In essence, if all geodesics on the surface patch are shorter than the value on the right-hand side of Expression (3.1), non-unique shortest geodesics do not appear.

Reducing the size of surface patches around a maximum of K eliminates problems with non-uniqueness. If the size of the patch is small enough, geodesics will be shorter than $ir(p)$, and therefore unique. However, Expression (3.1) is only useful as a quick check to approximately limit the size of the patch.

Clever splitting of the surface patch can reduce the problem further: Expression (3.1) does not address the location of the peak on the patch (far away from or near a boundary). The most effective way to avoid non-unique shortest geodesics is to place the boundaries of the patches directly over the peaks. This is illustrated with a simple example, shown in Figure 3.5 b): No shortest geodesic leads over the peak, and therefore the part of the surface that is not covered can not be encoded in the grid. If the surface is split and an additional geodesic boundary leads over the peak, shortest geodesics become unique.

To precisely check for uncoverable areas around a Gaussian curvature peak $p_{\max}$, we use a criterion based on geodesic distances, introduced by Pillwein *et al.* [Pillwein et al. 2020b], which we summarize briefly. Figure 3.6 depicts the process: Imagine a geodesic through $p_{\max}$, starting at p_1 and ending at q_1. If it is longer than the shortest geodesic connecting p_1 and q_1, this results in an uncoverable gap. To perform the check, we first compute geodesic distances from $p_{\max}$ to both boundaries and one from the

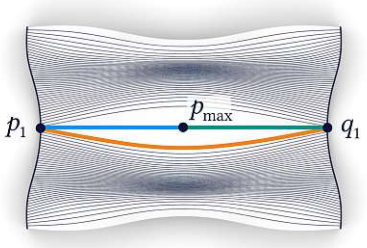

Fig. 3.6: The curvature of the central peak is too high, it causes the orange shortest geodesic to omit it. We check the size of the gap indirectly by the ratio η, which is the sum of the lengths of the blue and the green geodesic, divided by the length of the orange geodesic.

point p_1 to the opposite boundary, where p_1 is the closest point to $p_{\max}$ on the first boundary. This provides the distances $d(p_1, q)$ to the points q of the opposite boundary as well as $d(p_1, p_{\max})$ and $d(p_{\max}, q)$. We find q_1 at the location of the minimum of $d(p_1, p_{\max}) + d(p_{\max}, q) - d(p_1, q)$. If this minimum is close to zero, the peak can be covered completely. We compute the ratio of distances:

$$\eta = \frac{d(p_1, p_{\max}) + d(p_{\max}, q_1)}{d(p_1, q_1)},$$

to indirectly measure the size of the gap. Pillwein *et al.* [Pillwein et al. 2020b] propose to restrict values to a maximum of $\eta = 1.0015$. We use this check as an instrument to systematically decrease the size of a surface patch until uncoverable areas vanish.

3.4.2 Shapes of Patches and Cladding Functions

Some combinations of shapes of the surface patch and the planar patch are undesirable in terms of the aesthetics and the functionality of the grids. Please recall, that the deployment of an EGG strongly depends on changing angles between the members (cf. Figure 3.1). A big difference between these angles $\bar{\alpha}$ and α is important for smooth deployment and can be achieved if the planar patch can be "collapsed", i.e., has one very long and one very short diagonal.

If the quad framing the surface patch has opposite sides of equal lengths, the planar quad can be collapsed perfectly to a straight line. Otherwise, there is less freedom to collapse the planar quad, as convexity must be maintained. To put it simply: The better a planar quad can be collapsed, the easier it is to fit long strips on the surface into the planar configuration.

The suitability of a surface patch for an EGG can be checked by a simple geometric criterion [Pillwein et al. 2020b], which supports the above considerations:

$$(e - \bar{e})(f - \bar{f}) < 0\,, \tag{3.2}$$

where e, f are the lengths of the geodesic diagonals on the surface patch, and $\bar{e}$, $\bar{f}$ are the lengths of the diagonals in the planar patch. If one diagonal of the planar patch is shorter than the corresponding diagonal of the surface patch, the other diagonal must be longer.

Figure 3.7 shows how the shape of the planar patch influences the shapes of the cladding functions $\mathcal{F}$. They play a crucial role because they define the geodesic connections. Figure 3.7 also shows, the more collapsed the planar patch is, the more "parallel" the appearance of the grid members becomes. A strong concentration of members is unfavorable for deployment, but can easily be recognized in the cladding functions, as they are linked to very steep or flat slopes. To prevent such concentrations, we set constraints on the slopes of the cladding functions as proposed by Pillwein *et al.* [Pillwein et al. 2020b] in the form of lower and upper bounds $k_{\min}$ and $k_{\max}$.

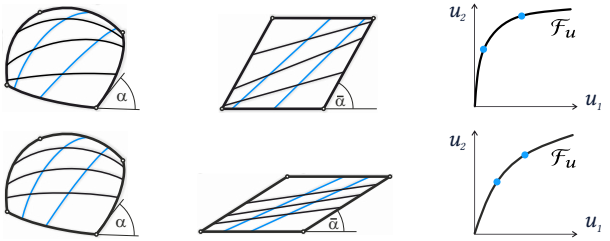

Fig. 3.7: The influence of $\bar{\alpha}$ on the shape of the planar grid and the cladding functions $\mathcal{F}$. Very steep or flat slopes of $\mathcal{F}$ indicate a concentration of members which is undesirable for the aesthetics and the deployment of the grid.

3.4.3 Splitting Strategy

Finding the best split locations is a difficult problem; it is a mix of many subjective criteria related to aesthetics (number of patches, minimum patch size, patch aspect ratio, location of supports, etc.) and geometric restrictions (unique geodesics, suitable cladding functions, etc.). We provide two workflows to design a multi-patch EGG: Workflow 1, presented in Algorithm 1, is fully automatic, it lets a designer specify patches on the surface freely and iteratively subdivides them until all patches are feasible. Workflow 2, presented in Algorithm 2, is a semi-automatic, more informed process and aims at keeping the number of patches low. Please note, that this process still offers a lot of freedom for the intents of a designer.

Let us first summarize problems that induce a split: The cut-offs of the design surface using a single EGG are too big. There are non-unique shortest geodesics, i.e., some areas of the surface patch cannot be covered by shortest geodesics (cf. Section 3.4.1). Grid members are too concentrated in certain areas of the surface patch, i.e., the slopes of the cladding functions are too steep or too flat (cf. Section 3.4.2).

Algorithm 1: Patch the Surface using Workflow 1

```
Provide an initial layout of patches;
while Patches cannot be covered, η > 1.0015 do
    if η > 1.0015 for one family of members then
        Split the patch by introducing an edge over p_max;
    else if η > 1.0015 for both families of members then
        Split the patch by introducing a corner at p_max;
    end
end
while Slopes of F_u, F_v violate k_min, k_max do
    if k_min, k_max is violated for one family then
        Split the patch by introducing an edge over p_max;
    else if k_min, k_max is violated for both families then
        Split the patch by introducing a corner at p_max;
    end
end
```

Algorithm 2: Patch the Surface using Workflow 2

```
while Not all regions of high K are patched do
    Identify remaining region of highest K;
    Find p_max and compute r = π/√K_max;
    Draw a circle (p_max, r) on the surface;
    if The size of the circle is suitable for a patch then
        Define a patch with corners on the circle;
    else
        Introduce a corner at p_max, use the directions of the
          principal curvatures κ1 and κ2 as guides for the
          directions of the patch edges;
        Draw a patch which is split by the edges through p_max
          into four parts, each of them corresponding to the
          size of the circle;
        Grow the patches outwards iteratively until either the
          patches are big enough for designer demands or
          η ≥ 1.0015;
        Check if two adjacent patches can be merged using η;
    end
    if Slopes of F_u, F_v violate k_min, k_max then
        Decrease the size of the patch to make the members of
          the respective family shorter until k_min, k_max are
          met;
    end
end
while Surface is not fully patched do
    Choose a region in a greedy manner;
    Use similar sized patches in regions with higher K;
    Use larger patches in regions with low K;
    if Slopes of F_u, F_v violate k_min, k_max then
        Decrease the size of the patch to make the members of
          the respective family shorter until k_min, k_max are
          met;
    end
end
```

Both workflows have the objectives of ensuring full coverage of the patches and suitable cladding functions. We check them using η, $k_{\min}$, $k_{\max}$, and adjust the patches by splitting them or decreasing their size until they are feasible. Workflow 2 is based on defining the patches in regions of the highest K first because they are prone to uncoverable areas and have a high aesthetic impact on the overall design. After that, the remaining parts of the surface are patched in a greedy manner.

3.4.4 Distribution of Members in a Multi-Patch EGG

To create an aesthetically pleasing multi-patch EGG with best coverage, we distribute members equidistantly across each patch and make sure that connections at adjacent patch boundaries maintain C^0-continuity.

A member of the u-family is defined by its start and end coordinates u_1 and $u_2 = \mathcal{F}_1(u_1, \bar{\alpha})$ respectively. The subsequent members in following adjacent patches can be denoted at their boundaries as $u_3 = \mathcal{F}_2(u_2, \bar{\alpha}_2)$, etc. Using this notation, we formulate an optimization problem, where we minimize the normalized squared distances between member endpoints on the boundaries:

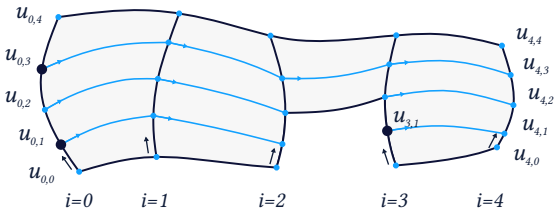

Fig. 3.8: Members of the blue family are propagated using the cladding functions $\mathcal{F}_1, \mathcal{F}_2, \mathcal{F}_3, \mathcal{F}_4$. Black dots represent u-values that define members, blue dots indicate how members are propagated. If there are smaller patches within a family of grid members, like patch number 3, they define an original member. Please note, that back-propagating members is performed using $\mathcal{F}_i^{-1}$.

$$\min_{\mathbf{u}_i} \sum_{i=1}^{n} \omega_i \left\langle \Delta\mathbf{u}_i, \Delta\mathbf{u}_i \right\rangle, \tag{3.3}$$

with

$$\Delta\mathbf{u}_i = \frac{1}{l_i} \begin{bmatrix} u_{i,1} - u_{i,0} \\ u_{i,2} - u_{i,1} \\ \dots \\ u_{i,m} - u_{i,m-1} \end{bmatrix},$$

where n is the number of boundaries, i is the index of the current boundary, $m-1$ is the number of members, l_i is the length of the respective boundary, ω_i is an importance factor for the respective boundary, and $u_j, \dots, u_m$ are the coordinates of start or endpoints on the respective boundary. Please note, that the second family of members is expressed using v in our notation (cf. Figure 3.4) and solved independently.

We solve Problem (3.3) using a gradient-based sequential quadratic programming algorithm in MATLAB. The number of members is fixed during the optimization, members due to boundaries of smaller patches appear as constraints as depicted in Figure 3.8. It also shows a family of members on multiple patches, the variables for Problem (3.3) are the u-values, displayed as black dots. Other u-values are computed by propagating members using the cladding functions. Figure 3.9 shows the result of the optimization on a set of patches.

3.5 Fabrication

There are challenges associated with the design and the implementation of EGG on different scales. This section presents some of the challenges and possible solutions. The showcase model shown in Figures 3.16 and 3.20 was used to evaluate these approaches. The measures presented are intended to improve the feasibility of EGG on an applied level.

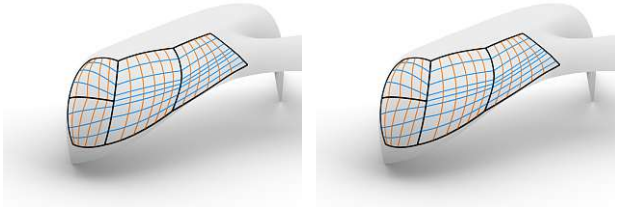

Fig. 3.9: Distribution of members on a multi-patch EGG design. Left: Members are distributed evenly on the leftmost boundary and simply propagated to the other patches. Right: The evenness of members is improved by solving the Optimization Problem (3.3).

3.5.1 Notches and Friction

The quality of the approximation strongly depends on the concept of notches, as outlined in Section 3.3.1. Notches enable grid members to slide for a predefined length and direction at their connections. Figure 3.3 shows notches in a physical grid.

While sliding of members in the notches delivers perfect results in simulations, friction poses a problem for the sliding process of physical grids. lamellae often get stuck in the notches, because forces that are supposed to push the lamellae in the right direction inside the notches are counteracted by friction. By interfering with sliding, the quality of the approximation suffers, and local stresses arise as some lamellae buckle. Also, the dissipation of energy by friction increases the force necessary to deploy the grid.

The regions that contribute to the overall friction during deployment are the contact areas of lamellae, the screw threads, and the notches, and the lamellae and the washers. Table 3.1 summarizes empirically determined friction coefficients. The goals of easy deployment on one hand and secure final fixing, on the other hand, can be fulfilled by reducing the friction between the lamellae but maintaining friction between lamellae and washers.

An effective measure to reduce friction is to equip the lamella-to-lamella contact areas with a PTFE-foil layer. The friction coefficient of PTFE is quite low, and it is robust. For every notch, an individual PTFE sticker was cut from an adhesive foil. The stickers cover the immediate contact area for every notch, so there is no contact with the rough wooden surface of the lamellae. Brass shells furthermore reduce the friction of the screw in the notch. Figure 3.10 illustrates the measures taken to reduce friction.

3.5.2 Grid Size

Fabricating small prototypical models to investigate the qualities of the design is common practice in architecture. Once a suitable material is found, designing EGG models on the same scale is easy.

Analyzing existing models [Pillwein et al. 2020b], we provide the rough empiric rule for small and medium-sized

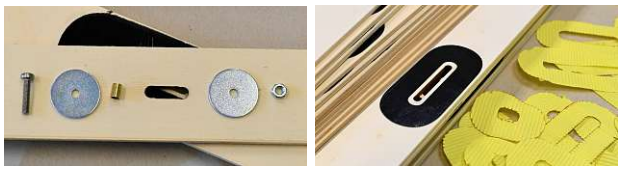

Fig. 3.10: Design features to minimize friction. Left: Contact of the screw thread and the notch wall is prohibited by a brass shell. Right: PTFE-foil stickers reduce friction at lamella-to-lamella contact areas.

models, that a lamella-width of around two percent of the desired output size works well. The thickness of a lamella follows from the considerations in Section 3.3.1 as smaller than $1/5$ of the width. Please recall, that a distinct width-to-thickness ratio is necessary for the grid to behave like a geodesic grid. Building EGG models on a larger scale is not straightforward, which will be discussed in this section.

The shape of a deployed elastic grid is driven by the stiffness parameters of the lamellae. The related X-Shells approach [Panetta et al. 2019] even uses different shapes of cross-sections, which induce different stiffness parameters to influence the shape of a deployed X-Shell. The stiffness of an element like a lamella can be expressed w.r.t. the different types of deformation, like bending and twisting. It determines the amount of stress which is induced by the deformation. The magnitude of a stiffness parameter is set by the geometry of the cross-section and by the material parameters. In our case, when wrapping a lamella on the surface patch, bending and twisting are prescribed.

To get an insight into the matter, we will first consider scaling up the whole structure just linearly, including the cross-sections of the lamellae, and have a look only at the internal stresses caused by bending.

Let us further assume, that the lamellae of the deployed grid agree well with the scaled surface patch, no matter how high the scaling factor is. This enables us to compute the stresses due to bending w.r.t. a scaling factor f:

$$\sigma_{B,max}(f) = \pm \frac{M(f)}{I(f)} \frac{tf}{2} = \pm \frac{E\, I(f) \frac{\kappa}{f}}{I(f)} \frac{tf}{2} = \pm \frac{E\kappa t}{2},$$

where $\sigma_{B,max}$ is the maximum stress induced by bending, M is the bending-moment, I is the moment of inertia, κ is the curvature, and t is the thickness of the lamellae. This means that the bending stresses are constant under linear

Tab. 3.1: Empirically determined friction coefficients μ for static and sliding friction; the evaluated plywood is poplar.

Material	μ_{static}	$\mu_{sliding}$
Plywood-Plywood	0.436	0.273
PTFE-PTFE	0.163	0.091
Plywood-Steel	0.252	0.203

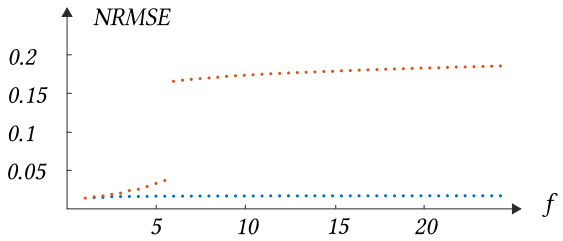

Fig. 3.11: The effects of scaling an EGG. The NRMS-Error is used to measure the deviation of scaled simulated grids to the design surface. Blue dots represent simulation results, if gravity is neglected, orange dots represent results including gravity. The jump represents the collapse of the structure under its own weight.

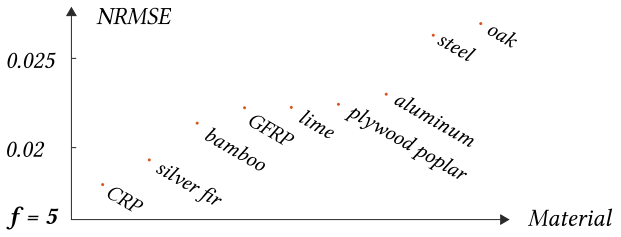

Fig. 3.12: The performance of different materials at $f = 5$. The plot shows that fiber-reinforced polymers or timbers are quite suitable. High-density materials like steel or oak perform worse, although they have a high elastic modulus.

scaling, as the curvature decreases at the same rate as the thickness of the cross-section increases.

The shape of a model is determined by the geometric boundary conditions (deploying a grid and fixing it to supports) and stiffness. This interplay leads to internal stresses. For EGG they are mainly caused by bending the lamellae and their self-weight. As the scaling factor f increases, stresses caused by self-weight grow significantly, whereas stresses caused by bending remain constant. The strong increase of stresses caused by self-weight is due to the fact that it grows cubically w.r.t. the scaling factor f:

$$F_G(f) = m(f)g = V(f)\rho g = twlf^3\rho g,$$

where w is the width and l is the length of a lamella. Figure 3.11 shows numerical results of the impact of scaling on the shape, generated with a physical simulation using the Discrete Elastic Rods model [Bergou et al. 2008; Bergou et al. 2010]. The implementation we used is based on the implementation by [Vekhter et al. 2019], which features the simulation of self-weight. To compare the shapes of linearly scaled versions of the small grid in Figure 3.1, the Normalized Root Mean Square Error (*NRMSE*) was used. The difference between the predicted and the observed values in the *NRMSE* are the distances d_i between points on the centerlines of a simulated deployed grid and their nearest neighbors in the surface patch. The inverse scaling factor acts as the normalization factor:

$$NRMSE = \frac{1}{f}\sqrt{\frac{1}{n}\sum_{i=1}^{n} d_i^2}\,.$$

Figure 3.11 shows, that linear scaling does not influence the shape significantly, as long as gravity is neglected. However, taking gravity into account, the cubical increase of gravitational loads makes linear scaling feasible only for small scaling factors. Figure 3.13 shows the simulated shape of the desktop model, which corresponds to the leftmost data point in Figure 3.11 ($f = 1$).

Strategies for large Grids To enable the construction of larger structures, the gravitational forces need to be kept small, while we expect a positive effect on the shape when increasing the relevance of bending stresses. There are several options to tackle this problem:

i. Choose suitable materials.

ii. Change the grid design by introducing more members with smaller cross-sections.

iii. Introduce multi-layered structures.

iv. Introduce a support at every connection on the boundary.

We will subsequently discuss approaches (i) and (ii) in detail. Approach (iii) is referred to future work and approach (iv) is straightforward.

Changing the material allows an improvement in two ways: Making it stiffer by increasing the elastic modulus E, and making it lighter by reducing the density ρ. It is therefore practical to look for a material with the right ratio of the two. In fact, this ratio is called specific modulus $\lambda = E/\rho$ and is well known in light-weight engineering like the aerospace design. There, it is used for parts whose shape is driven by stiffness, like the wings. Figure 3.12 shows the impact of using different materials on the shape of an initially desktop-sized EGG when scaling it by a factor of $f = 5$. However, when increasing the elastic modulus, there is a restriction that needs to be considered. The internal stresses due to bending σ_B grow proportionally, as the curvature κ and the thickness t of the lamella are prescribed. Therefore, it needs to be checked, that the stresses do not exceed the strength of the material.

Another aspect for the choice of material, is caused by geometry: As the ribbon-like lamellae are wrapped onto the surface, they need not only to bend but to twist as well. In extreme cases, on surface regions of negative Gaussian curvature, lamellae may even be almost or completely straight, but still have to twist. If such a lamella is made from material that allows no in-plane stretching, it needs to buckle. Using materials like wood does not cause trouble: the fibers are approximately perpendicular to the cross-section, and the outer fibers can stretch minimally

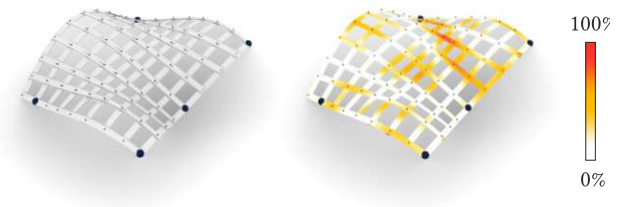

Fig. 3.13: Simulated elastic grid and deviations to the design surface. The deviations relate to the Euclidean distance w.r.t. the width of a lamella. The mean deviation is 2 mm for absolute dimensions of 0.43 x 0.57 x 0.1 m.

w.r.t. the fibers close to the centerline. Recent research on grid structures made of thin lamellae that undergo large torsion [Schikore et al. 2019] even shows, that metal is a suitable material.

Scaling a structure non-uniformly is feasible only within certain width-to-thickness bounds, as mentioned earlier. Increasing the thickness without keeping a high width-to-thickness ratio will corrupt the EGG design concept, and thus worsen the quality of the approximation.

Large grids, spanning meters to tens of meters, can furthermore not be obtained by simply scaling a desktop prototype grid. The layout needs to be adapted, which means introducing more and smaller lamellae. This can be explained simply by considering the effects of gravity: Doubling the number of lamellae doubles the weight of a grid. Scaling the lamellae by a factor of two increases the weight by a factor of eight.

The insights on shape and material suggest, that the bigger an EGG gets, the more important high-quality material and the dimensions of the cross-sections become. Good material choices can be achieved by tuning the specific modulus λ to receive the best possible shape. However, finding the best cross-sectional dimensions and number of lamellae for large grids is a difficult engineering task that is out of the scope of this paper.

3.5.3 Deployment

In theory, an EGG can be deployed to match all isometries of the input surface patch, which is due to the design concept. If the deployment is not guided, the grid will take the shape corresponding to minimal elastic energy. This shape will most certainly not correspond to the shape of the input surface patch.

To fix this, first, the deployment process of the grid needs to be guided. This means that the shape induced by deployment needs to be checked and adjusted, to ensure that the grid buckles in the right way. To put it simply: All bumps, that are supposed to go up, actually go up. Adjusting the shape of the grid is easy at the beginning of the deployment, as elastic forces are still low. Depending on the complexity of the design surface, however, this step can be tricky. So, for large and complex designs, it makes sense to set a maximum patch size w.r.t. handling of the grid. Multi-patch EGG can be deployed and combined sequentially, which simplifies this task.

Second, after deploying, the grid needs to be bent to match the shape of the surface patch. To ensure this, a set of supports is used. Good choices for locations are intersections of grid curves with boundaries. A support is defined by a point and a plane: The point corresponds to the intersection point and the plane corresponds to the tangent plane at this point.

Adjacent grids can be simply connected along their common lamellae, as can be seen in Figure 3.14. Please note, that there are no notches on boundary members.

3.6 Results

In this section, we present models, designed with the EGG approach, using multiple patches. First, the whole design and fabrication process of a showcase model is presented. Second, some iconic design surfaces from free-form architecture are used to explore the potential of the multi-patch EGG approach on an architectural scale.

3.6.1 Showcase Model

As a starting point for a model of a few meters in size, a small-scale prototype was built. It was intended to assess the aesthetic and structural qualities of the design. The first attempt to build the full-scale model failed, because of poor material properties. The second attempt, however, was successful. The production process was automated as much as possible, e.g. by laser-cutting the notches and lamellae.

Prototype The design was created by an architecture student without particular prior knowledge of elastic structures or differential geometry. The student was given access to the EGG pipeline via a Grasshopper node. The simulated shape of the current design and the laser-cutting plans were output again in Grasshopper. Out of many design candidates we chose the structure of Figure 3.14, which features two symmetric modules that can be used separately or together. The measurements of the prototype were 0.85 x 0.57 x 0.15 meters, and it was built from 1 mm thick and 10 mm wide limewood lamellae. A plan for laser-cutting the lamellae is provided in Figure 3.18. The 3D-printed supports feature inclined contact areas. The prototype kept its shape even with as few as four supports, which was a relevant design feature. Tests suggested a high degree of structural stiffness and load-bearing capacity. The total weight of the model was 160 grams, the applied weight in Figure 3.14 was 1135 grams. This gives a promising load-to-self-weight ratio of about 7.

Fabrication Process Fabricating the full-scale model featured the following steps: laser-cutting the lamellae and the notches, sanding and coating the lamellae, cutting the

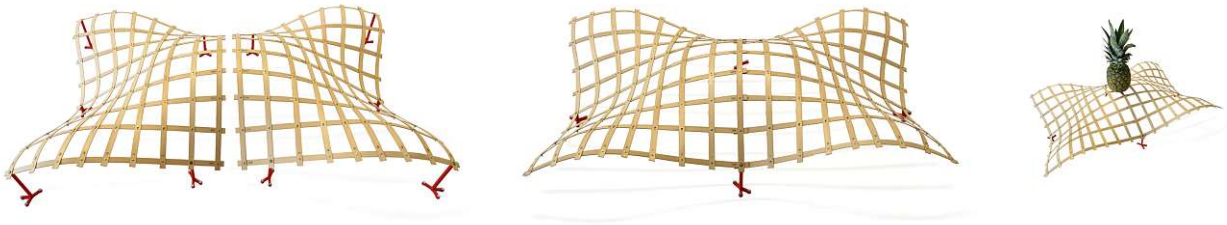

Fig. 3.14: Modules of the small-scale prototype and a test of the structural behavior. Left and middle: Modules can be used separately or combined. Right: A test of the load-bearing capacity of the grid.

PTFE-stickers, assembling the grid, and casting the supports. The different steps of the fabrication process can be seen in Figure 3.19.

As a construction material, plywood was used. It is cheap, available in big panels, and easy to machine. The plywood we used had three layers and was 3 mm thick. We decided to use a laser-cutter to produce the lamellae and notches. Our Trotec Speedy 500 has a back flap that can be opened. This enables easy production, as the plywood panels could be pushed through the flap. The cutting happened in multiple steps: after cutting one segment, the plywood panel was pushed forward and adjusted to cut the next segment.

The supports were cast from concrete and designed to be stable under their own weight, but also light enough that they could be carried. The inclined contact areas of the supports were realized with wooden wedges mounted to the supports.

Failed Model In the first iteration of building the full-scale model, the change of material from high-quality limewood to simple plywood had negative side effects. The structure failed under its own weight due to very flexible lamellae. The reason for the flexibility was the wrong fiber orientation of the top layers of the plywood. This reduced the elastic modulus E to about $1/5$ of what was expected (E of timber perpendicular to fiber direction is about $1/5$ of E parallel to fiber direction). Therefore, the top layers hardly contributed to the structural performance but made up $2/3$ of the self-weight.

Fig. 3.15: One module of the failed medium-scale model. The structure is not able to carry its self-weight. Some curvature features can be recognized, however, the structure as a whole performs rather poorly.

Table 3.2 summarizes the values of the specific modulus for the materials we used. Comparing the specific modulus of plywood (birch) to limewood, it is only about $1/3$. Essentially, the plywood was way less performative and much heavier, which is exactly the opposite of what would have been appropriate for a larger grid (cf. Section 3.5.2).

Successful Model The second attempt to build the full-scale model succeeded, using poplar plywood for the lamellae. This plywood is quite efficient, as Table 3.2 shows. In the deployed state the structure measures $3.1 \times 2.1 \times 0.9$ meters (including supports) and has a self weight of 7.1 kilograms. This makes a weight-to-span ratio of 1.09 kg/m^2 and a thickness-to-span ratio of $1/516$. In Figure 3.16, the closeness of the shapes of the small-scale prototype and the medium-scale model is obvious.

The deployment of the model was done by five people: four of them held the structure and one attached it to the supports. Some intermediate steps of the deployment process can be seen in Figure 3.20. On the site, the grid was first bent and fixed to two supports, then deployed. Pre-bending the grid before deployment eliminated problems with buckling into undesired configurations, and the grid automatically deployed correctly. Deployment worked smoothly and could be carried out by a single person. Sliding of the lamellae along the notches worked partially, however, the lamellae could be pushed into the right configuration by a single person without applying much force.

Tab. 3.2: The specific modulus λ of the materials used ($\perp$ and $\parallel$ indicate fiber direction). Limewood was used for the small-scale prototype, the failed version was built from birch plywood, and the successful medium-scale model was built from poplar plywood.

Param.	Unit	Lime-wood $\parallel$	Plywood birch $\perp$	Plywood poplar $\parallel$
E	$[GPa]$	9.1	4.0	7.6
ρ	$[g/cm^3]$	0.50	0.65	0.43
$\lambda = E/\rho$	$[10^6 m^2/s^2]$	18.2	6.15	17.7

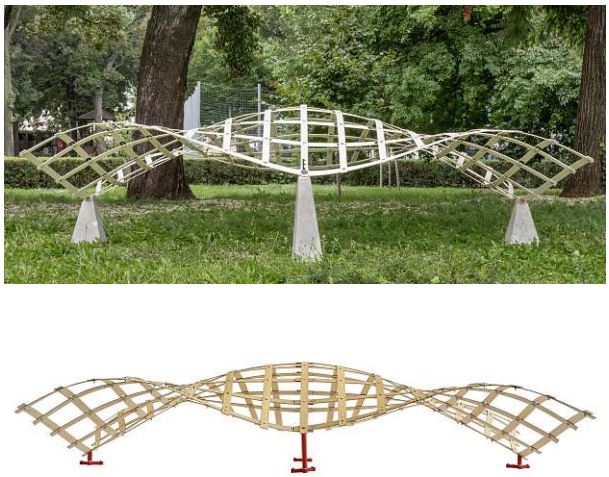

Fig. 3.16: Side-view comparison of the shapes of the small-scale prototype and the showcase model. Good agreement of the shapes is obvious.

3.6.2 Examples from Architecture

To explore the multi-patch EGG approach, three iconic design surfaces were used: The Great Court of the British Museum, designed by Foster and Partners, the tip of the Lilium Tower, designed by Zaha Hadid Architects, and the Yas-Hotel, designed by Asymptote Architecture. The surfaces were split into patches, using the rules of Section 3.4.3. The results are displayed in Figure 3.17. They show the design surfaces, how they are split, the geodesic grids, and the simulated shapes of the grids. The black dots indicate the position of supports. Table 3.3 summarizes model dimensions and deviations from the design surface. Please note, for designing the patches to cover the Yas-Hotel, the surface was extended and both holes were closed, all patch boundaries are shortest geodesics.

3.7 Discussion and Conclusions

In this paper, we investigated the idea of approximating sophisticated free-form surfaces with multiple elastic geodesic grids, to demonstrate the potential of the EGG method. This was done on a theoretical and geometric level, as well as hands-on, by building a showcase model. We discussed the cases when the EGG approach requires a design surface to be decomposed into smaller patches and presented two basic workflows for this process.

We also presented a showcase model of some meters in size to investigate the scalability of the EGG approach. Furthermore, we analyzed some design challenges that come with these special structures, like the interaction of size and shape, smooth deployment, and the choice of material. Furthermore, we presented a simple and fast fabrication process for the model.

Tab. 3.3: Model dimensions and quantitative results. We measure the root mean square error (*RMSE*) and the maximum error (max. *E*) between the lamellae and the design surface.

	G. Court	Lilium T.	Yas-Hotel
no. patches	4	16	16
size [m]	74×98×7	48×48×37	218×140×47
$w \times t$ [cm]	25×4	50×5	40×5
RMSE [cm]	14.3	24.2	31.8
max. *E* [cm]	49.1	176.1	114.1

3.7.1 Limitations

To validate our geometric results, we used physical simulation to compute the equilibrium shapes of the models presented in Figure 3.17. This was done using the Discrete Elastic Rods model [Bergou et al. 2008; Bergou et al. 2010], with an implementation that features the simulation of self-weight [Vekhter et al. 2019]. Please note, that this model is a standard model in computer graphics, it is fast and delivers good results, which makes it perfect for the early stages of a design process. However, to implement large-scale elastic grids, additional simulations like FEM are needed.

The showcase model we presented is made of two EGG, physically connected along their common lamellae. The simulated grids, displayed in Figure 3.17, are not connected along their common lamellae, which means, there is neither mutual stabilizing nor load transfer between neighboring grids. To connect the grids in the simulation and to study the influence on the overall shape is an interesting topic of its own, which we relate to future work.

In our member strategy (Section 3.4.4) we propagate members using the cladding functions. Please note that T-junctions of boundary members also produce a grid member, that is propagated, as in Figures 3.8 and 3.9. Furthermore, grid members along a ring of patches do not need to close. In Figure 3.17 for surface b) and c) this is the case only because of symmetry.

3.7.2 Conclusion

We demonstrated that the idea of multi-patch EGG is a simple and effective approach to approximate sophisticated design surfaces. The idea of covering the design surface with multiple EGG does not affect the aesthetic or structural qualities of the EGG, in fact, smaller grids are easier to handle and may therefore be more practical. The design surfaces from architecture were split interactively, using the rules presented in this paper, which took some hours each. Automating this process, incorporating certain user goals and aesthetic guidelines, is an interesting topic for future work.

The comparison of the shapes of the showcase model and the small-scale prototype shows satisfying closeness. Some benchmarks for the structural performance of EGG were also presented.

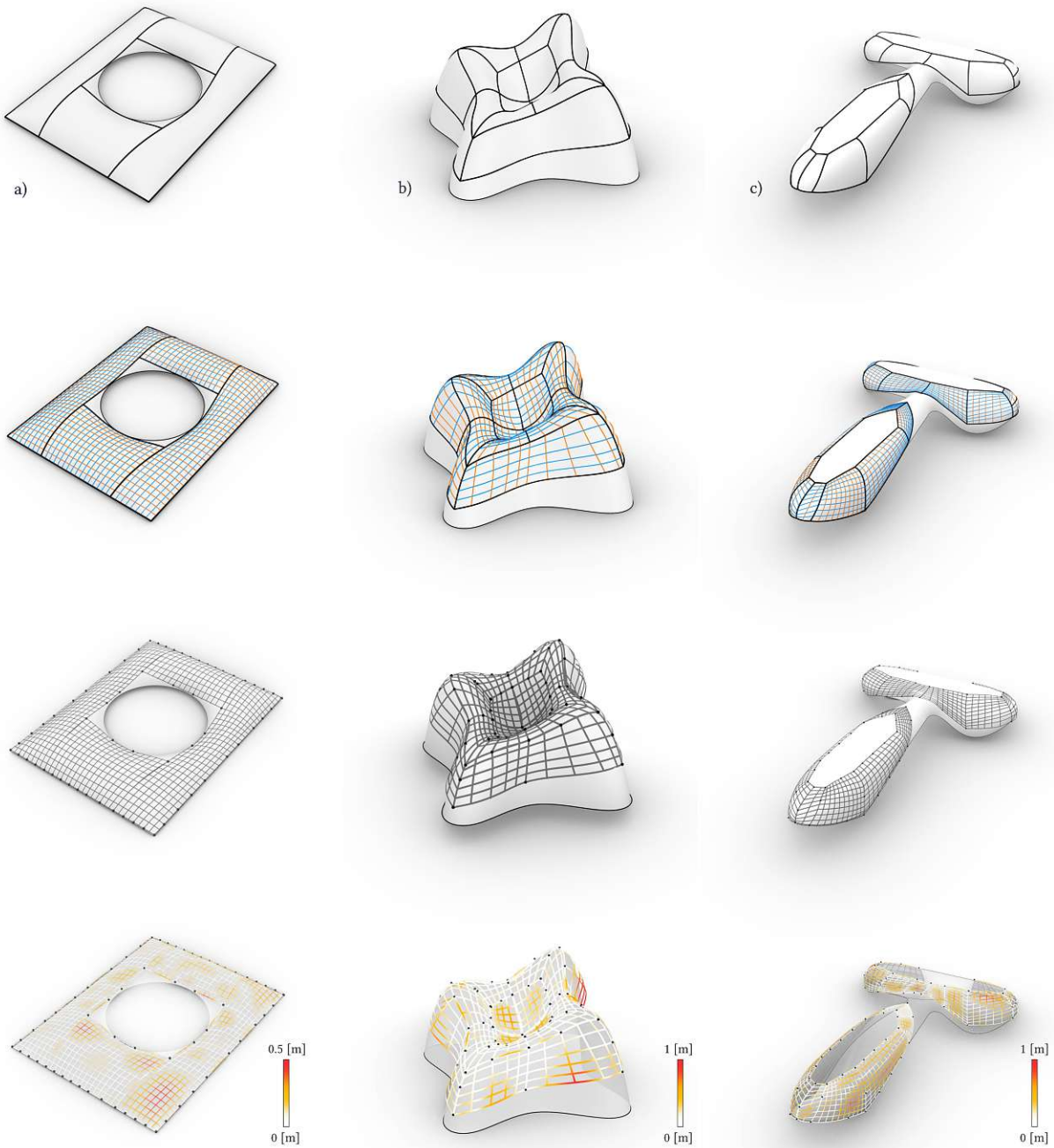

Fig. 3.17: Three multi-patch EGG designs at different stages. The first row shows the boundaries of the patches, the second row shows the geodesic grid members, the third row shows the equilibrium shape of the lamellae and the supports (black dots), and the last row shows a heat-map of deviations of the lamellae from the design surfaces. Columns show a) the Great Court of the British Museum, b) the tip of the Lilium tower, c) the Yas-Hotel. For numeric results, please refer to Table 3.3. Note that the Great Court model is not entirely symmetric, so the distribution of the error is not symmetric either.

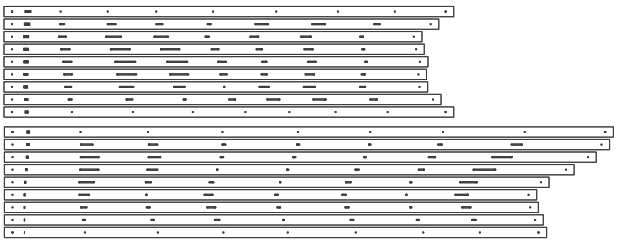

Fig. 3.18: Plan for laser-cutting the lamellae. Scaling by a factor of 9 yields the size of the prototype of Figure 3.1.

We analyzed the implication of increasing the size of the EGG, but the showcase model is only a first step in the direction of reaching architecturally relevant scales. Insights into the interaction of size and shape and the simulation results from architecture models suggest, that larger structures are feasible, especially when using high-performance, high-λ materials.

Acknowledgments

This research was funded by the Vienna Science and Technology Fund (WWTF ICT15-082).

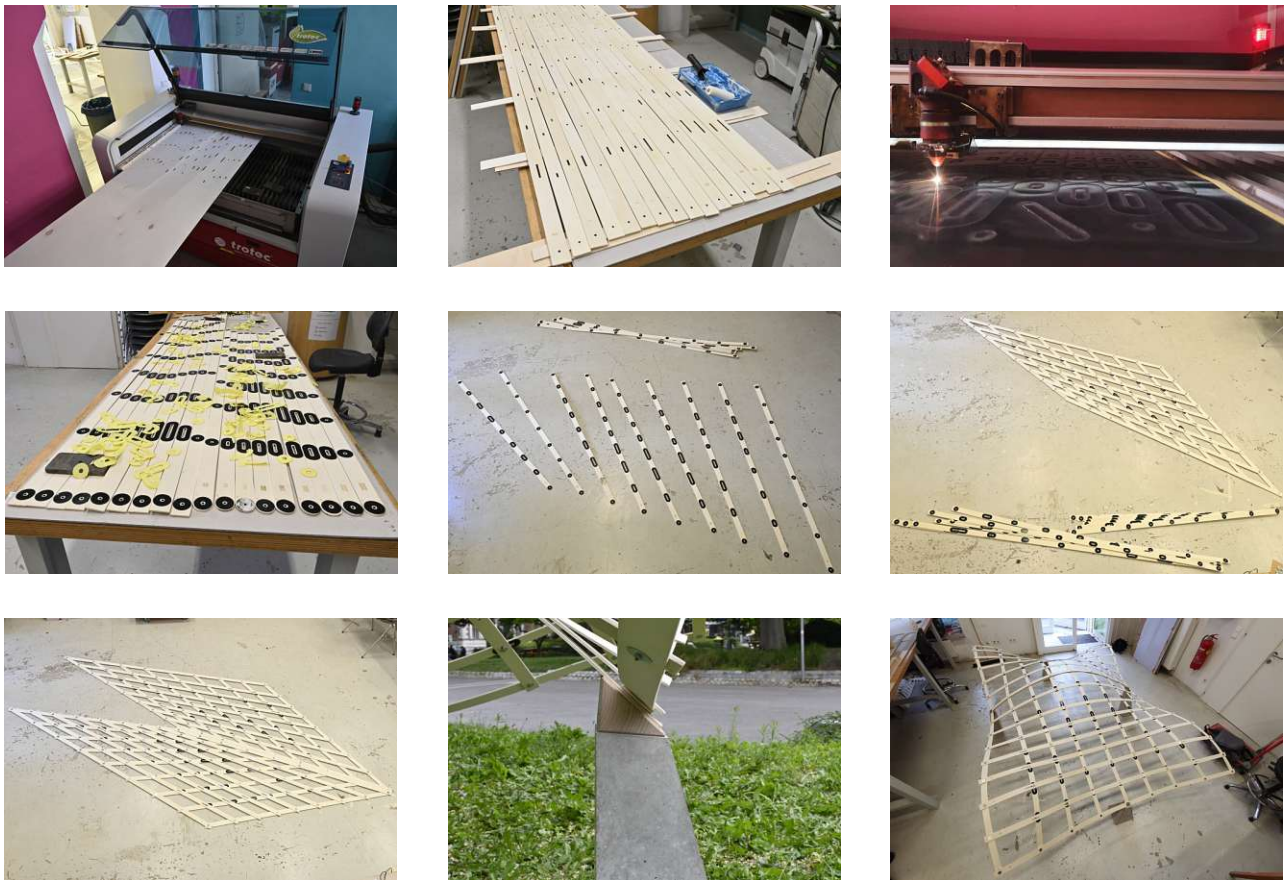

Fig. 3.19: Steps of the fabrication process of the model. A laser-cutter was used to produce the lamellae and the PTFE-stickers. After sticking them to the lamellae, the modules of the grid were assembled. The supports were cast from concrete and have inclined contact areas. Finally, the grid was deployed and fixed to the supports.

Fig. 3.20: Several steps of the deployment of the EGG model and the deployed structure. The deployment process does not require a lot of force, and the curvature of the structure emerges naturally.

Chapter 4

Generalized Deployable Elastic Geodesic Grids

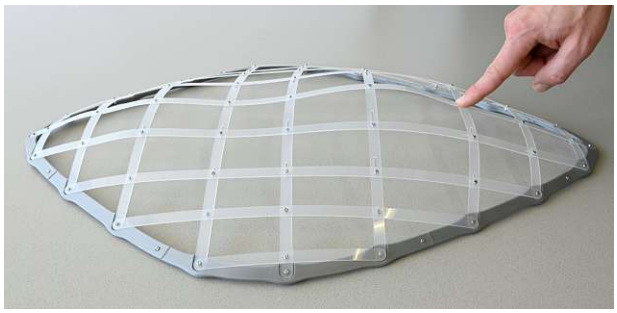

Fig. 4.1: Result of the generalized elastic grid method. An approximation of a doubly-curved surface with elliptic and hyperbolic regions using an elastic geodesic grid, deployed from a perfectly planar state by fixing its boundary elements to an anchor-ring.

Fig. 4.2: A closeup photography of an elastic geodesic grid dome which is also doubly-curved, fixed to 3d printed anchors. Please refer to Figure 4.20 for more examples.

Authors: Stefan Pillwein and Przemyslaw Musialski

Published in: ACM Transactions on Graphics, Vol. 40, No. 6, December 2021

4.1 Introduction

The pursuit of novel structures suitable for design and engineering has been a very old topic in science and engineering. One of the ultimate goals of this race are structures that are light, cheap, and strong.

An interesting class of structures that largely fulfill these requirements surprisingly seems to have contradictory properties: Under load, they leave their stable state and compensate it with buckling. In mechanical terms, they elastically move to the post-buckling regime. Usually, engineers want to avoid any buckling effects as they are regarded as structural failures. On the other hand, by adequately designing the structure's geometry, this seeming disadvantage can be of great practical use with a high level of efficiency. Especially, slender structures like rods, plates, or shells are suitable for design with such elastic bending techniques.

In practice, the post-buckling effect can be observed on a simple igloo tent whose shape is maintained by two poles bent over each other. This construction has many advantages; it is compact, lightweight, and easy to build, but still effective and durable.

In the past, the possibilities for the design of free-form structures were very limited, and the material has almost always imposed the final shape. The design of sophisticated geometric shapes was too complex without advanced computational tools. Nonetheless, the paradigm fascinates and has been applied in many scales and domains: from large-scale architecture [Shukhov 1896], over medium-scale furniture design [Panagoulia et al. 2016], to mesoscale structures in material science [Lavine 2015].

Recently, several approaches for the computational design of deployable elastic structures [Soriano et al. 2019; Panetta et al. 2019; Pillwein et al. 2020b] have been proposed. Nonetheless, while these methods come with excellent results, they suffer from a number of limitations. For instance, Panetta *et al.* [Panetta et al. 2019] introduce elastic gridshells composed of elements with varying cross-sections and allow for varying boundaries, however, their approach does not always ensure the planarity of the 2d configurations.

In contrast, the method of Pillwein *et al.* [Pillwein et al. 2020b] generates perfectly planar 2d layouts, on the downside, their method is limited to scissor-like convex quadrilateral patches only and does not allow free-form boundaries. While more complex shapes are possible by stitching multiple quadrilateral patches together [Pillwein et al. 2020a; Pillwein et al. 2021a], an arbitrary boundary is still not possible.

In this paper, we introduce a new method to deal with arbitrary, even non-convex boundaries. Our method is based on assumptions derived from differential geometry of curves and surfaces, similar to the model of Pillwein *et al.* [Pillwein et al. 2020b] , where the elastic grid follows

geodesic curves on the surface and expects that the lattice members are bendable only along a single axis. While this poses a certain limitation on the surfaces that can be approximated, it still allows exploring a rich space of possible designs with double curvature, especially if the surfaces have non-convex boundaries.

Our model allows us to compute the grids using purely geometric notions with no need for physical simulation, making it computationally very efficient. At the same time, the proposed geometric concepts are well-founded by the theory of minimal energy curves and we can show a very close match of our results to the outcomes of physical simulation performed with the state-of-the-art discrete elastic rods model [Bergou et al. 2008].

Indeed, most of our concepts can be reduced to the computation of geodesic distances on the surface, including intersections of curves, and not even the computationally expensive tracing of the paths of the curves is necessary. Additionally, we extend it fluently to the discrete domain, which allows for efficient updates of the combinatorics of the grids. In particular, the contributions of the paper are the following:

- An elastic grid on the surface should approximate the surface well and capture its characteristics. The task of the choice of proper members is non-trivial and has been solved by Pillwein *et al.* [Pillwein et al. 2020b] using a geometrically driven heuristic. We introduce a well-defined energy functional which allows us to identify so-called *least-effort* and *most-effort* curves on the surface, which ensure to capture the surface characteristics well and provides aesthetic grid layouts.
- More sophisticated surfaces exhibit boundaries which are non-convex (c.f. Fig. 4.3), in fact, they can possess multiple non-convex regions. This implies that the planar configuration becomes more intricate, hosting subfamilies of members, and poses the challenge of varying connectivity grids. We propose an efficient algorithm based on distance computations only that updates the combinatorics of the grids.
- A crucial requirement of deployable structures is that the undeployed state remains perfectly planar. This requirement is important for the ease of fabrication, transportation, and assembly and should not be underestimated—dealing with bent elements is considerably more difficult and more expensive than with planar ones. Therefore, we introduce a generic planarization algorithm that also takes fabrication constraints into account.
- Finally, we introduce a digital fabrication pipeline for the grids and present a number of our results as desktop-size models fabricated from wood or acrylic glass as a proof of concept of our approach.

In the remainder, our paper is organized as follows: In the next section, we review related works, in Section 4.3 we discuss the goals and assumptions of our approach. In Section 4.4 we describe the concepts of the representation of the grids, and in Section 4.5 we discuss the computation of finding grid layouts with non-convex boundaries. In Section 4.6 we describe the background of the elastic energy which we use for finding optimal grids. In Section 4.7 we propose an optimization algorithm for the planarization of spatial grids. Finally, in Section 4.8 we present quantitative and qualitative results, including fabricated models, and in Section 4.9 we discuss the limitations and conclude our work.

4.2 Related Work

Gridshell Structures Structures that gain their strength and stiffness through their curvature have been used in architecture and design since ancient times [Lienhard et al. 2013]. At the end of the 19th century, Shukhov applied the idea for the Rotunda of the Panrussian Exposition [Shukhov 1896], and it was further pursued by famous architects, e.g., by Frei Otto for the construction of the roof of the Multihalle at the Mannheim Bundesgartenschau [Happold et al. 1975].

This form of structure erection has been summarized in the architecture and construction literature as the *active bending* paradigm [Lienhard et al. 2013; Lienhard et al. 2018]. Modern and easy-to-use computational methods increased the interest of the scientific community in systematically utilizing elastic bending to realize curved shapes. Until recent advances in computer science, they could only be form-found empirically [Gengnagel et al. 2013]. Architectural works aim at the approximation of gridshells and combine lightweight structural design with aesthetics [Soriano et al. 2015; Soriano 2017].

Existing design approaches are often based on particular kinds of surface curves, e.g., asymptotic curves [Schling et al. 2018]. Besides their aesthetic qualities, such structures can also be assembled in initially flat segments. They naturally transform to a curved state by their internal forces, however, such curve networks can only be found on surfaces with negative Gaussian curvature.

Deployable Structures Much research is currently being carried out on gridshell-structures that can be deployed. They can be classified based on their deployment mechanism: inscribed in a grid that is deployed [Panetta et al. 2019; Isvoranu et al. 2019; Soriano et al. 2019; Pillwein et al. 2020b] or by other external mechanisms like inflatable air cushions [Quinn et al. 2018; Konaković-Luković et al. 2018]. We are interested in the first case. The design approaches of inscribing the deployment mechanism into the grid, however, differ:

To create an X-Shell [Panetta et al. 2019], a planar grid layout is designed using curved or straight members and actuated via physical simulation. In multiple layout iterations which do not require a target surface, the de-

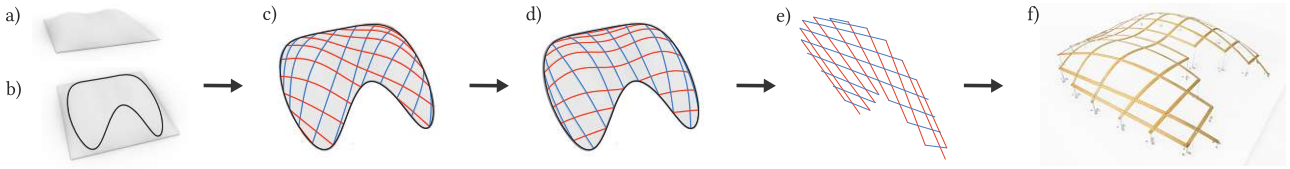

Fig. 4.3: Overview of our modeling pipeline: (a) initial surface, (b) designer chooses a boundary curve on the surface, (c) initial grid (designer provides an arbitrary number of members), (d) grid optimization (we find a grid that nestles to the surface well), (e) planarized grid, (f) fabricated gridshell.

signer finds a satisfactory shape by adapting the planar design. Target surfaces can, however, be approximated using shape optimization (presuming a good planar initialization). The practical feasibility of these structures was investigated with the construction of a pavilion [Isvoranu et al. 2019].

The G-Shells approach [Soriano et al. 2019] proposes to planarize a specific geodesic grid using physical simulation and an evolutionary multi-objective solver. This induces a geometric error, so the flat grid cannot be deployed to match the geodesic grid perfectly but still create beautiful shapes. However, the space of realizable shapes is not fully characterized.

In contrast to the former approaches, elastic geodesic grids [Pillwein et al. 2020b] use the concept of notches, which prevents the geometric error in the grid layout and allows for a very close approximation of a target surface. However, it also makes deployment more complicated as a sliding of members is necessary. The method takes a design surface as input and produces a deployable grid layout without using physical simulation.

Besides elastically bendable structures, there has also been extensive research on various deployable structures and deployment mechanisms methods. One way to easily construct spatial shapes from flat sheets is by appropriately folding paper [Massarwi et al. 2007; Dudte et al. 2016], which is inherently related to the Japanese art of Origami. Also Kirigami, a technique to cut patterns into planar sheets to allow solid faces to rotate about each other, deforming in three dimensions while remaining planar has been explored for deployable surfaces [M. Liu et al. 2020; Jiang et al. 2020a] and recently also bi-stable structures [T. Chen et al. 2021].

Bendable and Stretchable Structures Elastic deformation of surfaces based on variational principles of minimal energy has a long research history in the computer graphics community [Terzopoulos et al. 1987; Welch et al. 1992]. These approaches usually assume that the structure can elastically bend and stretch.

For instance, programmable elastic structures are based on both bending and tensile energy, e.g., by using prestressed latex membranes to actuate planar structures into free-form shapes [Guseinov et al. 2017]. This method has been extended to programmable material sheets composed of mesostructures and membranes to design materials that stretch and bend to evolve to doubly-curved surfaces over time [Guseinov et al. 2020]. Another approach is to combine elastic rods and membranes leading to Kirchhoff-Plateau surfaces that allow easy planar fabrication and deployment [Pérez et al. 2017]. Furthermore, flexible rod networks [Pérez et al. 2015], which additionally allow for controllable elastic deformation of given shapes, have been explored.

A combination of precomputed flexible meso-cells leads to a method where planar configurations can deform to desired shapes if appropriate boundary conditions are applied [Malomo et al. 2018]. This approach has been tested by constructing a pavilion [Laccone et al. 2019] on an architecturally relevant scale.

Another technique, called tensegrity, is to combine elastic and stiff elements to create physically stable structures, which has been recently explored for computational design [Pietroni et al. 2017]. Also recently, a method for the design of kinetic wire characters has been proposed [Xu et al. 2018], where custom springs are introduced to adapt the stiffness of the wires.

In fact, much attention has been paid to the design of doubly-curved surfaces, which can be deployed from planar configurations due to the ease of fabrication. One way of achieving this goal is by using auxetic materials [Konaković et al. 2016] which can nestle to doubly-curved spatial objects, or in combination with appropriate actuation techniques, can be used to construct complex spatial objects [Konaković-Luković et al. 2018].

Surface-based inflatable structures [Panetta et al. 2021] utilize expanding tunnels fabricated by fusing two layers of thin material to approximate surfaces. Layouts are found by including the bending energy stored in the tunnels using the shape operator, a method that is closely related to how we express the energy of lamellae.

Bendable Non-Stretchable Structures In contrast to methods that allow bending and stretching, our approach assumes that the elastic elements can bend and twist but not stretch and must therefore maintain the same length in the planar and spatial configuration.

Mappings of geodesic nets on a surface onto geodesic nets on a different surface (including the plane) were a topic of classic differential geometry [Voss 1907; Lagally 1910]. It has been shown that arc-length preserving mappings of continuous geodesic nets onto each other require

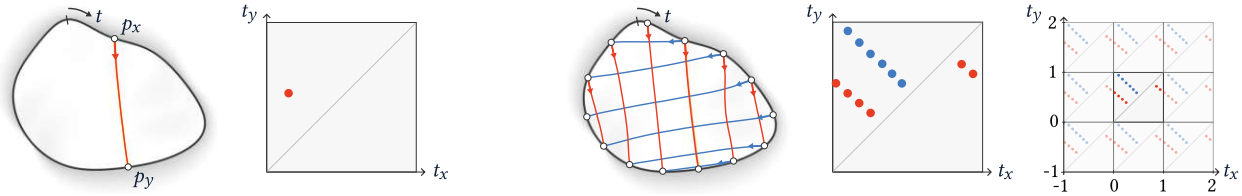

Fig. 4.4: Our concept of grid representation in the dual space. We parameterize the boundary with constant speed, $t \in [0, 1)$, and represent geodesics by the t-values of the endpoints. Left: The geodesic between $p_x = p(t_x)$, $p_y = p(t_y)$ corresponds to a single point in the dual space, the direction $t_x \rightarrow t_y$ is also encoded. Right: Two families of geodesics are represented in the dual space, spacing and directions of members define two sequences of points. If we extend the parameterization of the boundary to $(-\infty, \infty)$, the representation in the dual space is extended periodically.

rhombic geodesic nets, i.e., need a parameterization of the surface with the net curves as parameter curves and $E = G$ in the fundamental form. The resulting Liouville surfaces are very limited in shapes, and therefore not useful for our free-form design purpose.

A lot of attention has been paid to the approximation of free-form surfaces using developable surfaces [Pottmann et al. 2010] which can be fabricated from 2d flat elements by cutting. By bending and combining 2d elements, complex free-form surfaces can be erected. On the theoretical side, a novel representation of developable surfaces using quadrilateral meshes with appropriate angle constraints [Rabinovich et al. 2018a] or a definition of developability for triangle meshes [Stein et al. 2018] have been proposed recently. Also, optimal piecewise wrapping of doubly-curved surfaces with developable patches has been explored [Ion et al. 2020].

Other works deal with curved folds and efficient actuation of spatial objects from flat sheets [Kilian et al. 2008; Kilian et al. 2017a]. Discrete geodesic parallel coordinates have been introduced for modeling of developable surfaces [H. Wang et al. 2019]. Another related work combines the idea of elastic bending and weaving. This allows for creating physically governed surfaces woven out of foliations whose leaves approximate geodesic curves [Vekhter et al. 2019].

Also related to our work are approximations of surfaces based on Chebyshev nets [Garg et al. 2014], which have been further analyzed for their elastic characteristics [Baek et al. 2018]. Recently this method has also been used for the simulation of hemispherical elastic gridshells [Baek et al. 2019].

Introducing elements with variable stiffness furthermore enables a wide range of target equilibrium shapes. This space was recently rigorously characterized [Hafner et al. 2021] for elements that are only constrained at their boundaries, using a method to determine physically viable shapes by visual inspection. To find viable grid layouts, we face a similar task and build upon these insights.

4.3 Goals and Assumptions

4.3.1 Objectives

Our goal is to find geodesic grids on given free-form surfaces such that they can be realized as physical grids composed of slender physical elements, such as rods or strips, where the ratio of the cross-sections of the elements is about 1:10 with a distinct weak axis. In our experimental models, we use thin lamellae laser-cut from wooden panels or acrylic glass plates.

The grids can be deployed from 2d planar states to surfaces in 3d space by compressing and fixing the outer boundary of the planar state. The intuition is that hence the geodesic distance between the ends of the incompressible elements is longer than the distance between the ends in the embedding space, they will undergo buckling and take a shape that minimizes the bending energy along their length. Due to the global interaction of the members, properly connected at their intersections, a spatial structure emerges.

The input surfaces are allowed to have general boundary curves, which can even be non-convex (cf. Fig 4.3), such that various configurations are possible. The grids are erected by fixing the free ends of the planar elements to given anchors distributed along a boundary curve. This provides the constraints necessary to adopt the desired minimal potential energy state. Note that anchors provide both the positions (function values) and the tangent planes (first-order derivatives) at the boundary points of the grid, but the tangent directions are not fixed (refer to Figures 4.20 and 4.21).

4.3.2 Assumptions and Simplifications

We minimize the error between the given target surface and the geodesic grid implicitly by assuming that the lamellae will behave very closely to geodesic curves on the target surface. This assumption is based on the fact that a geodesic curve has zero geodesic curvature κ_g and exhibits only normal curvature κ_n, which is further discussed in Section 4.6.

The intuition behind this assumption is that we can "glue" a thin strip along its centerline along such a curve

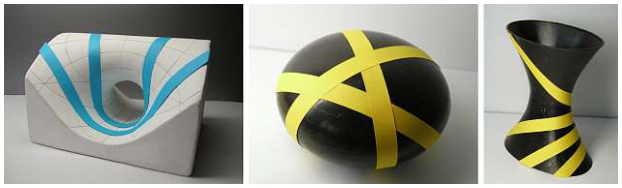

Fig. 4.5: Examples of paper strips "glued" to the surfaces. The centerlines of the strips follow geodesic curves on each surface. A sufficiently small strip can follow any geodesic on a surface but only a subset of all possible geodesics on a surface are suitable for elastic geodesic grids.

on the surface and their lengths will match (cf. Figure 4.5). A sufficiently small strip can follow any geodesic on the surface, however, if the strip itself is elastic and resists bending, only a subset of all possible geodesics on the surface are suitable for elastic geodesic grids. Thus, our major goal in this paper is to find such grids to approximate the surfaces efficiently.

Another simplification is that since our computations are based purely on geometry, we do not take any physical quantities, like gravity or friction, into account. Our model also assumes perfectly geometrically non-linearly bendable materials, and we do not account for any material failure if the elastic region is left, resulting in severe structural failure. We do so since our model is meant for rapid form-finding and the generation of prototypes, however, such engineering constraints could be added easily on top of our model, if necessary.

4.3.3 Representable Surfaces

The uniqueness of shortest geodesics is connected to the Gaussian curvature K of the surface. Figuratively speaking, if a region of the surface has very high K, shortest geodesics will go around it and cease to be unique, which we need to prevent. Pillwein *et al.* [Pillwein et al. 2020b] investigated this problem and proposed an iterative smoothing procedure until the shortest geodesics between points on the boundary of a surface are unique. We use the same procedure, please refer to the paper for details.

A stable grid on a surface with positive and negative K requires geodesics between all regions of positive K which are physically viable, i.e., the equilibrium shapes of the corresponding lamellae need to be close to the surface. If the input surface has no inner bumps (extrema of K far from the boundary), we can be pretty optimistic about finding a suitable grid. If there are inner bumps, finding a grid that remains stable in the desired shape may be challenging. A sufficient but not necessary condition is based on the mean curvature $H > 0$, which restricts the surfaces to the ones that can be achieved by inflating a balloon, i.e., excludes bumps that point inward [Konaković-Luković et al. 2018].

However, this condition is too strict for our purposes, as we discuss in Section 4.6 and show in our results in Section 4.8, because it does not account for the interaction of grid members, which stabilize each other.

4.4 Grid Representation

This section describes the details of our implementation, grid representation, parameterization, and discretization. For the readers convenience, we first summarize the notation further used in the paper:

- $S\colon \mathbb{R}^2 \to \mathbb{R}^3$ with $(u, v) \mapsto S(u, v)$ is the input surface.
- $p(t) \subset S$ is the closed boundary curve.
- t is the unit speed curve parameter, w.l.o.g., $t \in [0, 1)$.
- $c(t_x, t_y) = c(p_x, p_y) \subset S$ represents the shortest curve connecting $p_x = p(t_x)$ and $p_y = p(t_y)$.
- $d(p_x, p_y) = d(c(t_x, t_y)) \in \mathbb{R}_+$ denotes the distance between two points on the boundary.
- $g = \{c_1, \dots c_n\}$ and $h = \{c_1, \dots c_m\}$ are the families of curves of a grid; we order the elements by an increasing value of t_x.

4.4.1 Input and Output

The input to our system is a surface patch which is defined by a closed unit length boundary curve $p(t) \subset S$ on a surface $S \subset \mathbb{R}^3$. The curve is parameterized by the parameter t w.l.o.g. in the interval $t \in [0, 1)$. Both the surface S and the curve p are designer-provided.

If the input surface is represented in parametric form (e.g., NURBS), it is tessellated to a polygonal mesh with sufficient resolution. Further on, our system works with triangular meshes. For several operations, we resort to a parameterization of the surface $S\colon \mathbb{R}^2 \to \mathbb{R}^3$, hence we expect the mesh to be well-parameterized. We propose either utilizing the existing parameterization or employing other parameterization algorithms (e.g., least squares conformal mapping [Lévy et al. 2002]).

The output of our system is a planar grid composed of two families of lines denoted as g and h that cross each other. In the case of a non-convex boundary, any of the families can be further split into one or more groups, forming subfamilies; nevertheless, the grid pattern is always maintained, i.e., at each intersection exactly two members

Fig. 4.6: Two families of grid members, their parameterization and order in the grid. By ordering the members in ascending order of their "footpoints", we can ensure a consistent pointing direction of members, even if they move along the boundary.

of either family cross each other. Please refer to Figures 4.6 and 4.11 for a depiction.

During the deployment, all free ends of the planar grid are fixed to the anchors, which provide them their location in space as well as their tangent planes. The tangent directions are enforced by the overall equilibrium state of the deployed grid. Note that additional constraints, like tangent directions on the free ends, could be prescribed to increase the structure's stability.

4.4.2 Grid Parameterization

We represent the geodesic grid by defining pairs of points $p_x = p(t_x)$, $p_y = p(t_y)$ on the boundary curve which connect to curves $c_i(t_x, t_y) = c_i(p_x, p_y)$. These curves represent the grid members and are organized in two families $g = \{c_1, \dots c_n\}$ and $h = \{c_1, \dots c_m\}$ such that members of one family can intersect the members of the other family as depicted in Figure 4.6. We order the elements of each family by an increasing value of t_x, which ensures that their pointing direction in a grid is consistent; in other words, it ensures that p_x has a lower t-value than p_y, i.e., $t_x < t_y$.

This parameterization allows us to express curves $c(t_x, t_y)$ which connect p_x and p_y on the boundary as points in a 2d dual space. Since the boundary curve $p(t)$ is closed, the mapping is a symmetry group, such that for any function f, the following holds:

$$f(t_x, t_y) = f(T(t_x, t_y))$$

with

$$T(x, y) = \begin{bmatrix} 0 & 1 \\ 1 & 0 \end{bmatrix} \begin{bmatrix} x \\ y \end{bmatrix} + \begin{bmatrix} d \\ d \end{bmatrix}, \quad \forall\, x, y \in \mathbb{R}, d \in \mathbb{Z}\,.$$

Note that values $f(t_x, t_y)$ are translation and reflection-symmetric w.r.t. the affine transformation T, i.e., move along the borders in a periodic fashion and mirror across the diagonal. Points on the diagonal (i.e., $t_x = t_y$) represent infinitely short curves, i.e., points on the boundary. We confine the dual space by $[0, 1) \times [0, 1)$, with the symmetry given by T, please refer to Figure 4.4 for a depiction.

4.5 Grid Layout and Non-Convex Boundary

In this section, we discuss the geometric approach to finding appropriate grid combinatorics, which is purely based on considering (geodesic) distances of points on surfaces.

4.5.1 Distance Fields and Distance Map

While there are many efficient algorithms for computing geodesic distances [Crane et al. 2020], tracing the path

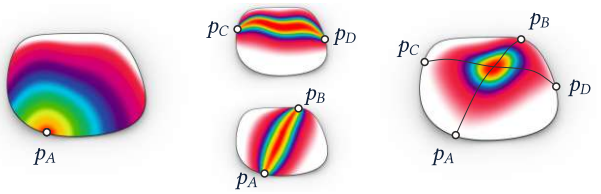

Fig. 4.7: We use distance fields to compute the intersection of two geodesics. Left: A distance field originating from p_A. Middle: When superimposing distance fields from p_A, p_B and p_C, p_D, the paths of the geodesics can be recognized. Right: We recover the intersection of the geodesics by superimposing the distance fields and finding the minimum.

of a shortest geodesic is computationally much more expensive, requiring backtracing, variational shortening of curves, or other methods.

Hence, we utilize the concept of distance maps [Pillwein et al. 2020b], which can be computed and stored efficiently. Distances from all points p_x on the boundary to all other points p_y on the boundary establish the distance map

$$D\colon (t_x, t_y) \to \mathbb{R}_+ \quad \text{with} \quad (t_x, t_y) \mapsto d(p_x, p_y)$$

where

$$d(p_x, p_y) = d(c(t_x, t_y)) = \int_c \|\mathbf{c}'(s)\|\, \mathrm{d}s \in \mathbb{R}_+$$

denotes the geodesic distance (i.e., the arc length) between two points p_x and p_y on the boundary curve w.r.t. the metric of the surface S. Since the boundary is closed, the distance map is defined over the dual space and is also subject to the same symmetry group.

In our implementation, the distance map is sampled on the boundary of the input surface mesh, and the resolution of the mesh gives its resolution. In practice, it is around 60×60 vertices. Since the surface is not altered, distances are stored in a matrix D and reused for many further computations, e.g., to detect non-convex parts of the boundary (Section 4.5.3). Any algorithm that determines geodesic distances accurately is suitable for our method, we use the algorithm proposed by Qin *et al.* [Qin et al. 2016].

4.5.2 Intersections of Geodesic Curves

In our approach, geodesic paths are not explicitly computed, but we need to compute the intersections of members $\in g$ with other members $\in h$. We thus rephrase the problem of computing geodesic paths to computing intersections, using the link between shortest geodesics and distance fields.

A shortest geodesic between points p_A and p_B is defined by two distance fields, i.e., scalar fields of geodesic distances between the source points and all other points on the surface. Summing up the distance fields and tracing the isoline with the value $d(p_A, p_B)$ of the resulting distance field yields the connecting geodesic. Introducing

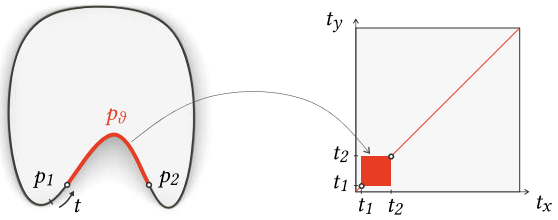

Fig. 4.8: Left: Non-geodesic shortest connections. We identify segments of the boundary that are non-convex using Equation (4.3). Right: All shortest connections along the red, non-convex segment of the boundary constitute a square in the dual space ($p_1 = p(t_1)$, $p_2 = p(t_2)$). These curves are considered invalid for grid members.

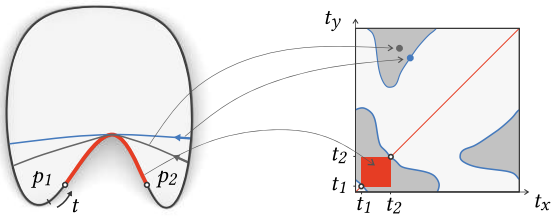

Fig. 4.9: Left: Invalid members. The blue curve is tangential to the non-convex segment on the boundary, and the gray curve shares a part of it. Right: The blue curves emerge in the dual space on the boundary of the gray regions. Curves in these regions are considered invalid and cannot be used as grid members. All such regions are detected using geodesic distances only.

an arbitrary third point $p = S(u, v)$ on the surface, we can state:

$$d(p_A, p) + d(p, p_B) \geq d(p_A, p_B)\,, \tag{4.1}$$

which is based on the triangle inequality of the surface metric. Expression (4.1) is an equality if and only if p is on the geodesic connecting p_A and p_B.

We now consider a second member between points p_C and p_D that intersects the first one. As above, we can state:

$$d(p_C, p) + d(p, p_D) \geq d(p_C, p_D)\,. \tag{4.2}$$

Adding the distance fields emanating from p_A, p_B, p_C and p_D, the minimum of the resulting scalar field takes the value

$$d_{\min} = d(p_A, p_B) + d(p_C, p_D)\,.$$

Considering Expressions (4.1) and (4.2), this can only be the case if both inequalities become equalities and therefore the location of d_{min} is a point on both shortest geodesics, i.e., the point of intersection.

In practice, we need to find the intersections on a mesh, where the distance fields are vectors that hold geodesic distances for all vertices. For every intersection, we first linearly interpolate the distance fields for the current t-values, superimpose them and find the minimum. Thus, the respective vertex is already close to the actual intersection of the geodesics. In a subsequent step, the result gets refined using second-order interpolation. To this end, we use the (u, v)-coordinates of the surface mesh parameterization of the vertex ring around the initial vertex, apply the values of the superimposed distance fields on a third axis, and fit a paraboloid. The (u, v)-coordinates of the minimum correspond to a point, which is sufficiently close to the real intersection of the two geodesics.

We reassemble the grid members using the appropriate intersections and increase their resolution by introducing extra points by linear interpolation between (u, v)-coordinates of adjacent intersections for sparse grids.

4.5.3 Non-Convex Boundaries

Non-convex boundaries introduce curves $c(p_x, p_y)$ on the surface S that minimize $d(p_x, p_y)$, however, are not shortest geodesics due to their non-vanishing geodesic curvature κ_g. Hence, we denote these curves as *shortest connections*. Figure 4.8 depicts a shortest connection between the points p_1 and p_2 which runs along the boundary. We premise that the shape of the surface outside the boundary is unknown, i.e., a shortest geodesic between p_1 and p_2 cannot be found.

We call the boundary of a surface *convex* if there are no *shortest connections* that are tangential to the boundary, otherwise, we call it *non-convex*. In the latter case, the parts of the boundary that make it non-convex need to be found. In Figure 4.8, the lower bay of the boundary is such a non-convex part.

Formally we identify non-convex boundaries by checking the following criterion:

$$d(p_x, p_y) - d_b(p_x, p_y) = 0\,, \tag{4.3}$$

where $d(p_x, p_y)$ is the shortest distance between p_x, p_y on the surface and $d_b(p_x, p_y)$ is their distance measured along the boundary. If there is a combination of p_x, p_y (with $t_x \neq t_y$) and Equation (4.3) is fulfilled, the boundary is non-convex and $c(p_x, p_y)$ leads entirely along the boundary. The part of the boundary that causes the non-convex behavior is formed by the points $p_\vartheta = p(t_\vartheta)$ with $t_1 \leq t_\vartheta \leq t_2$, where t_1 and t_2 are the smallest and largest t-values fulfilling Equation (4.3), respectively. In the dual space, such parts of the boundary appear as squares, please refer to Figure 4.8 for a depiction.

If the boundary is non-convex, in a second step, we need to find all shortest connections $c(t_x, t_y)$ that lead partly along the boundary and exclude them from the set of valid grid members. This is important as, due to our initial assumption (cf. Section 4.3), only lamellae based on geodesics ($\kappa_g = 0$) will bend properly to approximate the surface. Please refer to Figure 4.9, where invalid regions are depicted in the dual space.

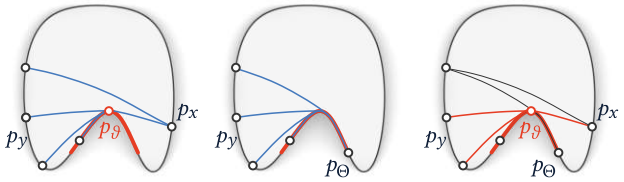

Fig. 4.10: To identify all shortest connections emanating from p_x to p_y that go partially along the boundary, we proceed as follows: Left: We compute the distances $d(p_x, p_y)$. Middle: From p_x, we jump to the closest point p_Θ of the non-convex segment and compute the distances $d(p_\Theta, p_y)$. Right: If shortest connections from p_x to p_y and p_Θ to p_y have more than one common point, the shortest connection $c(t_x, t_y)$ is invalid.

To this end, we check the shortest connections from one fixed point p_x to all other points p_y on the boundary at a time. The resulting curves span a fan of shortest connections emanating from p_x (cf. Figure 4.10). We introduce a second fan emanating from p_Θ with the same destinations p_y. The point p_Θ is the point of p_ϑ which is closest to p_x, measured along the boundary. We find all shortest connections that are no shortest geodesics by computing:

$$d_g(t_x, t_y) = d(p_x, p_y) - d(p_\Theta, p_y)\,, \tag{4.4}$$

and checking

$$\frac{\partial d_g}{\partial t_y} = 0\,. \tag{4.5}$$

Equation (4.5) is a necessary condition to find invalid connections $c(t_x, t_y)$ along the boundary. If $c(t_x, t_y)$ touches the boundary, we refer to the first point of contact as $p_\vartheta = p(t_\vartheta)$. Assuming such a curve, we rewrite Equation (4.4):

$$d_g(t_x, t_y) = d(p_x, p_\vartheta) + d(p_\vartheta, p_y) - d(p_\Theta, p_\vartheta) - d(p_\vartheta, p_y)\,,$$
$$d_g(t_x, t_y) = d(p_x, p_\vartheta) - d(p_\Theta, p_\vartheta)\,,$$

$\partial d_g / \partial t_y$ does indeed not depend on t_y and vanishes. Equation (4.5) is not sufficient as there may be special cases where $d_g(t_x, t_y)$ remains constant w.r.t. changes in p_y without boundary contact. We have not encountered such cases in our models but can exclude them as they would appear as noise or isolated islands in the dual space, not connected to a non-convex segment (red square in Figure 4.8). Figure 4.10 helps to interpret Expression (4.4): The difference $d_g(t_x, t_y)$ can be reduced to $d(p_x, p_\vartheta) - d(p_\Theta, p_\vartheta)$, if the shortest connections from the fan of p_x touch the boundary.

The set of invalid connections delivers in the dual space a map of connected regions that must be avoided in order to find valid geodesic grids.

4.5.4 Solution in the Discrete Domain

For the computation of invalid regions, we resort to the discrete domain $\mathbb{N}$ and introduce a mapping z which maps all t-values to integer coordinates of the mesh boundary:

$$z\colon t \in [0, 1) \mapsto i \in [1, \ldots, N]\,,$$

where N is the mesh boundary resolution. We denote the coordinates of the curves in the discrete space as $c(i_x, i_y) = c(z(t_x), z(t_y))$, where $i_x, i_y \in [1, \ldots, N]$ represent their counterparts $t_x, t_y \in [0, 1)$ from the continuous domain. Note that $N + 1 = 1$ and $c(i_x, i_y) = c(i_y, i_x)$, respecting the symmetry given by T.

To initially find non-convex regions we compute Equation (4.3) on the mesh. We reuse the distance fields and perform:

$$D - B < \epsilon\,, \tag{4.6}$$

where D and B are NxN matrices, D is the distance map $D(i_x, i_y) = d(p(i_x), p(i_y))$, B holds the distances measured along the boundary, $B(i_x, i_y) = d_b(p(i_x), p(i_y))$, and ϵ is a small constant close to zero. The distances $d(p_x, p_y)$ and $d(p_\Theta, p_y)$ in Equation (4.4) are a subset of the distances from the precomputed distance fields, the partial derivative w.r.t. t_y becomes a difference of $d_g(i_x, i_y)$, w.r.t. i_y.

Now we can formulate the search for invalid regions using a region growing approach as in image processing. We know the core regions from the difference in Expression (4.6), so we grow them along respective i_x and i_y coordinates as

$$c(i_x, i_y) = c(i_x + s_{i_x}, i_y)$$
$$c(i_x, i_y) = c(i_x, i_y + s_{i_y})$$

where s_{i_x} and s_{i_y} are steps that are either +1 or −1 depending on which half-space of the dual space the points are located. During this movement, distance checks as in Equation (4.4) are performed by looking up distance values in the distance map $D(i_x, i_y)$. Performing the procedure until convergence yields masks that contain invalid regions.

During the optimization of grids (cf. Section 4.6.4), grid members need to be found frequently, and the combinatorics of the grid has to change in order to produce valid grid members. We use the dual space and its invalid regions, identified using Equation (4.5), to correct layouts efficiently. Figure 4.11 depicts how invalid members are detected and the subsequent adjustment of a layout. In cases where a member arrives in an invalid region, the respective member family (g or h) is split into two along their respective i_x and i_y coordinates in the dual space, and all following members are shifted out until the invalid-region condition as well as grid consistency constraints, which maintain the order of elements, are fulfilled.

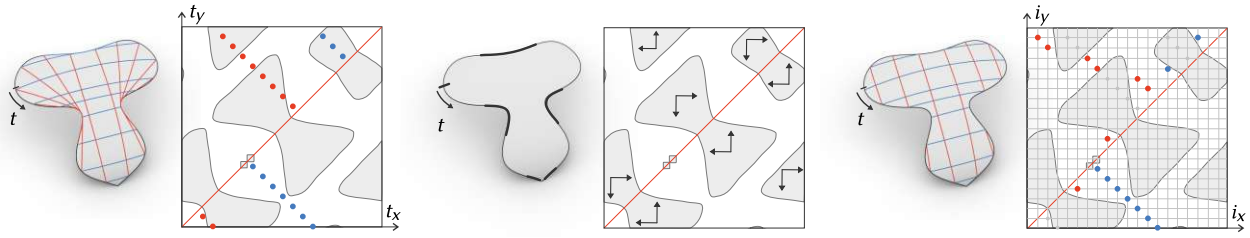

Fig. 4.11: Layout correction algorithm. Left: An invalid grid, members appear as points in the dual space. Middle: For every invalid region in the dual space, there are fixed shifting directions that govern the adjustment of layouts. Right: Members shifted out of invalid regions to the next feasible combination in the discrete dual space $z\colon (t_x, t_y) \mapsto (i_x, i_y)$. Note, it only changes the combinatorics of the grid but leaves the endpoint locations unchanged. The small square-shaped regions in the dual space correspond to two small, almost straight, non-convex segments of the boundary at the lower tip of the surface. Please recall that the dual space and the invalid regions are periodic, as depicted in Figure 4.4.

This algorithm can be implemented very efficiently in the discrete domain, where look-ups in the precomputed distance map and invalid-region maps are performed.

4.6 Elastic Geodesic Grid Energy

In this section, we describe the mathematical model of our approach, based on insights from differential geometry and variational principles, and derive the necessary energy functionals which constitute our elastic geodesic grids.

The main aspect of our work is finding networks of intersecting curves that nestle to the surface when boundary conditions are enforced, i.e., when grids are fixed to anchors. However, not all such grids will both nestle to the surface well and additionally also closely capture the surface's features, like local extrema of K. Figure 4.12 shows two different geodesic grids and their respective equilibrium shapes when boundary conditions are enforced. As evident, some grids are better suitable than others and their choice obviously depends on local surface features.

4.6.1 Elastic Geodesic Curves

The internal bending energy of an arc length parameterized curve $c := \boldsymbol{c}(s)$ of length l can be formulated using the Elastica energy:

$$E_b = \int_0^l \kappa^2 \, \mathrm{d}s \,, \tag{4.7}$$

where $\kappa = \|\boldsymbol{c}''(s)\|$ is its curvature, i.e., the length of the curvature vector.

We can use this energy to approximate the bending behavior of the centerlines of slender wooden lamellae quite accurately. This assumption is not entirely true in theory for non-stretchable, perfectly developable strips, which indeed need to maintain the same length of the centerline as well as of the edges.

Nonetheless, wooden lamellae are not perfectly developable, and hence their behavior is more similar to the bi-normal strips [Wallner et al. 2010], where the ratio of the lengths of the center curve and the edges varies slightly if they are bent and twisted (i.e., the strip stretches or compresses slightly). However, the deviation is negligible if the width to length ratio of the strip is small, as in our case. This assumption is also common in physical models, like discrete elastic rods [Bergou et al. 2008], which allow for the simulation of slender rods with varying cross-sectional ratios. For these reasons, we choose to approximate the strips with their center lines.

For curves $c(s)$ which lie on a surface S, their curvature vector $\boldsymbol{c''}$ can be decomposed into its normal curvature component κ_n and geodesic curvature component κ_g, such that it is given by

$$\boldsymbol{c}'' = \kappa_n \boldsymbol{n}_S + \kappa_g \boldsymbol{b}_c \,,$$

where $\boldsymbol{n}_S$ is the surface unit normal and $\boldsymbol{b}_c$ is a unit vector in the tangent plane, orthogonal to the curve tangent. This dependency can also be expressed by the Pythagorean theorem as:

$$\kappa^2 = \kappa_n^2 + \kappa_g^2 \,.$$

As per definition (cf. Section 4.3), geodesic curves have vanishing geodesic curvature, i.e., $\kappa_g = 0$, the curve's normal is aligned with the surface normal $\boldsymbol{n}_S$. Since we

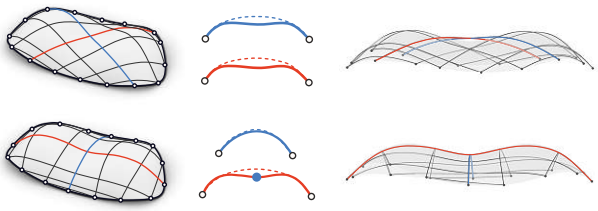

Fig. 4.12: Left: Two different grid layouts on the same surface. Middle (top): The blue and red geodesics are prone to relax to different shapes. Middle (bottom): The red geodesic is constrained by the blue one. Right: Physical simulation of the grids, only the lower grid nestles to the surface well.

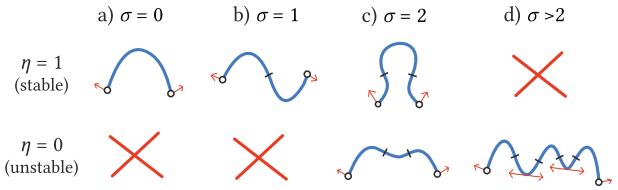

Fig. 4.13: We estimate the shape stability of geodesics using the shape stability parameter η, which depends on the number σ of inflection points w.r.t. the normal curvature κ_n. We expect that all curves of type d) need additional support from crossing members. Curves of type c) are a limit case and are assessed using the criterion of [Hafner et al. 2021].

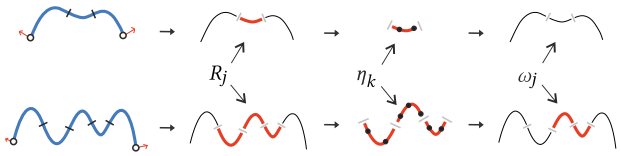

Fig. 4.14: We account for mutual stabilization effects by dividing the curve into segments R_j needing support and checking if they are stabilized by crossing members (black dots), taking into account their shape stability η_k. Top: The central region of the curve is stabilized, $\eta = 1$. Bottom: Only one of three curve segments is stabilized, we expect poor performance, $\eta = 1/3$.

allow only geodesic curves on S, the bending energy in Equation (4.7) reduces to

$$E_b = \int_0^l \kappa_n^2 \, \mathrm{d}s \,. \tag{4.8}$$

We can further rewrite κ_n using Euler's theorem as

$$\kappa_n = \kappa_1 \cos^2 \varphi + \kappa_2 \sin^2 \varphi \,,$$

where κ_1, κ_2 are the principal curvatures at the given surface location, and φ is the angle between the curve's tangent vector $\boldsymbol{t}_c$ and the principal curvature direction $\boldsymbol{v}_1$. Assuming a unit $\boldsymbol{t}_c$, it can also be expressed in the surface's local frame spanned by the principal curvature directions $\boldsymbol{v}_1, \boldsymbol{v}_2$ in terms of inner products as

$$\kappa_n = (\kappa_1 - \kappa_2)\langle \boldsymbol{t}_c, \boldsymbol{v}_1 \rangle^2 + \kappa_2 \,.$$

To evaluate κ_n at vertices $q(u,v)$ of grid members, we approximate $\boldsymbol{t}_c$ using the normalized mean of their adjacent edges and linearly interpolate values of κ_1, κ_2, and $\boldsymbol{v}_1$ for the respective (u,v)-coordinates.

4.6.2 Shape Stability

The shape of a physical grid depends on several factors, like the bending energy of grid members and mutual stabilization. To ensure a close approximation of the target surface but avoid costly physical simulation, we introduce an energy that estimates how closely a grid will preserve its initial shape when boundary conditions are enforced. To define this energy, we first analyze the quality of members individually, then account for mutual stabilization of members, and finally obtain a single scalar value E_{shape} ranging between 0 and 1. The lower its value, the larger the deviation from the target surface can be expected.

We initially assess the quality of grid members individually by means of the number σ of inflection points of each member w.r.t. the normal curvature κ_n. We consider members with $\sigma < 2$ as stable and members with $\sigma > 2$ as unstable, please refer to Figure 4.13 for a depiction. To classify members with $\sigma = 2$, we use a stability criterion for planar curves [Hafner et al. 2021] (neglecting the torsion of grid members). We subsequently classify each curve with a shape stability parameter $\eta = 0$ or $\eta = 1$.

The interaction of elastic members in a grid is highly complex, however, we want to take into account mutual stabilization effects for unstable members ($\eta = 0$). To this end, we divide them into $(\sigma - 1)$ curve segments R_j needing external support, which are separated by the inflection points (cf. Figure 4.14). For each segment j, we check for stable crossing members and assign a stability weight ω_j:

$$\omega_j = \begin{cases} 0 & \text{if} \quad \sum_{k=1}^{n+m} B(\eta_k \in R_j)\eta_k \geq 1 \,, \\ 1 & \text{if} \quad \sum_{k=1}^{n+m} B(\eta_k \in R_j)\eta_k = 0 \,, \end{cases}$$

where $B(\cdot) \rightarrow \{0,1\}$ is a Boolean operator which ensures that only η of crossing members intersecting in the respective curve segment are summed up, and k iterates over all members. If one or more curves with $\eta = 1$ cross in a segment needing support, it is considered as stabilized, and $\omega_j = 1$, otherwise $\omega_j = 0$. We subsequently update η of all unstable members by the arithmetic mean of their ω-values:

$$\eta = \frac{1}{\sigma - 1} \sum_{j=1}^{\sigma-1} \omega_j \,,$$

and finally assess the shape quality of the whole grid by taking the shape stability parameters of all members into account:

$$E_{\text{shape}} = \frac{1}{n+m} \sum_{k=1}^{n+m} \eta_k \,. \tag{4.9}$$

Figure 4.15 shows a failure example with a ripple-like target surface. The grid reaches a low shape stability ($E_{\text{shape}} = 0.45$) which indicates that we can expect a poor approximation of the surface.

4.6.3 Least and Most Effort Energy

Our goal is to approximate arbitrary representable surfaces, hence we need an energy functional that allows us to capture the surface characteristics well. To ensure this, we define two types of curves, which must be present in a grid.

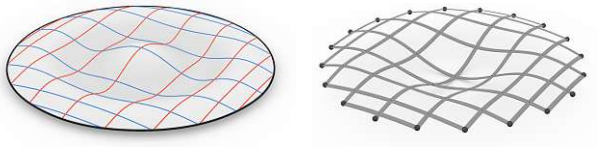

Fig. 4.15: Failure case. Left: A desired shape and geodesic grid. Right: The result of physical simulation. Due to the inner bump and the symmetry of the surface, no stable shape can be determined. As not enough stable members can be found, the physical grid does not follow the desired shape.

Among all geodesics on S, the subset minimizing the bending energy in Equation (4.8) is most likely to produce lamellae that nestle to the surface well, as shown in Figure 4.12, bottom. Hence, such minimal energy geodesics are essential candidates for our grids. On the other hand, we also require curves that capture high-K bumps on the surface.

We denote the first kind as *least-effort* geodesics; they run along hyperbolic regions, between elliptic regions (bumps) on the surface. They minimize their arc length and their curvature is low. The second kind are *most-effort* geodesics; they maximize κ_n^2 along their trajectory and their arc length. At the same time, they are attracted to the geometrically exposed features of a surface; their curvature is high and potentially oscillates, as they may travel over multiple elliptic regions. To identify such curves, we formulate their *effort energy* as the integral of the squared normal curvature along the curve c, normalized by the curve length:

$$E_c(c(t_x, t_y)) = \frac{1}{l_c} \int_c \kappa_n(u(s), v(s))^2 \, \mathrm{d}s \,. \tag{4.10}$$

Next, we extend this formulation to the entire grid, such that it ensures that we get as many *least-effort* geodesics and as many *most-effort* geodesics as possible at the same time. As E_c are the energies of our grid members, this is equivalent to pushing them apart as far as possible. Hence, the energy we use to find suitable grid configurations is

$$E_{\text{effort}} = -\sum_{i=1}^{n+m} \left(E_{c,i} - \widehat{E}_c \right)^2 , \tag{4.11}$$

where

$$\widehat{E}_c = \frac{1}{n+m} \sum_{i=1}^{n+m} E_{c,i}$$

is the arithmetic mean of the member energies E_c, and $(n+m)$ is the number of all member curves in the grid. The rationale behind Equation (4.11) is that we maximize the variance of the effort energies, and thus curves are forced to either minimize or maximize their value of E_c.

In practice, we discretize the elastic energy E_c of each geodesic by a weighted sum of κ_n^2, evaluated on the surface mesh, using its parameterization at curve points $q(u, v)$:

$$E_c = \frac{1}{l_c} \sum_j \frac{1}{2} \left\| (q_j - q_{j-1}) \right\| \kappa_n(q_j)^2 + \frac{1}{2} \left\| (q_{j+1} - q_j) \right\| \kappa_n(q_j)^2 ,$$

where j iterates over all curve points of a given member curve c.

4.6.4 Minimization of Elastic Grid Energy

To find the best orientation for the whole grid, we minimize the energies proposed in Sections 4.6.2 and 4.6.3 using the following objective:

$$E_{\text{grid}}(\boldsymbol{t}) = E_{\text{effort}}(\boldsymbol{t}) - \lambda \, E_{\text{shape}}(\boldsymbol{t}) \,, \tag{4.12}$$

where λ is a weighting factor. This functional is a piecewise smooth energy, however, we must expect jumps due to the changes in combinatorics and multiple local minima, which occur when a subset of members has a beneficial orientation, but the rest of the grid has not.

As the grid is parameterized by the locations of the anchor points on the boundary, the variables in our problem are $\boldsymbol{t} = [t_1, \ldots, t_k]$. The grid combinatorics are unchanging in case the surface has a convex boundary, but they need to be adapted in every iteration in case the boundary is non-convex (cf. Section 4.5.4). This can change the number of anchor points, making it particularly difficult to solve with a gradient-based continuous optimization approach. To address this issue, we use a genetic algorithm [Goldberg 1989] to find the best orientation for the whole grid. We formulate the optimization problem as

$$\min_{\boldsymbol{t}} E_{\text{grid}}(\boldsymbol{t}) \;\; \text{s.t.} \begin{cases} \forall \, t_1, \ldots, t_k \in [0, 2) \\ \boldsymbol{A}\boldsymbol{t} \leq \boldsymbol{b} \end{cases} . \tag{4.13}$$

In each optimization step, we allow the values of $\boldsymbol{t}$ range $\in [0, 2)$ in order to deal with the seam of the boundary curve. Subsequently, they are transformed back to $[0, 1)$ respecting the symmetry given by the transformation T in every iteration. To avoid leapfrogging, we apply linear inequality constraints that secure monotonously growing entries in $\boldsymbol{t}$ and a certain minimum distance between member endpoints.

We further provide the GA with an initial population, which is equivalent to rotating the grid on the surface in a number of steps. We observed that this step already roughly sets the orientation of the grid and speeds up convergence.

Our grid design algorithm is implemented in MATLAB, and we use its GA-solver for solving the Optimization Problem (4.13).

4.7 Grid Planarization

Arbitrary geodesic grids cannot be transformed to a planar state without changing either the lengths of members or the locations of their inner intersections. To planarize the grid, we resolve to the second solution and use the concept of sliding notches [Pillwein et al. 2020b]. This type of connection allows for a short amount of sliding at the connection of members and thus provides two additional translational degrees of freedom at each connection.

4.7.1 Planarization Algorithm

We express the locations of inner intersections w.r.t. the barycentric coordinates $\lambda, \bar{\lambda}$ on the members, where overlined quantities refer to the planar configuration (cf. Figure 4.17). For an intersection $q, \bar{q}$, the coordinates are:

$$\lambda_g = \frac{d(p_A, q)}{l_g}, \quad \bar{\lambda}_g = \frac{d(\bar{p}_A, \bar{q})}{l_g},$$
$$l_g = d(p_A, p_B) = d(\bar{p}_A, \bar{p}_B),$$
$$\lambda_h = \frac{d(p_C, q)}{l_h}, \quad \bar{\lambda}_h = \frac{d(\bar{p}_C, \bar{q})}{l_h},$$
$$l_h = d(p_C, p_D) = d(\bar{p}_C, \bar{p}_D).$$

We planarize the grid by first generating an initial planar grid of the same combinatorics and formulate a quadratic optimization problem w.r.t. its 2d endpoint coordinates. Therefore we compute the points

$$\bar{q}_g = \lambda_g \bar{p}_A + (1 - \lambda_g) \bar{p}_B,$$
$$\bar{q}_h = \lambda_h \bar{p}_C + (1 - \lambda_h) \bar{p}_D,$$

which are defined w.r.t. λ_g, λ_h of the geodesic grid and ideally should coincide with $\bar{q}$, please refer to Figure 4.16 for a depiction.

Since we want to minimize the length of the notches, we formulate the planarization problem as a constrained quadratic minimization with the following objective:

$$E_{\text{notch}} = \sum_{j=1}^{n_q} \| \bar{q}_{g_j} - \bar{q}_{h_j} \|^2, \tag{4.14}$$

where $j = [1 \dots n_q]$ denotes the intersections of the grid.

To ensure that the planar grid elements perfectly maintain the total lengths of their spatial counterparts, we introduce hard constraints which enforce that lengths between curves on the surface and in the plane match:

$$G_{\text{len}} = \| \bar{p}_y - \bar{p}_x \|^2 - d(p_y, p_x)^2 = 0,$$

where $\bar{p}_y, \bar{p}_x$ and p_y, p_x are the endpoints of corresponding members in the plane and on the surface.

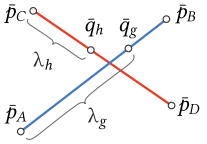

Fig. 4.16: In order to keep our optimization problem quadratic, we do not explicitly compute $\bar{q}$, but use the barycentric coordinates λ_g, λ_h to compute $\bar{q}_g, \bar{q}_h$. If $\lambda_g = \bar{\lambda}_g$ and $\lambda_h = \bar{\lambda}_h$, then $\bar{q}_g = \bar{q}_h = \bar{q}$ and the connection has no notch, otherwise we minimize the distance between $\bar{q}_g$ and $\bar{q}_h$.

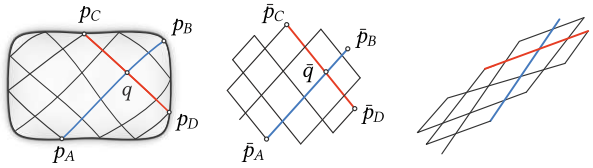

Fig. 4.17: Left: For intersection q, we determine partial lengths $d(p_A, q)$, $d(p_C, q)$, and total lengths $d(p_A, p_B)$, $d(p_C, p_D)$. Middle: We initialize the planar grid, and parameterize it by its endpoint coordinates. Matching partial and total lengths with the corresponding values on the surface is generally not possible. Right: Our planarization algorithm maintains total lengths perfectly and partial lengths as well as possible.

4.7.2 Fabrication Constraints

For manufacturing purposes, the width w of lamellae must be considered. Therefore we add optional minimum distance constraints, ensuring an offset between consecutive members of the same family. To this end, we use the endpoints $\bar{p}_1, \bar{p}_2, \bar{p}_3, \bar{p}_4$ of two consecutive members of a family (cf. Figure 4.18). We introduce the constraints w.r.t. the sign of determinants of vectors between the endpoints:

$$e_1 = \det\left(\bar{v}_{14}, \bar{v}_{13}\right) \leq 0,$$
$$e_2 = \det\left(\bar{v}_{24}, \bar{v}_{23}\right) \leq 0,$$
$$e_3 = \det\left(\bar{v}_{31}, \bar{v}_{32}\right) \leq 0,$$
$$e_4 = \det\left(\bar{v}_{41}, \bar{v}_{42}\right) \leq 0,$$

where each e_i checks one endpoint and positive values indicate overlaps. Since these constraints are rather restrictive, we introduce them as soft constraints within the objective as:

$$E_{\text{fab}} = \sum_{k=1}^{n-1} \sum_{i=1}^{4} B(e_{i,k} > 0)(e_{i,k}) + \sum_{k=1}^{m-1} \sum_{i=1}^{4} B(e_{i,k} > 0)(e_{i,k}),$$

where $B(\cdot) \rightarrow \{0, 1\}$ is a Boolean operator which is used to discard cases where the constraints are not violated and k, i iterate over all pairs of neighboring grid members $g = \{c_1, \dots c_n\}$ (fist sum) and $h = \{c_1, \dots c_m\}$ (second sum).

We minimize the planarization objective using Pareto weighting of the notch and fabrication terms

$$E_{\text{planar}} = E_{\text{notch}} + \mu E_{\text{fab}} \quad \text{s. t.} \quad G_{\text{len}} = \mathbf{0}, \tag{4.15}$$

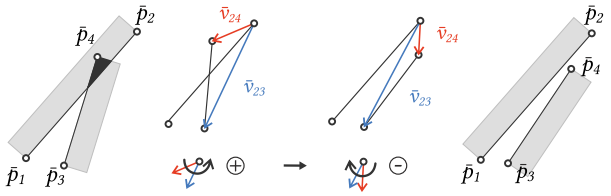

Fig. 4.18: Endpoints $\bar{p}_1, \bar{p}_2, \bar{p}_3, \bar{p}_4$ of two consecutive lamellae are defined by the offset $w/2$ from the centerline. We avoid overlapping by ensuring that certain determinants of vectors connecting the endpoints have the right sign.

Please note that the objective function and the constraints are quadratic w.r.t. the variables and an analytic gradient can be computed. We solve this optimization problem using sequential quadratic programming in MATLAB.

4.8 Results and Evaluation

Using our method, we have represented a number of surfaces which are depicted in Figures 4.20 and 4.21. The input surfaces have positive and negative Gaussian curvature regions, inner bumps, convex and non-convex boundaries.

We fabricated the models from lime wood or acrylic glass, the lamellae were laser-cut from thin plates, connected by screws, and placed on 3d-printed supports after assembly. The supports have inclined contact areas to enforce the desired shape of the grid (cf. Section 4.3.1).

4.8.1 Quantitative Results

In Table 4.1 we summarize quantitative results of our method for the models depicted in Figures 4.20, 4.21, and 4.15. To check the agreement of the grid shape and the target surface, we simulated the physical behavior of the deployed grid using the discrete elastic rods model [Bergou et al. 2008]. We refer the reader to the paper for details. In Table 4.1, RMS Δ denotes the root mean square distance between grid vertices and the base mesh and max Δ is the maximum distance.

Convergence times of our grid algorithm t_{opt} mainly depend on the number of grid members and the mesh resolution. Precomputation times t_{pre} depend on the mesh resolution, they include computing the distance fields and checking the boundary. Finally, planarization times t_{pla} depend on the number of values of $\mathbf{t} = [t_1, \ldots t_k]$.

4.8.2 Implementation

Our grid design algorithm is implemented in MATLAB, we use its GA-solver to solve the Optimization Problem (4.13). To planarize the grid, we solve the Optimization Problem (4.15) utilizing MATLAB's sequential quadratic programming solver using analytical gradients. We furthermore implemented the DER-simulation in C++, building upon the framework of [Vekhter et al. 2019]. To compute the distance fields on the mesh, we use the VTP algorithm by [Qin et al. 2016]. For the final computation of the geodesic paths, we use the algorithm for exact geodesics between two points by [Surazhsky et al. 2005].

4.9 Discussion and Conclusions

4.9.1 Discussion and Limitations

Surfaces with Inner Bumps We have shown that surfaces with inner bumps ($H < 0$) can be realized without inner supports (cf. Figure 4.20, example Hills), but in general, this is not possible (cf. Figure 4.20, example Flower). In such cases, our shape stability energy $E_{\text{shape}} \in [0, 1]$ provides information whether the grid can support itself or is likely to deviate from the target surface.

Holes in the Design Surface The input surfaces for our method need to be topological disks; we cannot compute grids on surfaces with holes. To adapt our approach to a surface with only one hole would require a second dual space because two boundaries must be taken into account. Additionally, a connection between the dual spaces needs to be established for geodesics that start at one boundary and end at the other. However, we can realize such surfaces using our present approach by splitting them into two or more non-convex surfaces [Pillwein et al. 2021a].

Tab. 4.1: Quantitative results of our method. We measure the root mean square error (RMS Δ) and the maximum error (max Δ) between the member centerlines and the target mesh in centimeters; ε_{geo} refers to the mean deviation between traced geodesics and our reconstruction w.r.t. the mean edge-length in percent. Timings are in seconds, t_{pre} refers to computation of distance fields and analysis of the boundary, t_{opt} refers to the GA-convergence times, and t_{pla} to the planarization of the grid. $|M_V|$ expresses the number of mesh vertices and n the number of grid members. Measured on an AMD Ryzen 7 1700 Eight-Core using parallel computing.

	Starship	Bumps	Flower	Hills	Moon	Drop
width	60.0	60.0	55.5	60.0	54.2	60.0
depth	40.4	37.5	60.0	47.5	60.0	60.0
heigth	6.8	8.9	20.0	5.9	10.6	4.2
$\lvert M_V \rvert$	3734	3333	3975	5102	3437	4591
n	18	22	30	22	22	18
t_{pre}	1.73	1.88	3.74	4.31	3.06	4.61
t_{opt}	3.68	6.01	6.13	5.71	4.41	5.86
t_{pla}	0.21	0.51	0.96	0.87	0.27	0.47
ε_{geo}	8.37	10.61	6.97	7.04	8.54	6.23
RMS Δ	0.25	0.36	0.48	0.29	0.38	1.45
max Δ	0.57	0.64	1.79	0.52	0.68	7.24
E_{shape}	1.00	1.00	0.88	0.94	1.00	0.45

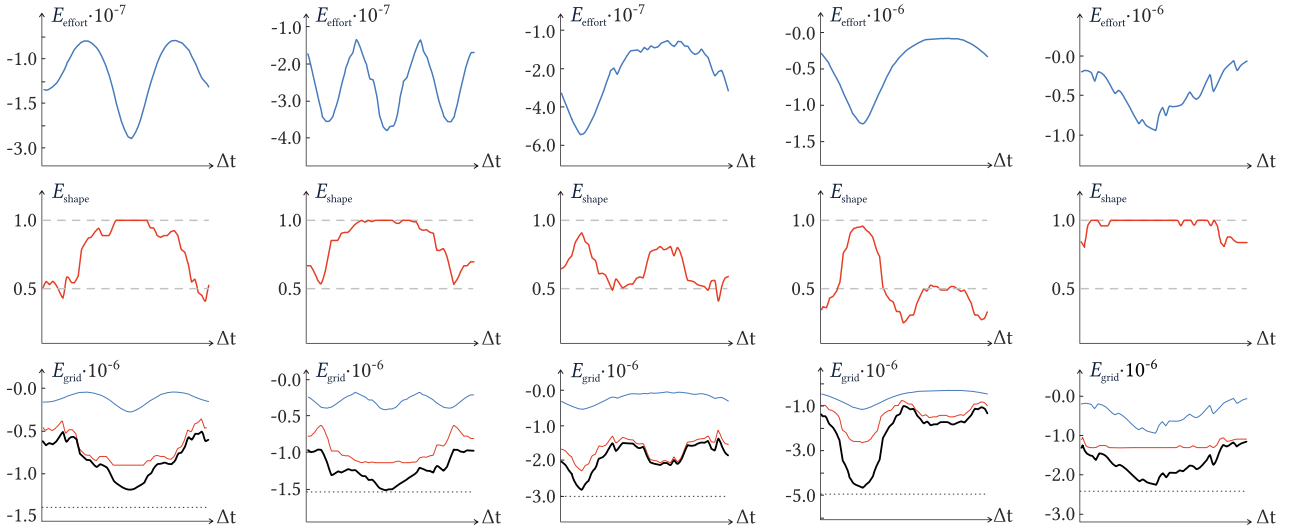

Fig. 4.19: Energies E_{effort}, E_{shape} and E_{grid} for our fabricated examples of Figures 4.20 and 4.21. The plots show the energies when the grid is rotated on the surface for a quarter rotation; the black dotted lines represent the final energy of the grid after optimization. Jumps in the energies indicate changes in combinatorics in the grid (cf. Equation (4.12)). From left to right: Starship, Bumps, Flower, Hills, and Moon.

Deployment The deployment of physical grids depends on one rotational degree of freedom (DoF), which controls the expansion of the scissor linkage, and additional translational DoF, introduced by the notches. Kinematically, the grids are related to other elastic scissor-like grid structures which use notches [Pillwein et al. 2020b; Pillwein et al. 2020a; Pillwein et al. 2021a], in contrast to structures with a rotational DoF only [Panetta et al. 2019; Soriano et al. 2019].

Our approach does not explicitly control individual notch lengths, it minimizes the overall notch lengths. Hence, when expanding a grid, it may not simply buckle into the final shape but nevertheless deliver perfect results when fixed to the supports. It would be interesting to adapt the planarization w.r.t. producing a large number of notches of length zero and see how the shape of the planar grid changes.

Grid Optimization and Combinatorics In our current approach, we only change the combinatorics of the grid in the case of non-convex boundaries. Additional changes in the combinatorics during the optimization process, regardless of convexity, could promise even better results w.r.t. the grid energy E_{grid}. However, we do not expect substantial improvements. This problem could be tackled using mixed-integer programming in the grid optimization, using an additional integer variable controlling the combinatorics.

Computational Efficiency Our method is streamlined for computational efficiency and delivers results in a matter of seconds. We compute distance fields at the beginning and subsequently reuse them for all computations, even to circumvent costly path tracing of geodesics. Tracing geodesics using the implementation of Surazhsky *et al.* [Surazhsky et al. 2005] significantly slows down the convergence of the grid optimization ranging from a factor of 108 for the example Starship up to 283 for the example Hills. Despite our simplifications and the reduced resolution of the grid members, the effort energy E_{effort} is smooth and jumps only if grid combinatorics change (cf. Figure 4.19). The shape stability energy E_{shape} is less smooth but still provides reliable information on whether the grid will be able to maintain the desired shape.

Mesh Resolution Our method requires a certain minimum resolution of the input mesh. If it is too coarse, we cannot find positions of the intersections of geodesics accurately (cf. Section 4.5.2). Moreover, as the used distance fields only store distances for mesh vertices, we need interpolation, which depends on the resolution. We noticed that the regions close to the boundary are prone to inaccuracies, so we recommend high resolution in this area. For our examples, we used meshes with about 4000 vertices (cf. Table 4.1).

4.9.2 Conclusions

We presented an approach for the computational design of elastic gridshell structures that ensures to capture the surface characteristics well and provide aesthetic grid layouts. Our fast form-finding algorithm is based on the notion of *least-effort* and *most-effort* geodesics, self-supporting members, and mutual stabilization to ensure close approximation of the input surfaces. An important outcome of our research is that even undulating surfaces can be well approximated by curve networks which minimize and maximize their normal curvature along their trajectories

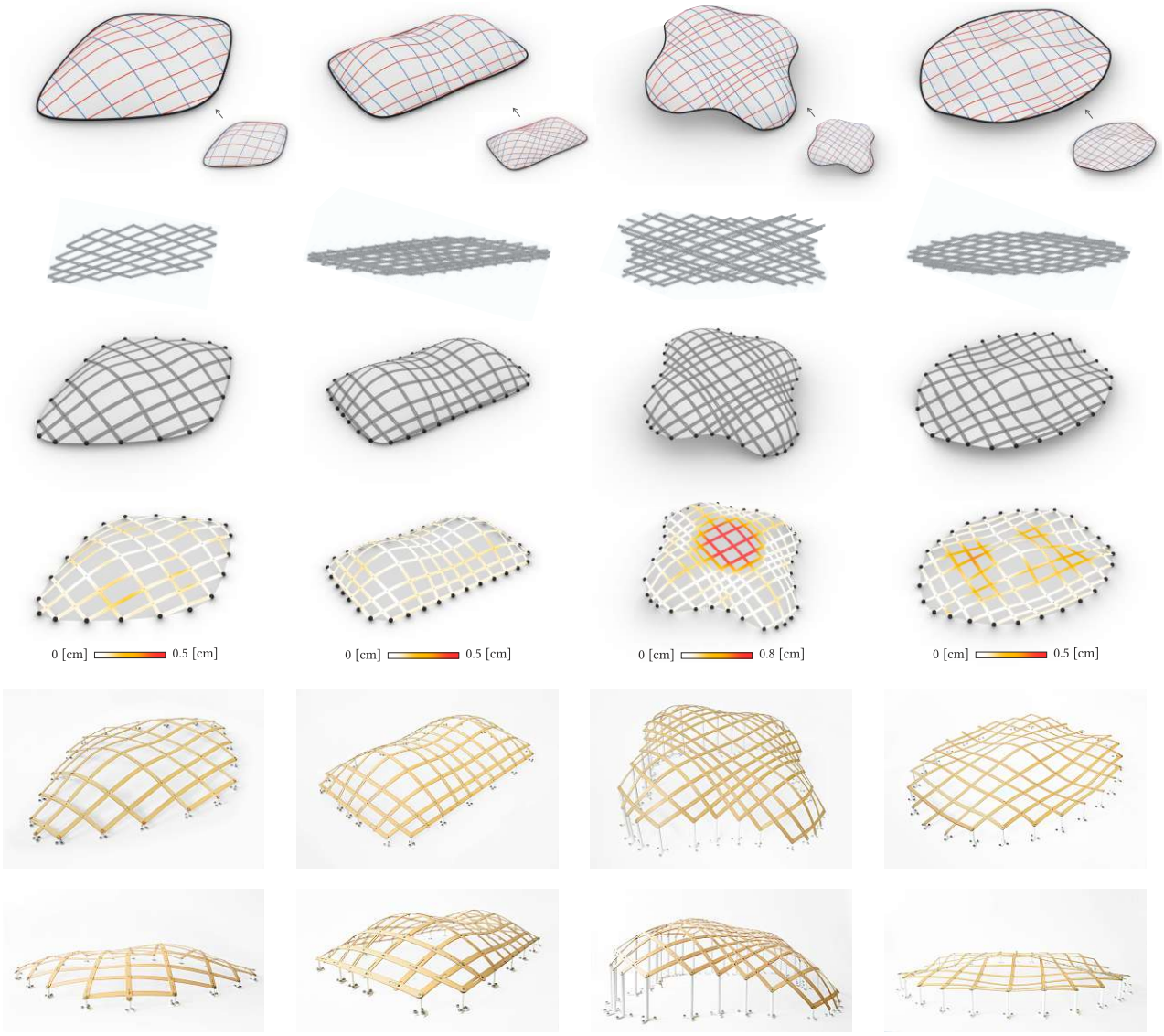

Fig. 4.20: Computed, simulated, and fabricated results of our method. From left to right: Starship, Bumps, Flower, Hills. All grids nestle the respective surfaces well and capture their characteristics. Example Flower is a limit case: The central inward bump cannot be captured by an elastic gridshell without inner supports (cf. Section 4.9). However, example Hills shows that inner bumps can be feasible without inner supports if enough *least-effort* and *most-effort* geodesics can be found. When it is deployed and fixed to 3d-printed anchors with inclined contact areas, the shape of a grid emerges. Please note that the fabricated results were optimized using a previous version of energy E_{effort} and were not re-fabricated because the deviations are not noticeable in the models. Best seen in the electronic version in closeup.

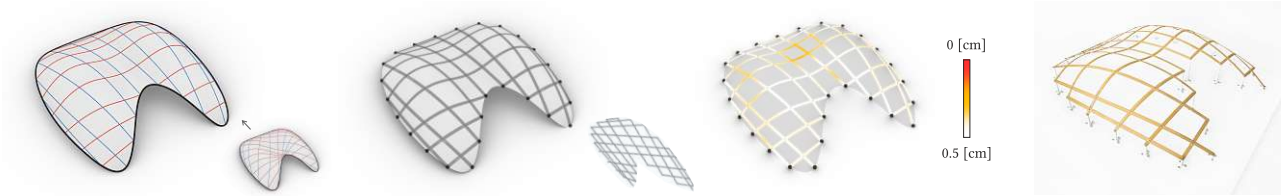

Fig. 4.21: Computed, simulated, and fabricated example Moon. The red family of geodesics is split into sub-families due to the non-convexity of the boundary. The physical grid nestles the surface very well. Please note that the fabricated result was optimized using a previous version of energy E_{effort} and was not re-fabricated because the deviations are not noticeable in the model.

simultaneously. In the future, we want to analyze this dependency further in order to provide theoretical results.

Our method is based on distance computations only and omits expensive computations, like geodesic path tracing or physical simulations. We allow for surfaces with non-convex boundaries and updates of the combinatorics of the grid during optimization to ensure functional grids, which can be solved efficiently in the discrete domain. We introduce a planarization algorithm for geodesic grids with a quadratic objective function and quadratic constraints for the sake of efficient computation. As a result, the grids have straight members and are perfectly planar, which favors fabrication, transportation, and assembly.

Our method is inspired by architecture and design and intended as an easy-to-handle tool for designers to quickly create physically sound and aesthetically pleasing spatial grid structures. Finally, we introduced a digital fabrication pipeline and presented a set of examples with varying curvatures, and produced small-scale gridshells as proof of our concept.

4.10 Acknowledgments

This research was funded by the Vienna Science and Technology Fund (WWTF) ICT15-082 (https://www.wwtf.at). The authors thank Florian Rist and Johanna Kübert for fabricating the models, as well as Kurt Leimer and Dominik Pint for support with coding and production tasks.

Chapter 5

Discussion and Conclusion

5.1 Discussion

This section summarizes the discussion of the papers presented in Chapters 2, 3, and 4, and provides additional discussion w.r.t. the bigger context of this thesis.

Representable Shapes. Due to the elastic shape response of grid members, it is not possible to clearly describe the space of feasible target surfaces for elastic gridshells. Finding appropriate constraints (e.g., supports) or achieving desired structural properties complicates this mission further. Thus, the feasibility of target surfaces still needs to be assessed on an individual basis. However, some conclusions on representable shapes can be drawn for elastic geodesic grids:

- Elastic grids are smooth in appearance, adopting the shape of minimal elastic energy. Thus, distinct local variations of the Gaussian curvature K or even sharp ridges are not desirable. Additionally, shortest geodesics avoid regions of high K. Hence, not all surfaces allow the covering with a grid of shortest geodesics (cf. Section 1.1.4).

  From an engineering point of view, the higher the curvature of a grid member, the more flexible it needs to be to avoid breaking. In technical terms, its stiffness needs to be reduced, e.g., by downsizing the cross-sectional dimensions. Unfortunately, this negatively impacts usability, e.g., for load-bearing structures.

- If the grid's resolution is too low to correspond to the frequency of the surface's curvature features, a close approximation is not possible. Highly-detailed surfaces need fine grid resolutions or, alternatively, multi-resolution approaches, as suggested in Chapter 3.

- Fastening the connections of members after deployment ultimately fixes interior grid angles. After that, the grid's shape is determined up to isometries. In other words, a family of shapes can be obtained by introducing different boundary conditions. Some shapes are not feasible with supports only along a grid's boundary, as their influence to the overall shape of the grid is limited: local, inner bumps or dents of a grid may have multiple equilibrium states, which belong to different local minima in elastic energy. Hence, reliably approximating target surfaces with inner bumps or dents is challenging (cf. Sections 2.7.2 and 4.9.1).

- Obtaining a relationship between given target surfaces and structurally capable elastic grids would be favorable for many applications. While it is clear that dome-like shapes are efficient due to a large portion of shell-action in their members, finding more elaborate and equally capable shapes is an open research question. However, using optimization, capable and shape-stable designs are feasible even for complicated design surfaces with many changes in K, or inner bumps and dents, as Chapter 4 suggests.

- Using geodesics as starting point for grid-members limits the space of feasible shapes. Other approaches demonstrate that the space of shapes is influenced not only by the layout of the grid, but also by different cross-sections [Panetta et al. 2019]. Elastic geodesic grids do not enjoy this additional freedom, as cross-sections are restricted to slender rectangles (cf. Section 2.7.1). However, these simple cross-sections help to avoid higher order geometric effects, like buckling of local cross-section parts.

Sliding Connections. It is a known fact in differential geometry that an arbitrary geodesic grid cannot be mapped onto a geodesic grid in the plane without stretching or shortening grid members (cf. Section 1.6). Hence, planarizing a geodesic grid generally requires additional degrees of freedom. Notches provide this freedom by allowing members to slide at inner joints, which greatly improves the quality of approximation (cf. Section 2.7.2). Despite their theoretical necessity, notches come with some practical drawbacks:

- Densification of members in elastic geodesic grids is limited by the notch lengths, which only depend on the member's locations, not their number.

- Grid members would slide perfectly inside the elongated holes only in an ideal world without friction. However, due to friction (cf. Section 2.7.3), the sliding of members needs to be assisted with some extra energy input. Nevertheless, the movement of joints due to the additional DoF w.r.t. the notches is controlled by the single, global DoF w.r.t. the shearing angle α (cf. Figure 1.1), and does not produce additional mechanisms in the deployed state (cf. Section 4.9.1).

- Physically, the notches are implemented by elongated holes, which unfortunately are sources of material fail-

ure, which linear elastic models cannot account for (cf. Section 2.7.3).

Surface Topology, Convexity of Boundary and Grid Combinatorics. Each shortest curve on a surface is a geodesic, as long as it does not contact the surface boundary. Such contacts never happen on surfaces that are topological disks with convex boundaries, but will happen if the boundaries are non-convex. Thus, creating valid geodesic grids on such surfaces requires changing the grid combinatorics (cf. Section 4.9.1). The method introduced in Chapter 4 uses a so-called dual-space, which readily encodes non-convex boundaries, even handling multiple non-convex parts. However, navigating this dual-space becomes increasingly complex if there are non-convex parts within larger non-convex parts, but it is nevertheless feasible.

Target surfaces, which are not topological disks, need to be cut open to approximate them with elastic geodesic grids. Indeed, using the method introduced in Chapter 4, allowing disks with holes is in principle possible: The boundaries of the holes require a dual-space for every hole, and additional dual-spaces which connect the dual-spaces, making the design process quite complicated (cf. Section 4.9.1). Thus, the most effective solution is to cut open disks with holes.

Computational Efficiency of Form-Finding. The methods presented in this thesis are intended as fast form-finding tools that provide solutions in a matter of seconds, and largely avoid expensive computations. There are two bottlenecks in the computational design of elastic geodesic grids: tracing paths of shortest geodesics, and computing the equilibrium shape of networks of lamellas:

- Tracing a shortest geodesic either requires computing two distance fields emanating from the endpoints and tracing the shortest connecting curve, or solving a variational curve-shortening problem. Since all form-finding approaches in this thesis require precomputing numerous distance fields (to compute the distance maps or the dual-space), simply reusing them is quite efficient. However, during form-finding, actually tracing geodesics is still quite time-consuming. For models of the method presented in Chapter 4, roughly hundreds or even thousands of iterations were necessary until convergence, where each iteration corresponds to an individual grid with two families of numerous geodesics. Hence, fast short-cuts were introduced, like computing intersections of geodesics without computing their paths, accepting tolerable losses of accuracy.

- Similar to tracing geodesic paths, simulating the equilibrium shape in a large number of iterations is computationally costly. Even optimized implementations of the Discrete Elastic Rods method [Bergou et al. 2008; Bergou et al. 2010] require up to seconds [Panetta et al. 2019] for computing the equilibrium shape of a grid, which would result in obstructive accumulated simulation times in tens of minutes. A geometrically based heuristic (cf. Section 4.6.2) was introduced to substitute the simulation of equilibrium shapes. This step is admissible since the overall shape of the grid and the individual shapes of members are strongly linked: If too many members are far from an equilibrium shape, the grid will deviate from the target surface, while the correspondence will be good if there are many well-distributed stabilizing members. Hence, the problem of computing the equilibrium shape was replaced by evaluating how much individual members deviate from stable shapes, which is a far more accessible problem.

5.2 Limitations and Future Work

An exciting direction for future work would be identifying surfaces and grids which allow for particularly short sliding connections. From a theoretical point of view, surfaces that can be approximated without notches are restricted to Liouville surfaces. Well-known examples are the hyperbolic paraboloid and the one-sheeted hyperboloid. Voss surfaces, which allow the definition of conjugate geodesic nets, might be interesting. They, too, do not allow a length-preserving transformation of geodesic grids into the plane but might be practical in minimizing notch lengths.

This thesis is primarily focused on shape approximation of target surfaces, while the structural capabilities of the resulting grids were not taken into account. To advance the structural efficiency of elastic grids, alternative design processes would be needed, which finally result in pure shell-action (cf. Section 1.2.3).

Elastic simulations were limited to establish the equilibrium shape of the deployed grids. Unlike other approaches, which actually simulate deployment [Panetta et al. 2019], intermediate states were assumed to be feasible if the final state is feasible. The Discrete Elastic Rods model [Bergou et al. 2008; Bergou et al. 2010]) was used to simulate equilibrium shapes, where a combination of geometric energies is minimized. Due to its inherent simplifications and non-physical components in the energy functional, e.g., positional constraints, simulation results are only a starting point for real-world implementations. Furthermore, the model does not allow incorporating forces directly, but only allows displacements as additional positional constraints.

Equilibrium shapes of elastic grids correspond to local minima of their potential energy. The properties of these local minima w.r.t. small perturbations were not analyzed. However, such sensitivity analyses are critical, e.g., for designs with local maxima of the Gaussian curvature K (shallow inner bumps or dents), as the grid may buckle into different locally energy minimizing configurations.

5.3 Conclusion

This thesis proposes a comprehensive study on how to design scissor-like deployable elastic geodesic grid structures intended to approximate given target surfaces.

Different approaches reduce the complexity of form-finding by introducing abstract spaces, where computing layouts is much easier. The cornerstone of these approaches are shortest geodesics, their connection to distances on surfaces, and their straightness. The latter property is particularly valuable for practical reasons, such as material-efficient fabrication, easy deployment, simple transport, and space-saving storage.

The major challenges this thesis tends to are twofold: Firstly, taking designer-provided free-form surfaces as input, differential geometry tells that corresponding geodesic grids cannot be flattened. The concept of notches solves this problem. The additional degrees of freedom are controlled by the global degree of freedom which governs deployment, and enable the perfect approximation of target surfaces from a geometric point of view. In other words, the notches ensure that the grid can always be assembled in the plane, which is much easier and faster than in space. Secondly, it proposes multiple automated algorithms which solve the inverse design problem of finding scissor-like deployable gridshells based on geodesics. No expert knowledge is required to design grid layouts, which makes the proposed approaches practical for all design disciplines and rapid form-finding.

Furthermore, the papers of this thesis provide impulses to speed up the form-finding of elastic geodesic grid structures at an acceptable loss of accuracy. Strategies include efficient reuse of once calculated distance fields, avoiding the necessity of tracing geodesic paths, and an empiric approach to assess the shape stability of geodesic grids w.r.t. physical equilibrium shapes, which circumvents physical simulation.

Finally, several fabricated models of different scales prove the practical feasibility of the proposed methods. Form-finding focuses on a single objective: shape agreement of elastic geodesic grids with target surfaces. Aspiring high efficiency and functionality of the grids, many questions w.r.t. form-finding remain, such as favorable target surfaces. While such problems are particularly difficult to solve due to the elastic shape response, this thesis contributes to their investigation and shall motivate further interesting research.

Bibliography

Adiels, E., N. Bencini, C. Brandt-Olsen, A. Fisher, I. Näslund, R. K. Otani, E. Poulsen, P. Safari, and C. J. Williams (2018). "Design, fabrication and assembly of a geodesic gridshell in a student workshop". In: *Proceedings of IASS Annual Symposia*. Vol. 2018. 20. International Association for Shell and Spatial Structures (IASS), pp. 1–8.

Adikusuma, Y. Y., Z. Fang, and Y. He (2020). "Fast Construction of Discrete Geodesic Graphs". In: *ACM Trans. Graph.* 39.2. ISSN: 0730-0301. DOI: 10.1145/3144567. URL: https://doi.org/10.1145/3144567.

Adriaenssens, S., M. Barnes, R. Harris, and C. Williams (2014a). "Dynamic relaxation: Design of a strained timber gridshell". In: *Shell Structures for Architecture*. Routledge, pp. 103–116.

Adriaenssens, S., P. Block, D. Veenendaal, and C. Williams (2014b). *Shell Structures for Architecture : Form Finding and Optimization*. en. 1st ed. Abingdon: Routledge/Taylor & Francis Group. ISBN: 978-1-3158-4927-0. URL: https://www.bloomsburyarchitecturelibrary.com/encyclopedia?docid=b-9781315849270.

Asnani, V., D. Delap, and C. Creager (2009). "The development of wheels for the Lunar Roving Vehicle". In: *Journal of Terramechanics* 46.3. Special Issue: Robotics, pp. 89–103. ISSN: 0022-4898. DOI: https://doi.org/10.1016/j.jterra.2009.02.005. URL: https://www.sciencedirect.com/science/article/pii/S0022489809000263.

Baek, C. and P. M. Reis (2019). "Rigidity of hemispherical elastic gridshells under point load indentation". In: *Journal of the Mechanics and Physics of Solids* 124, pp. 411–426. ISSN: 0022-5096. DOI: 10.1016/J.JMPS.2018.11.002. URL: https://www.sciencedirect.com/science/article/pii/S0022509618306203?via%3Dihub.

Baek, C., A. O. Sageman-Furnas, M. K. Jawed, and P. M. Reis (2018). "Form finding in elastic gridshells". In: *Proceedings of the National Academy of Sciences of the United States of America* 115.1, pp. 75–80. ISSN: 10916490. DOI: 10.1073/pnas.1713841115. URL: https://www.pnas.org/content/115/1/75%20https://www.pnas.org/content/115/1/75.abstract.

Bergou, M., B. Audoly, E. Vouga, M. Wardetzky, and E. Grinspun (2010). "Discrete viscous threads". In: *ACM Trans. Graph.* 29.4, p. 1. ISSN: 0730-0301. DOI: 10.1145/1778765.1778853. URL: http://portal.acm.org/citation.cfm?doid=1399504.1360662%20http://portal.acm.org/citation.cfm?doid=1778765.1778853.

Bergou, M., M. Wardetzky, S. Robinson, B. Audoly, and E. Grinspun (2008). "Discrete elastic rods". In: *ACM Trans. Graph.* 27.3, p. 1. ISSN: 0730-0301. DOI: 10.1145/1360612.1360662. URL: http://portal.acm.org/citation.cfm?doid=1833349.1778853%20http://portal.acm.org/citation.cfm?doid=1360612.1360662.

Bermano, A. H., T. Funkhouser, and S. Rusinkiewicz (2017). "State of the Art in Methods and Representations for Fabrication-Aware Design". In: *Computer Graphics Forum* 36.2, pp. 509–535. ISSN: 01677055. DOI: 10.1111/cgf.13146. URL: http://doi.wiley.com/10.1111/cgf.13146.

Binninger, A., F. Verhoeven, P. Herholz, and O. Sorkine-Hornung (2021). "Developable Approximation via Gauss Image Thinning". In: *Computer Graphics Forum (proceedings of SGP 2021)* 40.5, pp. 289–300. ISSN: 1467-8659. DOI: 10.1111/cgf.14374.

Block, P. and J. Ochsendorf (2007). "Thrust network analysis: a new methodology for three-dimensional equilibrium". In: *Journal of the International Association for shell and spatial structures* 48.3, pp. 167–173.

Bouleau, E., F. Isvoranu, J. Panetta, and M. Pauly (2019). "χ-Shell, a new spatial deployable lattice compared to traditional reticulated shells". In: *Proceedings of IASS Annual Symposia*. Vol. 2019. 11. International Association for Shell and Spatial Structures (IASS), pp. 1–8.

Chen, D., P. Sitthi-amorn, J. T. Lan, and W. Matusik (2013). "Computing and Fabricating Multiplanar Models". In: *Computer Graphics Forum* 32.2pt3, pp. 305–315. ISSN: 01677055. DOI: 10.1111/cgf.12050. URL: http://doi.wiley.com/10.1111/cgf.12050.

Chen, J. and Y. Han (1990). "Shortest Paths on a Polyhedron". In: *Proceedings of the Sixth Annual Symposium on Computational Geometry*. SCG '90. Berkley, California, USA: Association for Computing Machinery, pp. 360–369. ISBN: 0897913620. DOI: 10.1145/98524.98601. URL: https://doi.org/10.1145/98524.98601.

Chen, T., J. Panetta, M. Schnaubelt, and M. Pauly (2021). "Bistable Auxetic Surface Structures". In: *ACM Trans. Graph.* 40.4. ISSN: 0730-0301. DOI: 10.1145/3450626.3459940. URL: https://doi.org/10.1145/3450626.3459940.

Chilton, J. and G. Tang (2016). *Timber gridshells: architecture, structure and craft*. 1st ed. Routledge. URL: https://doi.org/10.4324/9781315773872.

Crane, K., M. Livesu, E. Puppo, and Y. Qin (2020). "A Survey of Algorithms for Geodesic Paths and Distances". In: *arXiv*. arXiv: 2007.10430. URL: http://arxiv.org/abs/2007.10430.

Crane, K., C. Weischedel, and M. Wardetzky (2013). "Geodesics in Heat: A New Approach to Computing Distance Based on Heat Flow". In: *ACM Trans. Graph.* 32.5. ISSN: 0730-0301. DOI: 10.1145/2516971.2516977. URL: https://doi.org/10.1145/2516971.2516977.

D'Amico, B., A. Kermani, H. Zhang, A. Pugnale, S. Colabella, and S. Pone (2015). "Timber gridshells: Numerical simulation, design and construction of a full scale structure". In: *Structures*. Vol. 3. Elsevier, pp. 227–235.

Demaine, E. and T. Tachi (2017). "Origamizer: A practical algorithm for folding any polyhedron". In: *Proceedings of the 33rd International Symposium on Computational Geometry (SoCG 2017)*. URL: https://hdl.handle.net/1721.1/137685.

Desbrun, M., M. Meyer, P. Schröder, and A. H. Barr (1999). "Implicit fairing of irregular meshes using diffusion and curvature flow". In: *Proceedings of the 26th annual conference on Computer graphics and interactive techniques - SIGGRAPH '99*. New York, New York, USA: ACM Press, pp. 317–324. ISBN: 0201485605. DOI: 10.1145/311535.311576. URL: http://portal.acm.org/citation.cfm?doid=311535.311576.

Deuss, M., D. Panozzo, E. Whiting, Y. Liu, P. Block, O. Sorkine-Hornung, and M. Pauly (2014). "Assembling self-supporting structures". In: *ACM Trans. Graph.* 33.6, pp. 1–10. ISSN: 0730-0301. DOI: 10.1145/2661229.2661266. URL: http://dl.acm.org/citation.cfm?id=2661229.2661266.

Dickson, M. and D. Parker (2014). *Sustainable Timber Design*. 1st ed. Routledge. URL: https://doi.org/10.4324/9781315774114.

Dijkstra, E. W. et al. (1959). "A note on two problems in connexion with graphs". In: *Numerische mathematik* 1.1, pp. 269–271.

do Carmo, M. (1992). *Riemannian geometry*. Birkhaeuser, p. 300. ISBN: 9780817634902. URL: https://www.springer.com/gp/book/9780817634902.

Douthe, C., J. Caron, and O. Baverel (2010). "Gridshell structures in glass fibre reinforced polymers". In: *Construction and Building Materials* 24.9, pp. 1580–1589. ISSN: 0950-0618. DOI: https://doi.org/10.1016/j.conbuildmat.2010.02.037. URL: https://www.sciencedirect.com/science/article/pii/S0950061810000802.

Du Peloux, L., F. Tayeb, O. Baverel, and J.-F. Caron (2016). "Construction of a large composite gridshell structure: a lightweight structure made with pultruded glass fibre reinforced polymer tubes". In: *Structural Engineering International* 26.2, pp. 160–167.

Dudte, L. H., E. Vouga, T. Tachi, and L. Mahadevan (2016). "Programming curvature using origami tessellations". In: *Nature Materials* 15.5, pp. 583–588. ISSN: 1476-1122. DOI: 10.1038/nmat4540. URL: http://www.nature.com/articles/nmat4540.

Eigensatz, M., M. Kilian, A. Schiftner, N. J. Mitra, H. Pottmann, and M. Pauly (2010). "Paneling architectural freeform surfaces". In: *ACM Trans. Graph.* 29.4, p. 1. ISSN: 0730-0301. DOI: 10.1145/1778765.1778782. URL: http://portal.acm.org/citation.cfm?doid=1778765.1778782.

Fleischmann, M. and A. Menges (2011). "Icd/itke research pavilion: A case study of multi-disciplinary collaborative computational design". In: *Computational design modelling*. Springer, pp. 239–248.

Garg, A., A. O. Sageman-Furnas, B. Deng, Y. Yue, E. Grinspun, M. Pauly, and M. Wardetzky (2014). "Wire mesh design". In: *ACM Trans. Graph.* 33.4, pp. 1–12. DOI: 10.1145/2601097.2601106. URL: http://dl.acm.org/citation.cfm?doid=2601097.2601106.

Gauss, C. F. (1828). *Disquisitiones generales circa superficies curvas*. Vol. 1. Typis Dieterichianis.

Gavriil, K., A. Schiftner, and H. Pottmann (2019). "Optimizing B-spline surfaces for developability and paneling architectural freeform surfaces". In: *Computer-Aided Design* 111, pp. 29–43.

Gengnagel, C., J. Lienhard, H. Alpermann, C. Gengnagel, and J. Knippers (2013). "Active bending, a review on structures where bending is used as a self-formation process". In: *International Journal of Space Structures* 28.3-4, pp. 187–196.

Goldberg, D. E. (1989). *Genetic Algorithms in Search, Optimization and Machine Learning*. 1st. USA: Addison-Wesley Longman Publishing Co., Inc. ISBN: 0201157675.

Guseinov, R., C. McMahan, J. Pérez, C. Daraio, and B. Bickel (2020). "Programming temporal morphing of self-actuated shells". In: *Nature Communications* 11.1, pp. 1–7. ISSN: 20411723. DOI: 10.1038/s41467-019-14015-2. URL: https://doi.org/10.1038/s41467-019-14015-2.

Guseinov, R., E. Miguel, and B. Bickel (2017). "CurveUps". In: *ACM Trans. Graph.* 36.4, pp. 1–12. ISSN: 0730-0301. DOI: 10.1145/3072959.3073709. URL: http://dl.acm.org/citation.cfm?doid=3072959.3073709.

Hafner, C. and B. Bickel (2021). "The Design Space of Plane Elastic Curves". In: *ACM Trans. Graph.* 40.4. ISSN: 0730-0301. DOI: 10.1145/3450626.3459800. URL: https://doi.org/10.1145/3450626.3459800.

Han, X., H. Yu, Y. Yu, and J. Zhang (2017). "A fast propagation scheme for approximate geodesic paths". In: *Graphical Models* 91, pp. 22–29. ISSN: 1524-0703. DOI: https://doi.org/10.1016/j.gmod.2017.02.004. URL: https://www.sciencedirect.com/science/article/pii/S1524070317300115.

Happold, E. and I. Liddell (1975). "Timber Lattice Roof for the Mannheim Bundesgartenschau". In: *The Structural Engineer* 53.3.

Harding, J., W. Pearson, H. Lewis, and S. Melville (2015). "The Ongreening pavilion". In: *Advances in architectural geometry 2014*. Springer, pp. 295–308.

Harris, R., S. Haskins, and J. Roynon (2008). "The Savill Garden gridshell: design and construction". In: *The Structural Engineer* 86.17, pp. 27–34.

Harris, R., J. Romer, O. Kelly, and S. Johnson (2003). "Design and construction of the Downland Gridshell". In: *Building Research & Information* 31.6, pp. 427–454. ISSN: 0961-3218. DOI: 10.1080/0961321032000088007. URL: http://www.tandfonline.com/doi/abs/10.1080/0961321032000088007.

Haskell, C., N. Montagne, C. Douthe, O. Baverel, and C. Fivet (2021). "Generation of elastic geodesic gridshells with anisotropic cross sections". In: *International Journal of Space Structures* 36.4, pp. 294–306. DOI: 10.1177/09560599211064099. eprint: https://doi.org/10.1177/09560599211064099. URL: https://doi.org/10.1177/09560599211064099.

Hernández, E., O. Baverel, and C. Gengnagel (2013). "On the design and construction of elastic gridshells with irregular meshes". In: *International Journal of Space Structures* 28, pp. 161–174. URL: https://hal-enpc.archives-ouvertes.fr/hal-00946118.

Huang, W., L. Qin, and Q. Chen (2022). "Natural frequencies of pre-buckled rods and gridshells". In: *Applied Mathematical Modelling* 107, pp. 621–636. ISSN: 0307-904X. DOI: https://doi.org/10.1016/j.apm.2022.03.011. URL: https://www.sciencedirect.com/science/article/pii/S0307904X22001287.

Ion, A., M. Rabinovich, P. Herholz, and O. Sorkine-Hornung (2020). "Shape approximation by developable wrapping". In: *ACM Trans. Graph.* 39.6, pp. 1–12. ISSN: 0730-0301. DOI: 10.1145/3414685.3417835. URL: https://doi.org/10.1145/3414685.3417835%20https://dl.acm.org/doi/10.1145/3414685.3417835.

Isvoranu, F., J. Panetta, T. Chen, E. Bouleau, and M. Pauly (2019). "X-Shell Pavilion: A Deployable Elastic Rod Structure". In: *Proceedings of IASS Annual Symposia*. Vol. 2019. 5. International Association for Shell and Spatial Structures, pp. 1–8.

Jiang, C., K. Mundilova, F. Rist, J. Wallner, and H. Pottmann (2019). "Curve-Pleated Structures". In: *ACM Trans. Graph.* 38.6. ISSN: 0730-0301. DOI: 10.1145/3355089.3356540. URL: https://doi.org/10.1145/3355089.3356540.

Jiang, C., F. Rist, H. Pottmann, and J. Wallner (2020a). "Freeform Quad-Based Kirigami". In: *ACM Trans. Graph.* 39.6. ISSN: 0730-0301. DOI: 10.1145/3414685.3417844. URL: https://doi.org/10.1145/3414685.3417844.

Jiang, C., C. Wang, F. Rist, J. Wallner, and H. Pottmann (2020b). "Quad-Mesh Based Isometric Mappings and Developable Surfaces". In: *ACM Trans. Graph.* 39.4. ISSN: 0730-0301. DOI: 10.1145/3386569.3392430. URL: https://doi.org/10.1145/3386569.3392430.

Kilian, M., S. Flöry, Z. Chen, N. J. Mitra, A. Sheffer, and H. Pottmann (2008). "Curved folding". In: *ACM Trans. Graph.* 27.3, p. 1. ISSN: 0730-0301. DOI: 10.1145/1360612.1360674. URL: http://portal.acm.org/citation.cfm?doid=1399504.1360674%20http://portal.acm.org/citation.cfm?doid=1360612.1360674.

Kilian, M., A. Monszpart, and N. J. Mitra (2017a). "String Actuated Curved Folded Surfaces". In: *ACM Trans. Graph.* 36.3, pp. 1–13. ISSN: 0730-0301. DOI: 10.1145/3015460. URL: http://dl.acm.org/citation.cfm?doid=3087678.3015460.

Kilian, M., D. Pellis, J. Wallner, and H. Pottmann (2017b). "Material-minimizing forms and structures". In: *ACM Trans. Graph.* 36.6, pp. 1–12. ISSN: 0730-0301. DOI: 10.1145/3130800.3130827. URL: http://dl.acm.org/citation.cfm?doid=3130800.3130827.

Koenderink, J. and A. v. Doom (1998). "Shape from chebyshev nets". In: *European Conference on Computer Vision*. Springer, pp. 215–225.

Konaković, M., K. Crane, B. Deng, S. Bouaziz, D. Piker, and M. Pauly (2016). "Beyond developable". In: *ACM Trans. Graph.* 35.4, pp. 1–11. ISSN: 0730-0301. DOI: 10.1145/2897824.2925944. URL: https://dl.acm.org/citation.cfm?doid=2897824.2925944%20http://dl.acm.org/citation.cfm?doid=2897824.2925944.

Konaković-Luković, M., J. Panetta, K. Crane, and M. Pauly (2018). "Rapid deployment of curved surfaces via programmable auxetics". In: *ACM Trans. Graph.* 37.4, pp. 1–13. ISSN: 0730-0301. DOI: 10.1145/3197517.3201373. URL: http://dl.acm.org/citation.cfm?doid=3197517.3201373.

Laccone, F., L. Malomo, J. Pérez, N. Pietroni, F. Ponchio, B. Bickel, and P. Cignoni (2019). "FlexMaps Pavilion: a twisted arc made of mesostructured flat flexible panels". In: *Proceedings of IASS Annual Symposia*. Vol. 2019. 5. International Association for Shell and Spatial Structures (IASS), pp. 1–7.

Lagally, M. (1910). "Über die Verbiegung geodätischer Netze". In: vol. 1910,10. Sitzungsbericht der Bayerischen Akademie der Wissenschaften. München: Verl.d.K.B.Akad.d.Wiss. URL: http://publikationen.badw.de/de/003396114.

Lavine, M. S. (2015). "Popping materials and devices from 2D into 3D". In: *Science* 347.6218, pp. 141–143. ISSN: 0036-8075. DOI: 10.1126/science.347.6218.141-1. URL: https://science.sciencemag.org/content/347/6218/141.12%20https://science.sciencemag.org/content/347/6218/141.12.abstract.

Lefevre, B., C. Douthe, and O. Baverel (2015). "Buckling of elastic gridshells". In: *Journal of the International Association for shell and spatial structures* 56.3, pp. 153–171.

Lefevre, B., F. Tayeb, L. Du Peloux, and J.-F. Caron (2017). "A 4-degree-of-freedom Kirchhoff beam model for the modeling of bending–torsion couplings in active-bending structures". In: *International Journal of Space Structures* 32.2, pp. 69–83.

Lévy, B., S. Petitjean, N. Ray, and J. Maillot (2002). "Least Squares Conformal Maps for Automatic Texture Atlas Generation". In: *ACM Trans. Graph.* 21.3, pp. 362–371. ISSN: 0730-0301. DOI: 10.1145/566654.566590. URL: https://doi.org/10.1145/566654.566590.

Lienhard, J. (2014). "Bending-active Structures : Form-finding Strategies using Elastic Deformation in Static and Kinetic Systems and the Structural Potentials Therein". en. DOI: 10.18419/OPUS-107. URL: http://elib.uni-stuttgart.de/handle/11682/124.

Lienhard, J., H. Alpermann, C. Gengnagel, and J. Knippers (2013). "Active Bending, a Review on Structures where Bending is Used as a Self-Formation Process". In: *International Journal of Space Structures* 28.3-4, pp. 187–196. ISSN: 0266-3511. DOI: 10.1260/0266-3511.28.3-4.187. URL: http://journals.sagepub.com/doi/10.1260/0266-3511.28.3-4.187.

Lienhard, J. and C. Gengnagel (2018). "Recent developments in bending-active structures". In: *Creativity in Structural Design, annual Symposium of the IASS – International Association for Shell and Spatial Structures*. Boston.

Lira, W., C.-W. Fu, and H. Zhang (2018). "Fabricable Eulerian Wires for 3D Shape Abstraction". In: *ACM Trans. Graph.* 37.6. ISSN: 0730-0301. DOI: 10.1145/3272127.3275049. URL: https://doi.org/10.1145/3272127.3275049.

Liu, H.-Y., Z.-Y. Liu, Z.-Y. Zhao, L. Liu, and X.-M. Fu (2020). "Practical fabrication of discrete chebyshev nets". In: *Computer Graphics Forum*. Vol. 39. 7. Wiley Online Library, pp. 13–26.

Liu, M., L. Domino, and D. Vella (2020). "Tapered elasticæ as a route for axisymmetric morphing structures". In: *Soft Matter* 16.33, pp. 7739–7750. ISSN: 17446848. DOI: 10.1039/d0sm00714e. URL: https://pubs.rsc.org/en/content/articlehtml/2020/sm/d0sm00714e%20https://pubs.rsc.org/en/content/articlelanding/2020/sm/d0sm00714e.

Liu, Y., W. Xu, J. Wang, L. Zhu, B. Guo, F. Chen, and G. Wang (2011). "General Planar Quadrilateral Mesh Design Using Conjugate Direction Field". In: *ACM Trans. Graph.* 30.6, pp. 1–10. ISSN: 0730-0301. DOI: 10.1145/2070781.2024174. URL: https://doi.org/10.1145/2070781.2024174.

Liuti, A., A. Pugnale, and S. Colabella (2017). "The Airshell prototype: a timber gridshell erected through a pneumatic formwork". In: *Interfaces: Architecture, Engineering, Science, Annual Meeting of the International Association of Shell & Spatial Structures (IASS)*. Hamburg, p. 1. URL: https://structurae.net/en/literature/conference-paper/airshell-prototype-a-timber-gridshell-erected-through-a-pneumatic-formwork.

Malek, S., T. Wierzbicki, and J. Ochsendorf (2014). "Buckling of spherical cap gridshells: A numerical and analytical study revisiting the concept of the equivalent continuum". In: *Engineering Structures* 75, pp. 288–298. ISSN: 0141-0296. DOI: https://doi.org/10.1016/j.engstruct.2014.05.049. URL: https://www.sciencedirect.com/science/article/pii/S0141029614003472.

Malomo, L., J. Pérez, E. Iarussi, N. Pietroni, E. Miguel, P. Cignoni, and B. Bickel (2018). "FlexMaps". In: *ACM Trans. Graph.* 37.6, pp. 1–14. ISSN: 0730-0301. DOI: 10.1145/3272127.3275076. URL: http://dl.acm.org/citation.cfm?doid=3272127.3275076.

Massarwi, F., C. Gotsman, and G. Elber (2007). "Papercraft Models using Generalized Cylinders". In: *15th Pacific Conference on Computer Graphics and Applications (PG'07)*. IEEE, pp. 148–157. ISBN: 0-7695-3009-5. DOI: 10.1109/PG.2007.16. URL: http://ieeexplore.ieee.org/document/4392725/.

Miguel, E., M. Lepoutre, and B. Bickel (2016). "Computational design of stable planar-rod structures". In: *ACM Trans. Graph.* 35.4, pp. 1–11. ISSN: 0730-0301. DOI: 10.1145/2897824.2925978. URL: http://dl.acm.org/citation.cfm?doid=2897824.2925978.

Millar, C., T. Mitchell, A. Mazurek, A. Chhabra, A. Beghini, A. McRobie, and W. Baker (2021). "On funicular gridshells and Airy stress functions". In: *Proceedings of the IASS annual symposium*.

Mitani, J. and H. Suzuki (2004). "Making papercraft toys from meshes using strip-based approximate unfolding". In: *ACM SIGGRAPH 2004 Papers on - SIGGRAPH '04*. Vol. 23. 3. New York, New York, USA: ACM Press, p. 259. DOI: 10.1145/1186562.1015711. URL: http://portal.acm.org/citation.cfm?doid=1186562.1015711.

Mitchell, J. S., D. M. Mount, and C. H. Papadimitriou (1987). "The discrete geodesic problem". In: *SIAM Journal on Computing* 16.4, pp. 647–668.

Mitchell, T. (2014). "A limit of economy of material in shell structures". In: *Proceedings of IASS Annual Symposia*. Vol. 2014. 3. International Association for Shell and Spatial Structures (IASS), pp. 1–8.

Nicholas, P., E. L. Hernández, and C. Gengnagel (2013). "The Faraday Pavilion: activating bending in the design and analysis of an elastic gridshell". In: *Proceedings of the Symposium on Simulation for Architecture & Urban Design*, pp. 1–8.

Panagoulia, E. and S. Schleicher (2016). "Bending-active Structures: A Case study for an Office Chaise Lounge". In: *eCAADe – Computing for a better tomorrow*. Lodz: eCAADe (Education and Research in Computer Aided Architectural Design in Europe), pp. 621–630. URL: http://ecaade.org/downloads/eCAADe-2018-Volume1.pdf.

Panetta, J., F. Isvoranu, T. Chen, E. Siéfert, B. Roman, and M. Pauly (2021). "Computational Inverse Design of Surface-Based Inflatables". In: *ACM Trans. Graph.* 40.4. ISSN: 0730-0301. DOI: 10.1145/3450626.3459789. URL: https://doi.org/10.1145/3450626.3459789.

Panetta, J., M. Konaković-Luković, F. Isvoranu, E. Bouleau, and M. Pauly (2019). "X-Shells: a new class of deployable beam structures". In: *ACM Trans. Graph.* 38.4, pp. 1–15. ISSN: 0730-0301. DOI: 10.1145/3306346.3323040. URL: http://dl.acm.org/citation.cfm?doid=3306346.3323040%20https://dl.acm.org/doi/10.1145/3306346.3323040.

Panozzo, D., P. Block, and O. Sorkine-Hornung (2013). "Designing unreinforced masonry models". In: *ACM Trans. Graph.* 32.4, p. 1. ISSN: 0730-0301. DOI: 10.1145/2461912.2461958. URL: http://dl.acm.org/citation.cfm?doid=2461912.2461958.

Pellis, D., H. Wang, M. Kilian, F. Rist, H. Pottmann, and C. Müller (2020). "Principal Symmetric Meshes". In: *ACM Trans. Graph.* 39.4. ISSN: 0730-0301. DOI: 10.1145/3386569.3392446. URL: https://doi.org/10.1145/3386569.3392446.

Peloux, L. D. (2017). "Modeling of bending-torsion couplings in active-bending structures. Application to the design of elastic gridshells." Theses. Université Paris Est, École des Ponts Paris Tech, 6-8 avenue Blaise Pascal, 77455 Marne La Vallée. URL: https://tel.archives-ouvertes.fr/tel-01757782.

Pérez, J., M. A. Otaduy, and B. Thomaszewski (2017). "Computational design and automated fabrication of kirchhoff-plateau surfaces". In: *ACM Trans. Graph.* 36.4, pp. 1–12. ISSN: 0730-0301. DOI: 10.1145/3072959.3073695. URL: http://dl.acm.org/citation.cfm?doid=3072959.3073695.

Pérez, J., B. Thomaszewski, S. Coros, B. Bickel, J. A. Canabal, R. Sumner, and M. A. Otaduy (2015). "Design and fabrication of flexible rod meshes". In: *ACM Trans. Graph.* 34.4, 138:1–138:12. ISSN: 0730-0301. DOI: 10.1145/2766998. URL: http://dl.acm.org/citation.cfm?doid=2809654.2766998.

Perron, O. (1924). *Bestimmung aller geradlinigen rhombischen Netze*. Vol. 1924,16. Sitzungsbericht der Bayerischen Akademie der Wissenschaften. München: Verl. der Bayer. Akad. der Wiss. URL: http://publikationen.badw.de/de/003390833.

Pietroni, N., M. Tarini, A. Vaxman, D. Panozzo, and P. Cignoni (2017). "Position-based tensegrity design". In: *ACM Trans. Graph.* 36.6, pp. 1–14. ISSN: 0730-0301. DOI: 10.1145/3130800.3130809. URL: https://dl.acm.org/doi/10.1145/3130800.3130809.

Pillwein, S., J. Kübert, F. Rist, and P. Musialski (2020a). "Design and Fabrication of Elastic Geodesic Grid Structures". In: *Symposium on Computational Fabrication*. SCF '20. Virtual Event, USA: Association for Computing Machinery. ISBN: 9781450381703. DOI: 10.1145/3424630.3425412. URL: https://doi.org/10.1145/3424630.3425412.

— (2021a). "Design and fabrication of multi-patch elastic geodesic grid structures". In: *Computers & Graphics* 98, pp. 218–230. ISSN: 0097-8493. DOI: https://doi.org/10.1016/j.cag.2021.06.002. URL: https://www.sciencedirect.com/science/article/pii/S0097849321001163.

Pillwein, S., K. Leimer, M. Birsak, and P. Musialski (2020b). "On Elastic Geodesic Grids and Their Planar to Spatial Deployment". In: *ACM Transactions on Graphics* 39.4, 125:1–125:12. DOI: 10.1145/3386569.3392490.

Pillwein, S. and P. Musialski (2021b). "Generalized Deployable Elastic Geodesic Grids". In: *ACM Trans. Graph.* 40.6. ISSN: 0730-0301. DOI: 10.1145/3478513.3480516. URL: https://doi.org/10.1145/3478513.3480516.

Polthier, K. and M. Schmies (1998). "Straightest Geodesics on Polyhedral Surfaces". In: *Mathematical Visualization*. Berlin, Heidelberg: Springer Berlin Heidelberg, pp. 135–150. DOI: 10.1007/978-3-662-03567-2_11. URL: http://link.springer.com/10.1007/978-3-662-03567-2_11.

Pone, S., S. Colabella, B. Parenti, D. Lancia, A. Fiore, B. D'Amico, F. Portioli, R. Landolfo, M. D'Aniello, and C. Ceraldi (2013). "Construction and form-finding of a post-formed timber grid-shell". In: *Structures and architecture. Concepts, Applications and challenges*, pp. 245–252.

Pottmann, H., M. Eigensatz, A. Vaxman, and J. Wallner (2015). "Architectural geometry". In: *Computers & Graphics* 47, pp. 145–164. ISSN: 00978493. DOI: 10.1016/j.cag.2014.11.002. URL: https://linkinghub.elsevier.com/retrieve/pii/S009784931400140X.

Pottmann, H., Q. Huang, B. Deng, A. Schiftner, M. Kilian, L. Guibas, and J. Wallner (2010). "Geodesic patterns". In: *ACM Trans. Graph.* 29.4, pp. 1–10. ISSN: 0730-0301. DOI: 10.1145/1778765.1778780. URL: http://portal.acm.org/citation.cfm?doid=1778765.1778780%20https://dl.acm.org/doi/10.1145/1778765.1778780.

Qin, Y., X. Han, H. Yu, Y. Yu, and J. Zhang (2016). "Fast and Exact Discrete Geodesic Computation Based on Triangle-Oriented Wavefront Propagation". In: *ACM Trans. Graph.* 35.4, pp. 1–13. ISSN: 0730-0301. DOI: 10.1145/2897824.2925930. URL: https://doi.org/10.1145/2897824.2925930.

Quinn, G. and C. Gengnagel (2014). "A Review Of Elastic Grid Shells, Their Erection Methods And The Potential Use Of Pneumatic Formwork". In: *WIT Transactions on The Built Environment* 136. ISSN: 1746-4498. DOI: 10.2495/MARAS140111. URL: https://www.witpress.com/elibrary/wit-transactions-on-the-built-environment/136/26254.

Quinn, G. and C. Gengnagel (2018). "Full Scale Prototype for the Pneumatic Erection of Elastic Gridshells". In: *Proceedings of IASS Annual Symposia*. Vol. 2018. 15. International Association for Shell and Spatial Structures (IASS), pp. 1–8.

Rabinovich, M., T. Hoffmann, and O. Sorkine-Hornung (2018a). "Discrete Geodesic Nets for Modeling Developable Surfaces". In: *ACM Trans. Graph.* 37.2, pp. 1–17. ISSN: 0730-0301. DOI: 10.1145/3180494. URL: http://dl.acm.org/citation.cfm?doid=3191713.3180494.

— (2018b). "The Shape Space of Discrete Orthogonal Geodesic Nets". In: *ACM Trans. Graph.* 37.6. ISSN: 0730-0301. DOI: 10.1145/3272127.3275088. URL: https://doi.org/10.1145/3272127.3275088.

— (2019). "Modeling Curved Folding with Freeform Deformations". In: *ACM Trans. Graph.* 38.6. ISSN: 0730-0301. DOI: 10.1145/3355089.3356531. URL: https://doi.org/10.1145/3355089.3356531.

Ren, Y., J. Panetta, T. Chen, F. Isvoranu, S. Poincloux, C. Brandt, A. Martin, and M. Pauly (2021). "3D Weaving with Curved Ribbons". In: *ACM Trans. Graph.* 40.4. ISSN: 0730-0301. DOI: 10.1145/3450626.3459788. URL: https://doi.org/10.1145/3450626.3459788.

Sageman-Furnas, A. O., A. Chern, M. Ben-Chen, and A. Vaxman (2019). "Chebyshev Nets from Commuting PolyVector Fields". In: *ACM Trans. Graph.* 38.6. ISSN: 0730-0301. DOI: 10.1145/3355089.3356564. URL: https://doi.org/10.1145/3355089.3356564.

Sakai, Y., M. Ohsaki, and S. Adriaenssens (2020). "A 3-dimensional elastic beam model for form-finding of bending-active gridshells". In: *International Journal of Solids and Structures* 193, pp. 328–337.

Sanchez-Palencia, E., O. Millet, and F. Bechet (2010). *Singular problems in shell theory: computing and asymptotics*. Vol. 54. Springer Science & Business Media.

Schikore, J., A. M. Bauer, R. Barthel, and K.-U. Bletzinger (2019). "Large torsion on elastic lamella grid structures". In: *Proceedings of IASS Annual Symposia*. Vol. 2019. 18. International Association for Shell and Spatial Structures (IASS), pp. 1–8.

Schikore, J., E. Schling, T. Oberbichler, and A. M. Bauer (2021). "Kinetics and Design of Semi-Compliant Grid Mechanisms". In: *Advances in Architectural Geometry*, pp. 108–129.

Schling, E., M. Kilian, H. Wang, J. Schikore, and H. Pottmann (2018). "Design and construction of curved support structures with repetitive parameters". In: *Advances in Architectural Geometry (AAG) 2018*. ISBN: 978-3-903015-13-5.

Schling, E. and Z. Wan (2022). "A geometry-based design approach and structural behaviour for an asymptotic curtain wall system". In: *Journal of Building Engineering* 52, p. 104432. ISSN: 2352-7102. DOI: https://doi.org/10.1016/j.jobe.2022.104432. URL: https://www.sciencedirect.com/science/article/pii/S2352710222004454.

Schreck, C., D. Rohmer, S. Hahmann, M.-P. Cani, S. Jin, C. C. L. Wang, and J.-F. Bloch (2016). "Nonsmooth Developable Geometry for Interactively Animating Paper Crumpling". In: *ACM Trans. Graph.* 35.1. ISSN: 0730-0301. DOI: 10.1145/2829948. URL: https://doi.org/10.1145/2829948.

Sellán, S., N. Aigerman, and A. Jacobson (2020). "Developability of Heightfields via Rank Minimization". In: *ACM Trans. Graph.* 39.4. ISSN: 0730-0301. DOI: 10.1145/3386569.3392419. URL: https://doi.org/10.1145/3386569.3392419.

Sethian, J. A. (1999). "Fast Marching Methods". In: *SIAM Review* 41.2, pp. 199–235. DOI: 10.1137/S0036144598347059. eprint: https://doi.org/10.1137/S0036144598347059. URL: https://doi.org/10.1137/S0036144598347059.

Sharp, N. and K. Crane (2020). "You Can Find Geodesic Paths in Triangle Meshes by Just Flipping Edges". In: *ACM Trans. Graph.* 39.6. ISSN: 0730-0301. DOI: 10.1145/3414685.3417839. URL: https://doi.org/10.1145/3414685.3417839.

Shukhov, V. (1896). *Rotunda of the Panrussian Exposition (Nizhny Novgorod, 1896) | Structurae*. URL: https://structurae.net/en/structures/rotunda-of-the-panrussian-exposition (visited on 01/19/2020).

Soriano, E., R. Sastre, and D. Boixader (2019). "G-shells: Flat collapsible geodesic mechanisms for gridshells". In: *IASS Annual Symposium 2019 – Structural Membranes*. Barcelona.

Soriano, E. (2017). "Low-Tech Geodesic Gridshell: Almond Pavilion". In: *Archidoct* 4, p. 29. ISSN: 2309-0103.

Soriano, E., P. Tornabell, D. Naicu, and G. H. Filz (2015). "Topologically-based curvature in thin elastic shell networks". In: DOI: 10.13140/RG.2.1.3972.6965.

Stein, O., E. Grinspun, and K. Crane (2018). "Developability of triangle meshes". In: *ACM Trans. Graph.* 37.4, pp. 1–14. ISSN: 0730-0301. DOI: 10.1145/3197517.3201303. URL: https://dl.acm.org/doi/10.1145/3197517.3201303.

Surazhsky, V., T. Surazhsky, D. Kirsanov, S. J. Gortler, and H. Hoppe (2005). "Fast Exact and Approximate Geodesics on Meshes". In: *ACM Trans. Graph.* 24.3, pp. 553–560. ISSN: 0730-0301. DOI: 10.1145/1073204.1073228. URL: https://doi.org/10.1145/1073204.1073228.

Takezawa, M., T. Imai, K. Shida, and T. Maekawa (2016). "Fabrication of freeform objects by principal strips". In: *ACM Trans. Graph.* 35.6, pp. 1–12. ISSN: 0730-0301. DOI: 10.1145/2980179.2982406. URL: http://dl.acm.org/citation.cfm?doid=2980179.2982406.

Tang, C., P. Bo, J. Wallner, and H. Pottmann (2016). "Interactive Design of Developable Surfaces". In: *ACM Trans. Graph.* 35.2. ISSN: 0730-0301. DOI: 10.1145/2832906. URL: https://doi.org/10.1145/2832906.

Tang, C., X. Sun, A. Gomes, J. Wallner, and H. Pottmann (2014). "Form-finding with polyhedral meshes made simple". In: *ACM Trans. Graph.* 33.4, pp. 1–9. ISSN: 0730-0301. DOI: 10.1145/2601097.2601213. URL: http://dl.acm.org/citation.cfm?doid=2601097.2601213.

Tayeb, F., J. Caron, O. Baverel, and L. Du Peloux (2013). "Stability and robustness of a 300 m2 composite gridshell structure". In: *Construction and Building Materials* 49, pp. 926–938.

Terzopoulos, D., J. Platt, A. Barr, and K. Fleischer (1987). "Elastically deformable models". In: *ACM SIGGRAPH Computer Graphics* 21.4, pp. 205–214. ISSN: 00978930. DOI: 10.1145/37402.37427. URL: http://dl.acm.org/citation.cfm?id=37402.37427.

Tornabell, P., E. Soriano, and R. Sastre (2014). "Pliable structures with rigid couplings for parallel leaf-springs: a pliable timber torus pavilion". In: *Mobile and Rapidly Assembled Structures IV* 136.117, p. 485.

Tozoni, D. C., J. Dumas, Z. Jiang, J. Panetta, D. Panozzo, and D. Zorin (2020). "A Low-Parametric Rhombic Microstructure Family for Irregular Lattices". In: *ACM Trans. Graph.* 39.4. ISSN: 0730-0301. DOI: 10.1145/3386569.3392451. URL: https://doi.org/10.1145/3386569.3392451.

Trettner, P., D. Bommes, and L. Kobbelt (2021). "Geodesic Distance Computation via Virtual Source Propagation". In: *Computer graphics forum*. Vol. 40. 5. Wiley Online Library, pp. 247–260.

Vekhter, J., J. Zhuo, L. F. G. Fandino, Q. Huang, and E. Vouga (2019). "Weaving geodesic foliations". In: *ACM Trans. Graph.* 38.4, pp. 1–22. ISSN: 0730-0301. DOI: 10.1145/3306346.3323043. URL: http://dl.acm.org/citation.cfm?doid=3306346.3323043.

Verhoeven, F., A. Vaxman, T. Hoffmann, and O. Sorkine-Hornung (2022). "Dev2PQ: Planar Quadrilateral Strip Remeshing of Developable Surfaces". In: *ACM Trans. Graph.* 41.3. ISSN: 0730-0301. DOI: 10.1145/3510002. URL: https://doi.org/10.1145/3510002.

Voss, A. (1907). "Über diejenigen Flächen, welche durch zwei Scharen von Kurven konstanter geodätischer Krümmung in infinitesimale Rhomben zerlegt werden". In: vol. 36,7. Sitzungsbericht der Bayerischen Akademie der Wissenschaften. München: Verl.d.K.B.Akad.d.Wiss. URL: http://publikationen.badw.de/de/003388868.

Vouga, E., M. Höbinger, J. Wallner, and H. Pottmann (2012). "Design of self-supporting surfaces". In: *ACM Trans. Graph.* 31.4, pp. 1–11. ISSN: 0730-0301. DOI: 10.1145/2185520.2185583. URL: http://dl.acm.org/citation.cfm?doid=2185520.2185583.

Wallner, J., A. Schiftner, M. Kilian, S. Flöry, M. Höbinger, B. Deng, Q. Huang, and H. Pottmann (2010). "Tiling Freeform Shapes With Straight Panels: Algorithmic Methods." In: *Advances in Architectural Geometry 2010*. Vienna: Springer Vienna, pp. 73–86. DOI: 10.1007/978-3-7091-0309-8_5. URL: http://link.springer.com/10.1007/978-3-7091-0309-8_5.

Wang, H., D. Pellis, F. Rist, H. Pottmann, and C. Müller (2019). "Discrete geodesic parallel coordinates". In: *ACM Trans. Graph.* 38.6, pp. 1–13. DOI: 10.1145/3355089.3356541. URL: https://dl.acm.org/doi/10.1145/3355089.3356541.

Wang, X., Z. Fang, J. Wu, S.-Q. Xin, and Y. He (2017). "Discrete geodesic graph (DGG) for computing geodesic distances on polyhedral surfaces". In: *Computer Aided Geometric Design* 52, pp. 262–284.

Welch, W. and A. Witkin (1992). "Variational surface modeling". In: *ACM SIGGRAPH Computer Graphics* 26.2, pp. 157–166. ISSN: 00978930. DOI: 10.1145/142920.134033. URL: http://dl.acm.org/citation.cfm?id=142920.134033.

Woodbury, R., S. Williamson, and P. Beesley (2006). "Parametric Modelling as a Design Representation in Architecture: A Process Account". In: *Proceedings of the Canadian Engineering Education Association (CEEA)*.

Xin, S.-Q. and G.-J. Wang (2007). "Efficiently determining a locally exact shortest path on polyhedral surfaces". In: *Computer-Aided Design* 39.12, pp. 1081–1090. ISSN: 0010-4485. DOI: https://doi.org/10.1016/j.cad.2007.08.001. URL: https://www.sciencedirect.com/science/article/pii/S0010448507001959.

— (2009). "Improving Chen and Han's Algorithm on the Discrete Geodesic Problem". In: *ACM Trans. Graph.* 28.4. ISSN: 0730-0301. DOI: 10.1145/1559755.1559761. URL: https://doi.org/10.1145/1559755.1559761.

Xu, H., E. Knoop, S. Coros, and M. Bächer (2018). "Bend-It: Design and Fabrication of Kinetic Wire Characters". In: *ACM Trans. Graph.* 37.6. ISSN: 0730-0301. DOI: 10.1145/3272127.3275089. URL: https://doi.org/10.1145/3272127.3275089.

Yang, Z., P. Xu, H. Fu, and H. Huang (2021). "WireRoom: Model-Guided Explorative Design of Abstract Wire Art". In: *ACM Trans. Graph.* 40.4. ISSN: 0730-0301. DOI: 10.1145/3450626.3459796. URL: https://doi.org/10.1145/3450626.3459796.

Ying, X., C. Huang, X. Fu, Y. He, R. Yu, J. Wang, and M. Yu (2019). "Parallelizing discrete geodesic algorithms with perfect efficiency". In: *Computer-Aided Design* 115, pp. 161–171. ISSN: 0010-4485. DOI: https://doi.org/10.1016/j.cad.2019.05.023. URL: https://www.sciencedirect.com/science/article/pii/S0010448519301988.

Ying, X., X. Wang, and Y. He (2013). "Saddle Vertex Graph (SVG): A Novel Solution to the Discrete Geodesic Problem". In: *ACM Trans. Graph.* 32.6. ISSN: 0730-0301. DOI: 10.1145/2508363.2508379. URL: https://doi.org/10.1145/2508363.2508379.

Ying, X., S.-Q. Xin, and Y. He (2014). "Parallel Chen-Han (PCH) Algorithm for Discrete Geodesics". In: *ACM Trans. Graph.* 33.1. ISSN: 0730-0301. DOI: 10.1145/2534161. URL: https://doi.org/10.1145/2534161.